Wave propagation and tidal dissipation in giant planets containing regions of stable stratification

Christina Mary Pontin

Submitted in accordance with the requirements for the degree of
Doctor of Philosophy

The University of Leeds
Department of Applied Mathematics

May 2022

The candidate confirms that the work submitted is their own, except where work which has formed part of jointly authored publications has been included. The contribution of the candidate and the other authors to this work has been explicitly indicated below. The candidate confirms that appropriate credit has been given within the thesis where reference has been made to the work of others.

Chapters 2 and 3 contain material from the jointly authored publication,

- **Pontin C. M., Barker A. J., Hollerbach R., André Q., Mathis S. (2020)**
  Wave propagation in semiconvective regions of giant planets,
  Monthly Notices of the Royal Astronomical Society, Volume 493, Issue 4, April 2020, Pages 5788–5806

C.M. Pontin carried out the majority of the calculations and writing for the paper, producing all figures. A. J. Barker and R. Hollerbach provided advice, verified some calculations and edited the paper draft. Q. André, S. Mathis were involved in some discussions and provided editorial comments on the paper.

For

Sheila Marshall

Acknowledgements

First and foremost, I would like to thank my supervisors Adrian Barker and Rainer Hollerbach for your support and guidance throughout my PhD. Your continued assistance and extensive knowledge has in no doubt enhanced the content of this thesis. I would like to thank my examiners Chris Jones and Gordon Ogilvie for examining my thesis and the useful comments that came from my viva.

I would like to thank my tutor Chris, for the additional support and guidance you have given me when faced with some of the hardest tasks required in putting together this thesis. Thank you for never letting me think any task was beyond my ability.

It has been wonderful to be part of such an active research community both in Leeds and further afield. I would like to thank all who have contributed to this community, for all the interesting conversations and all I have learnt from you over the course of my PhD. In particular I thank my co-authors for the joint papers. I am fortunate to have taken part in the Kavli Summer Programme in Astrophysics and would like to acknowledge The Kavli Foundation for funding, as well as my supervisor Nic Brummell, and Bhishek Manek working with me throughout the programme.

I am also grateful for the funding received from the STFC to complete this research.

And finally for the more personal acknowledgements. I thank my parents and grandparents for the emotional, academic, and financial support that you have given me over the last 28 years, without which I would not be where I am today. Also, my partner, brothers, extended family, and friends (near and far) who have supported in so many different ways. Whether it be coffee breaks, badminton, boardgames, pub trips (when the government guidance allowed them) or the numerous video calls that got us through the multiple lockdowns. Your support is truly appreciated.

Abstract

Tidal interactions impact the long-term evolution of orbits and spins of planet-satellite systems. Observations of these orbits and spins for giant planets in our solar system suggest efficient tidal dissipation. We also know that tidal dissipation is strongly influenced by the internal structure of a planet. This, coupled with evidence for stable stratification or semi-convective layers within giant planets, motivates considering the effect of stratification on tidal interactions.

In this thesis we analyse how stable stratification within giant planets can alter tidal dissipation rates through excitation and subsequent dissipation of internal and inertial waves. We combine a mixture of analytical calculations with numerical results in a global spherical Boussinesq model, both with and without rotation. We analyse the free modes and transmission of waves through layered staircase structures, as well as studying the dissipation rates of tidally forced systems where stably stratified layers form.

We find that a staircase density structure can alter the free modes and the transmission of waves through such a medium. We find our results tend towards the behaviour of a continuously stratified medium as the number of steps in the staircase increases, and that the transmission of short wavelength waves through a staircase is only efficient when they are resonant with the free modes.

Enhanced tidal dissipation arises when the tidal forcing frequency is close to a resonance of the system. By varying parameters, we find overarching trends in dissipation rates. In particular, that an extended core can enhance the inertial wave response, but such a response is not strongly altered by the properties of the core itself. Therefore, we find that as well as introducing additional internal gravity and gravito-inertial wave resonances into the system, stable stratification can enhance the inertial wave response, all of which can contribute to the resultant tidal dissipation.

Contents

List of figures

List of tables

Chapter 1

Introduction

1.1 Planetary Context

The study of planetary interiors is a large and active subject of research. Although far too large a field to fully summarise here, we begin by outlining some of the current understanding of giant planet interiors and highlight some of the uncertainties in these models. It is these uncertainties that underline and motivate the research carried out in this thesis.

1.1.1 The standard "3-layer" model

Scientists have been studying the formation and interiors of giant planets for many years, since at least the 1950's (Hubbard & Smoluchowski, 1973). The various compositions and structures possible for the interiors of giant planets have been continuously evolving since. Both historically, and currently when it is convenient to simplify analysis, the structures of our Solar System's giant planets are often described by the "3-layer model". This structure is sketched in Figure 1.1, and as the name suggests, consists of three distinct layers (e.g Stevenson, 1982; Guillot, 2005; Helled et al., 2014):

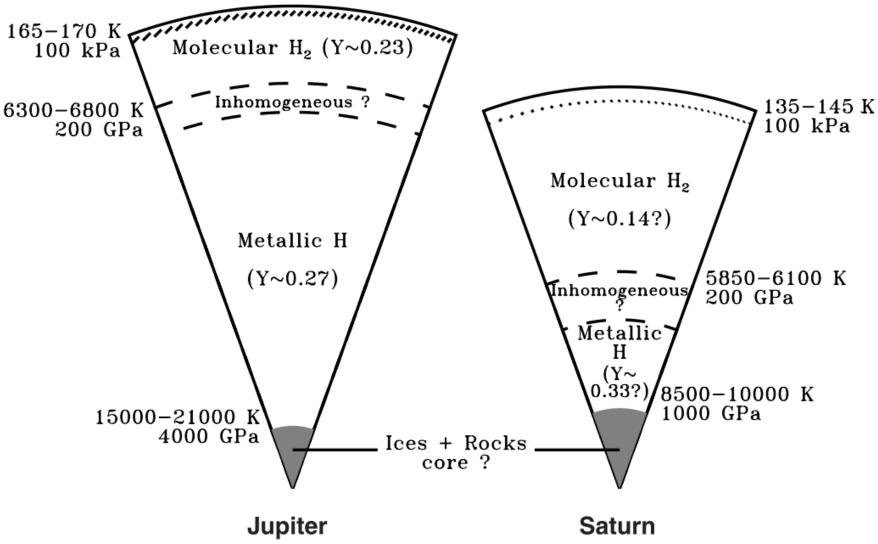

Figure 1.1: Diagrams of Jupiter's and Saturn's interior profile, from Guillot (1999).

1. The first is a dense, typically solid, inner core. This is thought to consist predominantly of heavy elements. This is sometimes also referred to as a rocky or icy core.

2. Above the inner core sits a convective layer which is composed mostly of Hydrogen and Helium. The temperature and pressure in this region is sufficiently high that Hydrogen exists in its metallic form. It is in this region where magnetic fields are thought to be produced by the motion of electrically conducting fluid.

3. The final layer is an outer envelope, again consisting of Hydrogen and Helium but in molecular form. This layer is normally expected to have a lower Helium content than the metallic region.

In the 3-layer model, each layer is usually assumed to be chemically homogeneous, and convection to be sufficiently efficient that the entropy profile is considered to be adiabatic (i.e. neutrally stable to convection). This standard model can do very well at explaining many of the observations of giant planets. Therefore, it is a useful baseline for further work, however the exact nature and location of the transition regions between layers are hard to constrain and cannot

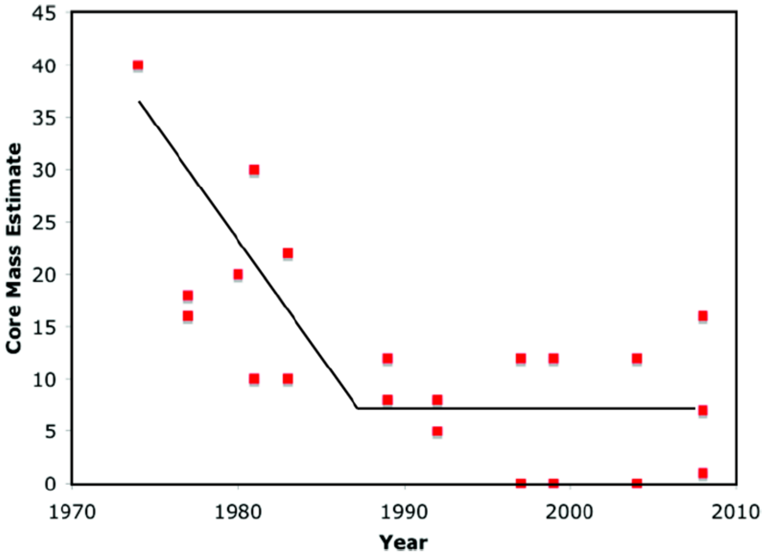

Figure 1.2: Historical estimates from different sources for the core mass of Jupiter in Earth masses. Figure taken from Fortney & Nettelmann (2010).

always explain observational results. Additionally, the predictions for our planets vary significantly, suggesting the range of possible core structures for giant planets elsewhere is large. This motivates continued interest in researching this field.

1.1.2 Departure from the “3-layer model” and recent advancements

Our understanding of the giant planets in our solar system is constantly developing. For instance Figure 1.2, taken from Fortney & Nettelmann (2010), shows estimates of the core masses of Jupiter from various studies from 1970 to 2010, and demonstrates how significantly our predictions have varied with time and between studies. Note in particular that this figure pre-dates results of the Juno mission which has considerably changed current estimated bounds on Jupiter’s core mass.

There is significant motivation for the presence of a solid core. Firstly, this dense centre fits with most planetary formation models. Although there are multiple formation mechanisms and only some rely on a solid core, those that do not initially can later evolve to form a dense core. The mechanism of core accretion relies on the formation of a solid core which is followed by the rapid accretion of nebular gas; the required core sizes vary significantly in models ($\sim 2M_\oplus$ to $\sim 10M_\oplus$) however they would be expected to remain (Pollack et al., 1996; Wahl et al., 2017). Alternatively, considering a formation mechanism such as the collapse of a portion of a disk due to a gravitational instability does not rule out a core forming later in the evolution (Helled & Schubert, 2009; Wahl et al., 2017).

It is possible that this dense core is not necessarily solid but partially fluid, which could lead to additional physics beyond the scope of this thesis. However, this does not mean it cannot have a significantly higher density from its surroundings (Goodman & Lackner, 2009).

Measurement of the gravity fields of the giant planets can be used to establish their masses and how this mass is distributed. Recent advancements, in particular with data from the Juno mission, are driving planetary models away from three distinct layers and instead towards models including more inhomogeneous distributions of heavy elements, including the transition regions between the previously-adopted layers. In particular, these gravity field measurements indicate that instead of a small dense core, the heavy-elements of Jupiter are probably distributed throughout the inner regions of the planet (Wahl et al., 2017; Helled & Stevenson, 2017; Bolton et al., 2017; Debras & Chabrier, 2019).

Kronoseismology measurements of Saturn give further information on its interior. By detecting and measuring the frequency of waves in Saturn's rings this gives some information on their potential coupling with the possible interior modes. These modes are expected to be excited by tidal interactions. Recent observations suggest that frequencies in Saturn's rings are consistent with frequencies excited by gravitational forcing due to global oscillation modes (g-modes) inside Saturn, therefore requiring some form of stratification (Marley & Porco, 1993; Hedman & Nicholson, 2013; Hedman et al., 2018). In fact some studies suggest that the frequencies reached could only exist if there are large regions of strong stable stratification within the planet; these internal modes (g-modes) mix with

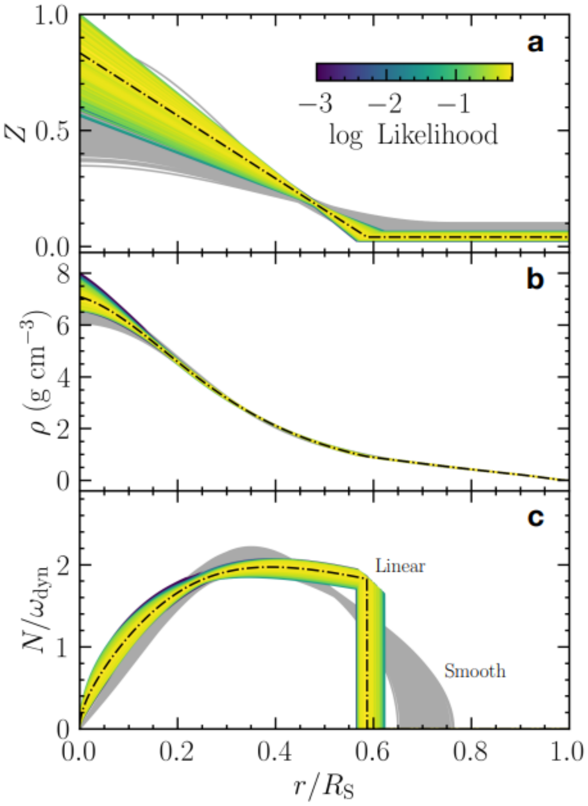

Figure 1.3: Possible interior profiles of Saturn from Kronoseismology and gravity field measurements. Figure taken from Mankovich & Fuller (2021), shows, (a) heavy element mass fraction, (b) density and (c) Brunt-Väisälä frequency for a series of model runs.

the surface gravity (f-modes) creating the mixed modes observed (Fuller, 2014). Kronoseismology data combined with gravity field measurements can be used to constrain the internal stratification (Mankovich & Fuller, 2021; Dewberry et al., 2021). Figure 1.3, taken from Mankovich & Fuller (2021), shows the density and buoyancy frequency profiles found using this data, where a dilute core of heavy elements extends into the convective region.

As a result of these findings, there has been much ongoing research in recent years to explore planetary models incorporating compositional gradients or non-adiabatic structures (e.g. Leconte & Chabrier, 2012; Vazan et al., 2016; Berardo & Cumming, 2017; Lozovsky et al., 2017; Vazan et al., 2018; Debras & Chabrier, 2019). If a stably stratified region exists within the planet, it could inhibit convection, which in turn could reduce the transport of energy to the surface (Chabrier & Baraffe, 2007). A consequence of this reduced energy transport is a decrease in the luminosity observed at the surface, which could be responsible for Saturn's observed luminosity (Leconte & Chabrier, 2013). Secondly, some hot Jupiters are thought to have an inflated radius, which formation models suggest again could be a result of reduced energy transport (e.g Chabrier & Baraffe, 2007).

1.2 Double diffusive convection

Adapting planetary models to include a layer of stable stratification can result in additional interesting physics. One such consequence is double diffusive convection, a mechanism caused by a linear instability, that can lead to interesting non-linear physics. Here, we will outline the main consequences but for a thorough review see Garaud (2018).

In previous models, by considering well-mixed convective regions, the planetary layers consist of unstable entropy gradients. Now that we are additionally considering that there is a stable composition gradient, there are two competing components contributing to the local density gradient. There are two possible regimes for this instability to occur, depending on the rate of the stable component compared with that of the unstable component as well as the relative gradients of the quantities concerned. There are three key parameters which dictate which regime is expected to develop; Prandtl number $Pr = \frac{\nu}{\kappa}$, ratio of diffusivities $\tau = \frac{\kappa_c}{\kappa}$, and the density ratio $R_0 = \frac{\alpha\left|\frac{\mathrm{d}T_0}{\mathrm{d}z} - \frac{\mathrm{d}T_{ad}}{\mathrm{d}z}\right|}{\beta\left|\frac{\mathrm{d}C_0}{\mathrm{d}z}\right|}$ which is a measure of stratification (see Garaud (2018)), where ν is the kinematic viscosity, κ is the thermal diffusivity, and κ_c is the compositional diffusivity. In giant planets (and most other astrophysically relevant scenarios), it is expected that temperature diffuses much more rapidly than momentum and composition and therefore $Pr \ll 1$ and $\tau \ll 1$. This means that a layer that might be considered stable to standard convection, can in fact become unstable to the double-diffusive instability.

For the case where the rapidly diffusive component is unstable (in our case entropy/temperature), and the slowly diffusing component is stable (composition), this gives rise to oscillatory double diffusive convection (ODDC). Alternatively, however, we could consider a regime in which the rapidly diffusing component is stabilising, and the slowly diffusing component is destabilising, which gives rise to fingering convection. This is not discussed here as it is not the focus of this study, but see the review of Garaud (2018) for more detail. Note that it does not matter which component diffuses faster, composition or entropy, or even that they are entropy and composition, just that they are competing gradients with different rates. Double diffusive convection can also occur when there are two distinct chemical concentrations, however the regimes that the instability develops into can depend on the nature of the stability gradients (Garaud, 2018).

1.2.1 Initial linear instability

We first consider the behaviour of the initial linear instability that forms because of these competing gradients.

If we take a system with a stable composition gradient and constant entropy,

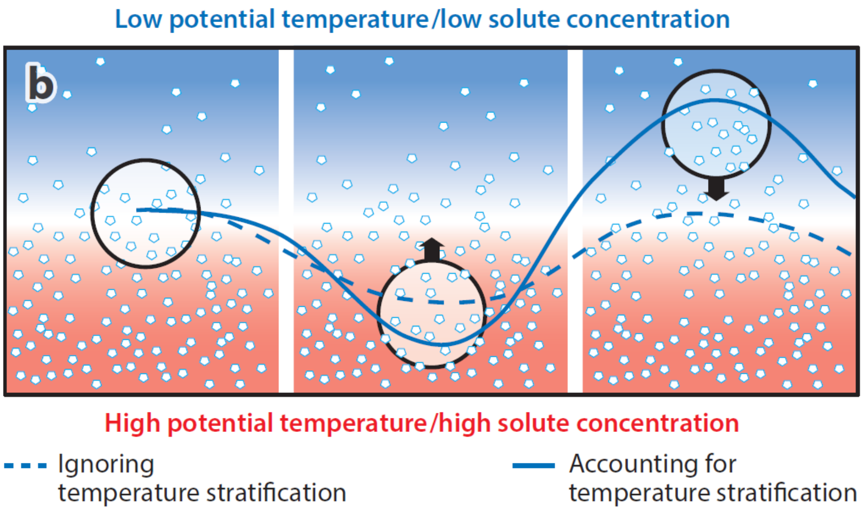

Figure 1.4: Diagram of the Oscillatory Double Diffusive convection instability, showing enhanced gravity wave oscillations, from Garaud (2018).

when a perturbed fluid parcel is displaced upwards it is denser than the surrounding fluid and will therefore sink before adjusting to the surroundings (or vice-versa for a fluid parcel displaced downwards). This forms a traditional internal gravity wave as will be discussed in Section 1.5. However, if we now consider that there is also a more rapidly diffusing, destabilising entropy gradient, when the fluid parcel is displaced, again considering upwards, the fast diffusion of heat occurs, which cools down the fluid parcel more rapidly than any diffusion of composition. Therefore, when the fluid sinks it is now cooler than the surrounding fluid. This enhances the amplitude of the oscillations as shown in Figure 1.4; this is often referred to as an oscillatory instability or overstability.

The size of the structures that develop in this linear regime can be shown to be of the order (Walin, 1964; Kato, 1966; Baines & Gill, 1969),

$$d = \left(\frac{\kappa\nu}{N^2}\right)^{\frac{1}{4}}, \tag{1.1}$$

where N^2 is the Brunt-Väisälä frequency defined in Section 1.4. Although we expect this value to be small in giant planets, we note that in the subsequent non-linear interactions they can evolve into much larger structures.

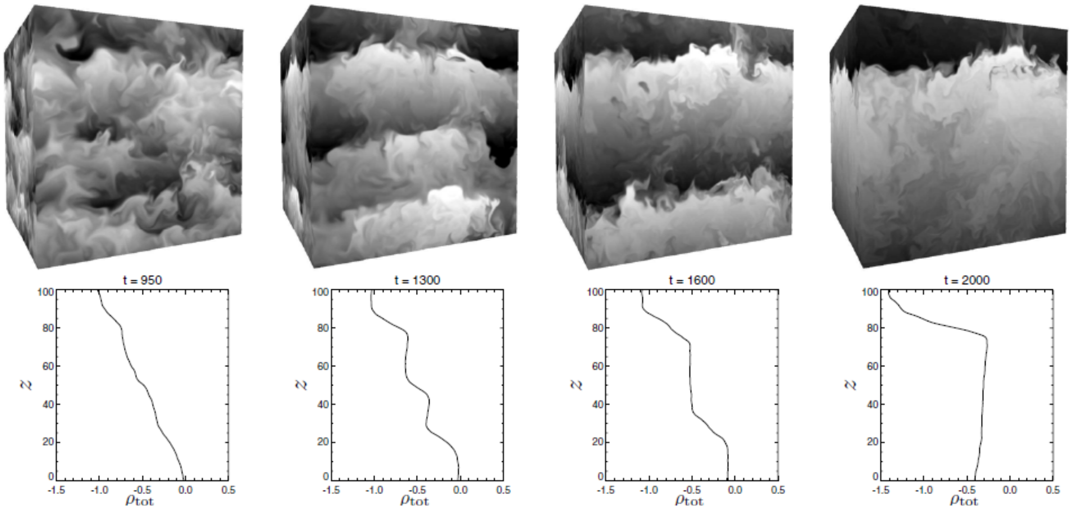

Figure 1.5: 3-D simulation showing the formation and consequential merger of semi-convective layers by double diffusive convection, figure taken from Wood et al. (2013).

Linear stability analysis shows that a system can be unstable to the oscillatory double diffusive convection when in the following regime (Baines & Gill, 1969),

$$1 < R_0^{-1} < \frac{Pr + 1}{Pr + \tau}, \tag{1.2}$$

where R_0 and τ are the density ratio and ratio of diffusivities as defined previously. From this we can see that when considering the low Prandtl number regime, where typically $Pr \sim \tau \ll 1$, the upper limit is much larger than one and there can be a large parameter space in which an instability can occur. Additionally, there have been observations of such an instability occurring outside the regime defined in equation 1.2. This suggests that there is still much more to understand about this problem, and the instabilities that can cause it (Garaud (2018) and therein).

1.2.2 Non-linear saturation

The behaviour of the system changes as it develops into a non-linear instability, and this has been an active area of research where analysis has been carried out by 3-D numerical simulations. It is after this point that non-linear interactions occur and the dynamics change significantly from that observed in the linear instability (Mirouh et al., 2012).

Upon saturation there are again two regimes observed; in cases where the system is more stably stratified homogeneous turbulence forms. In the case of weakly stably stratified systems spontaneous layering can form. It is this layering that is of particular interest in this case. The system evolves into layers that can be seen to form and then merge over time. Figure 1.5, from Wood et al. (2013), shows a simulation of these layers forming and then merging. Referred to as semi-convective layers, they consist of homogeneous well-mixed convective layers that are separated by narrow diffusive interfaces, and it is the consequence of these interfaces that is one aspect we wish to investigate further.

It is possible that these layers form in the deep interiors of giant planets; however the fact that the simulations find these layers to eventually merge over time makes it difficult to predict the number and size of these layers that could potentially form in a realistic system (Wood et al., 2013).

1.2.3 Planetary consequences of double diffusive convection

As discussed in Section 1.1.2, it is possible that giant planets contain stabilising composition gradients near the transition regions in the 3 layer model. Therefore, the conditions could be consistent with the parameters required to exhibit double diffusive convection and ultimately evolve to form semi-convective layers.

Just outside the core, where a stabilising composition gradient is consistent with the gravity field observations from Juno, a compositional gradient could be produced by the erosion or dissolution of the solid inner core. The temperature and pressure near the core boundary in a giant planet could be sufficient that heavy elements from the core can dissolve into the metallic Hydrogen/Helium region. This would then cause this extended core structure to generate a stable composition gradient (Guillot et al., 2004; Wilson & Militzer, 2012; Wahl et al., 2017; Moll et al., 2017). Alternatively, some studies suggest that a direct impact during the early formation of Jupiter could lead to an extended dilute core, (Liu et al., 2019; Guillot, 2019).

In the second transition region, further out between the metallic and molecular layers, it is thought that the temperature and pressure conditions are such that Helium molecules can form what is referred to as Helium rain, which sinks Helium further into the deep interior (Nettelmann et al., 2015; Stevenson & Salpeter, 1977).

1.2.4 Other applications of double diffusive convection

It is not just in the deep interiors of giant planets that these instabilities are thought to occur. Other astrophysical applications include stellar interiors. It is thought that density gradients may also be present outside the cores of massive stars, where heavy elements generated through nuclear reactions can diffuse into the neighbouring convective region (Maeder, 2009; Kippenhahn et al., 2012).

Although current technology means that observations of stars and giant planets are not sufficient to directly detect these density staircases, they can be observed elsewhere. Competing gradients occur in the deep oceans on Earth, where a stabilising salinity gradient competes against the destabilising temperature gradient. Direct observations of these layers have been observed in the Arctic oceans on Earth, where there is a stabilising salinity gradient and a destabilising thermal gradient (e.g. Ghaemsaidi et al., 2016; Shibley et al., 2017; Shibley & Timmermans, 2019).

1.3 Tides

Any two real bodies orbiting one another exert a tidal force, the consequences of which can vary depending on the parameters of the bodies and orbit, but they can be significant for the ultimate evolution of the system. This tidal force and the consequences of tidal dissipation (particularly for giant planets) is the focus of this study. We consider the implications of various density structures containing stably stratified layers for tidal behaviour in giant planets. Therefore, here we introduce some background in tidal theory.

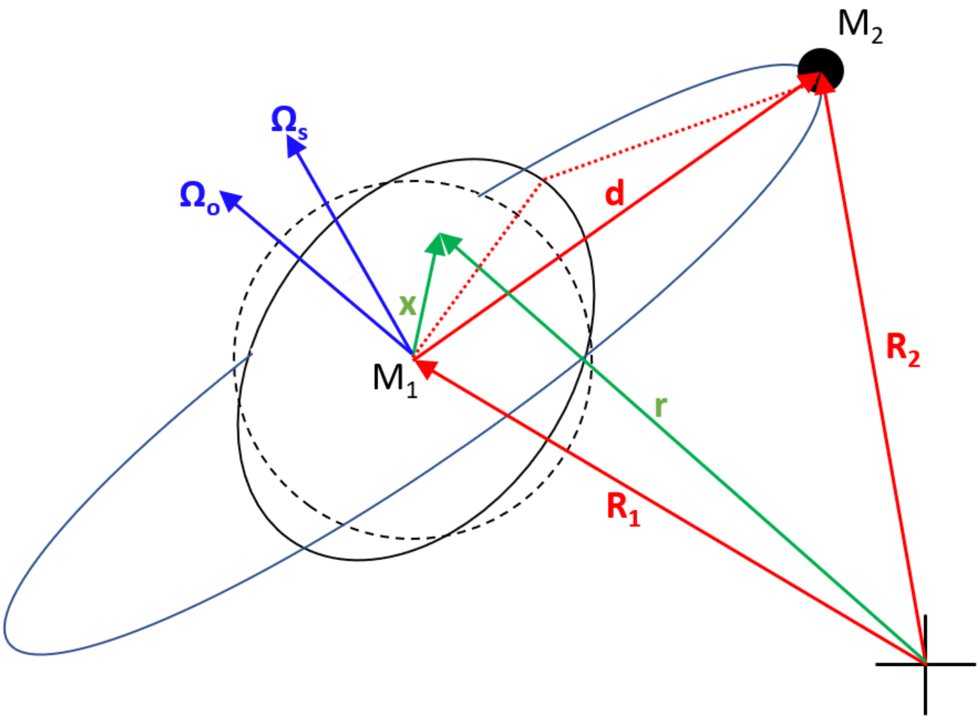

Figure 1.6: Schematic of 2-body tidal interaction adapted from Ogilvie (2014). It shows a planet-moon system, where Body 1 (mass M_1, position R_1 and spin $\boldsymbol{\Omega_s}$), is tidally deformed by the orbiting Body 2 (mass M_2, position R_2 and orbit $\boldsymbol{\Omega_o}$).

1.3.1 Tidal forcing

While tidal theory applies for any orbiting bodies, we will consider here a system consisting of a planet and a satellite. Figure 1.6 illustrates the two-body system we are considering. It consists of an isolated system where a point mass satellite, hereafter "Body 2", is orbiting an extended planet, "Body 1". This follows other standard derivations of tidal dynamics such as Murray & Dermott (2000) and Ogilvie (2014).

Starting by considering classical Newtonian physics, we know that there is a gravitational force that one body applies to other bodies. In this case we know that the potential caused by Body 2 at a point $\boldsymbol{r}$ in Body 1 is,

$$\Phi = -\frac{G\,M_2}{|\boldsymbol{r} - \boldsymbol{R}_2|}, \tag{1.3}$$

where the force exerted on a component of mass m' is $\boldsymbol{F} = -m'\boldsymbol{\nabla}\Phi$. By taking a Taylor series about the point $\boldsymbol{r} = \boldsymbol{R_1}$ it can be shown that,

$$\Phi \approx -\frac{G\,M_2}{|\boldsymbol{d}|}\left[1 + \frac{\boldsymbol{d}\cdot\boldsymbol{x}}{|\boldsymbol{d}|^2} + \frac{3(\boldsymbol{d}\cdot\boldsymbol{x})^2 - |\boldsymbol{d}|^2|\boldsymbol{x}|^2}{2|\boldsymbol{d}|^4} + \cdots\right], \tag{1.4}$$

where $\boldsymbol{d} = \boldsymbol{R_2} - \boldsymbol{R_1}$ and $\boldsymbol{x} = \boldsymbol{r} - \boldsymbol{R_1}$. This can be expressed in exact form using Legendre polynomials as

$$\Phi = -\frac{G\,M_2}{|\boldsymbol{d}|}\sum_{l=0}^{\infty}\frac{|\boldsymbol{x}|^l}{|\boldsymbol{d}|^l}P_l\left(\frac{\boldsymbol{d}\cdot\boldsymbol{x}}{|\boldsymbol{d}||\boldsymbol{x}|}\right), \tag{1.5}$$

where P_l is the normalised Legendre polynomial of degree l.

We note that if we assume that $|\boldsymbol{x}| \ll |\boldsymbol{d}|$, as is true in a planet-moon system, that terms in this series are of the order $\mathcal{O}(|\boldsymbol{x}/\boldsymbol{d}|^l)$. Therefore, higher order terms can be neglected when taking an appropriate approximation. Considering the terms in equation 1.5 and remembering that the resultant force applied is proportional to $\nabla\Phi$, we find that,

1. The 1st term ($l = 0$) is a constant and thus does not contribute to the overall force.
2. The 2nd term ($l = 1$) causes Body 1 to undergo orbital motion about the centre of mass of the system.
3. The remaining higher order terms, ($l \geq 2$) are then considered to be the tidal potential Ψ.

We therefore define the tidal potential to be,

$$\Psi = -\frac{G\,M_2}{|\boldsymbol{d}|}\sum_{l=2}^{\infty}\frac{|\boldsymbol{x}|^l}{|\boldsymbol{d}|^l}P_l\left(\frac{\boldsymbol{d}\cdot\boldsymbol{x}}{|\boldsymbol{d}||\boldsymbol{x}|}\right) \approx -\frac{G\,M_2}{|\boldsymbol{d}|}\left[\frac{3(\boldsymbol{d}\cdot\boldsymbol{x})^2 - |\boldsymbol{d}|^2|\boldsymbol{x}|^2}{2|\boldsymbol{d}|^4} + \cdots\right]. \tag{1.6}$$

By setting the co-ordinate system to align with the centre of Body 1, such that

$\boldsymbol{R_1} = 0$, $\boldsymbol{d} = \boldsymbol{R_2}$ and $\boldsymbol{x} = \boldsymbol{r}$, the tidal potential can be further simplified to,

$$\Psi = -\frac{G\,M_2}{|\boldsymbol{d}|}\sum_{l=2}^{\infty}\frac{|\boldsymbol{r}|^l}{|\boldsymbol{d}|^l}P_l\left(\frac{\boldsymbol{d}\cdot\boldsymbol{r}}{|\boldsymbol{d}||\boldsymbol{r}|}\right) = -\frac{G\,M_2}{|\boldsymbol{d}|}\sum_{l=2}^{\infty}\frac{r^l}{|\boldsymbol{d}|^l}P_l\big(\cos\theta\big). \tag{1.7}$$

Currently this formulation allows for a general vector $\boldsymbol{d}$, but as we consider the bodies to be undergoing Keplerian motion we know that it must describe the orbit of Body 2. Therefore, it can be defined as that of an orbit with eccentricity e, inclination i and semi major axis a (Kaula, 1961; Polfliet & Smeyers, 1990; Ogilvie, 2014). Finally, the Legendre polynomials can be written in terms of normalised spherical harmonics, where l and m are the spherical harmonic degree and order, i.e.,

$$\Psi = \mathrm{Re}\sum_{l=2}^{\infty}\sum_{m=0}^{l}\sum_{n=-\infty}^{\infty}\frac{G\,M_2}{a}A_{l,m,n}(e,i)\left(\frac{r}{a}\right)^l Y_l^m(\theta,\phi)e^{-in\Omega_o t}, \tag{1.8}$$

where $A_{l,m,n}$ depends on the orbital parameters, n is the temporal harmonic of the orbit and Re signifies the real part of a quantity. Ω_o is the averaged orbital frequency of Body 2, $\sqrt{GM_1/a^3}$. Note that here, in a non-rotating frame, we have a tidal frequency of $2\Omega_o$; if we were in a frame rotating with the spin angular velocity of Body 1 there is a Doppler shift and the tidal frequency becomes $2(\Omega_o - \Omega_s)$.

In general, throughout this thesis, we are considering cases where $r \ll a$ and therefore it is a reasonable approximation to consider just the $l = 2$, $n = 2$, $m = 2$ component and define our tidal potential to be

$$\psi = \mathrm{Re}\left[\psi_0 r^2 Y_2^2(\theta,\phi)e^{-i\omega t}\right], \tag{1.9}$$

where $\omega = 2(\Omega_o - \Omega_s)$, $\psi_0 = \frac{G\,M_2}{a^3}A_{2,2,2}$ and $A_{2,2,2} = \sqrt{6\pi/5}$ as is found in Ogilvie (2014) for a circular orbit in the equatorial plane, and therefore relevant for the moons of Jupiter and Saturn.

This can be written in an alternative form where the parameters of the

Body 1	**Body 2**	ϵ
Earth	Moon	5.6×10^{-8}
Jupiter	Io	2.3×10^{-7}
Jupiter	Europa	3.1×10^{-8}
Jupiter	Ganymede	2.3×10^{-8}
Jupiter	Callisto	3.1×10^{-9}
Saturn	Titan	2.8×10^{-8}
Saturn	Enceladus	3.1×10^{-9}
Saturn	Mimas	2.3×10^{-9}
WASP-18	WASP-18b	1.7×10^{-4}
WASP-19	WASP-19b	1.7×10^{-5}
WASP-19b	WASP-19	5.5×10^{-2}

Table 1.1: Example values of the tidal amplitude factor, data taken from Jet Propulsion Laboratory (2022) and Exoplanet.eu (2022).

problem are combined into the parameter $\mathcal{A}_n$,

$$\Psi = \mathrm{Re}\left[\mathcal{A}_n \left(\frac{r}{R_1}\right)^2 Y_2^2(\theta, \phi) e^{-in\Omega_o t}\right], \tag{1.10}$$

where $\mathcal{A}_n = \frac{G\ M_2 R_1^2}{a^3} A_{2,2,n}$.

1.3.2 Tidal dissipation and tidal torque

The tidal amplitude factor, ϵ, is a dimensionless quantity that can be used to estimate the magnitude of the tidal deformation. It is defined to be the ratio of the tidal gravity due to Body 2, $\frac{GM_2 R_1}{d^3}$, and the gravity due to itself, $\frac{GM_1}{R_1^2}$, at the surface of Body 1, i.e.,

$$\epsilon = \frac{M_2}{M_1}\left(\frac{R_1}{d}\right)^3. \tag{1.11}$$

For context, table 1.1 shows some expected values for the tidal amplitude factor for various planet-moon and star-exoplanet systems.

Looking back at Figure 1.6, the tidal forcing causes a tidal bulge in Body 1. If thinking naively this bulge would align with the orbit of Body 2 in the absence of dissipation. However, unless Body 1 is completely elastic there are dissipative effects that cause the bulge to shift either ahead or behind the orbit depending on the relative orbital and spin frequencies.

The perturbed response to the tidal forcing takes the form of the regular solutions to Laplace's equations proportional to $r^{-(l+1)}$ outside Body 1,

$$\Phi' = \mathrm{Re}\left[\mathcal{B}\left(\frac{R}{r}\right)^3 Y_2^2(\theta, \phi) e^{-in\Omega_o t}\right], \tag{1.12}$$

where $\mathcal{B}$ is the complex amplitude of the tidal response to be determined.

It is helpful now to define the complex Love number, which is defined to be the ratio between the perturbed response in Body 1 to the applied tidal potential. The Love number is a dimensionless complex number that can parametrise the tidal response (Love, 1892, 1909),

$$k_l^m(\omega) = \frac{\mathcal{B}}{\mathcal{A}}. \tag{1.13}$$

The real part of the Love number corresponds to the in-phase, elastic response to the forcing, and the imaginary part corresponds to the out-of-phase, dissipative response, which can be linked to the tidal torque and consequential exchange of angular momentum.

Another dimensionless quantity often used to quantify the tidal response is the tidal quality factor, Q, defined by Goldreich (1963) as the ratio of peak energy in one oscillation E^*, to the energy dissipated per oscillation, i.e.

$$Q = \frac{2\pi E^*}{\oint \dot{E}\,\mathrm{d}t}. \tag{1.14}$$

This can be described in terms of the imaginary component of the Love number (Ogilvie, 2014) as

$$|\,\mathrm{Im}[k_l^m(\omega)]| = \frac{k_l}{Q} = \frac{k^{hom}}{Q'}, \tag{1.15}$$

where k_l is the hydrostatic Love number assuming an elastic response, which is real and independent of m, true for a axisymmetric body. k^{hom} is the Love number, for a homogeneous body (for a fluid body $k_2^{hom} = \frac{3}{2}$), and Q' is the modified tidal quality factor.

It is important to note at this point that the tidal quality factor is a linear-fit to what is inherently a non-linear problem and therefore should be used with caution (Goldreich, 1963; Ogilvie, 2014). Therefore, typically it is advantageous to instead use the imaginary part of the Love number which we define to be,

$$\kappa_{l,m,n} = \mathrm{Im}[k_l^m(\omega)]. \tag{1.16}$$

The torque acting on the orbit of Body 2 can be calculated using $\boldsymbol{T} = \boldsymbol{r} \times \boldsymbol{F}$. We can see that the only component of the tidal forcing ($\boldsymbol{F} = -M_2 \boldsymbol{\nabla}\Phi'$) is that perpendicular to $\boldsymbol{r}$, the ϕ component (Ogilvie, 2016). Therefore for an aligned and circular orbit it can be shown that,

$$\boldsymbol{T} = -M_2 r \sin\theta \bigg(- \frac{1}{r\sin\theta}\frac{\partial \Phi'}{\partial \phi}\bigg)\bigg|_{r=a,\theta=\pi/2,\phi=\Omega_o t} \hat{\boldsymbol{z}}, \tag{1.17}$$

$$\boldsymbol{T} = -\,\mathrm{Re}\left(M_2 k_2^2 \frac{GM_2}{4a^3}\frac{R_1^5}{a^3} 2i \right) \hat{\boldsymbol{z}} = \mathrm{Im}(k_2^2)\frac{3GM_2^2 R_1^5}{2a^6}\hat{\boldsymbol{z}}. \tag{1.18}$$

We know from Newton's third law that there is an equal and opposite torque acting on the spin of Body 1, and the associated exchange of angular momentum is

$$\frac{\mathrm{d}L_o}{\mathrm{d}t} = -T. \tag{1.19}$$

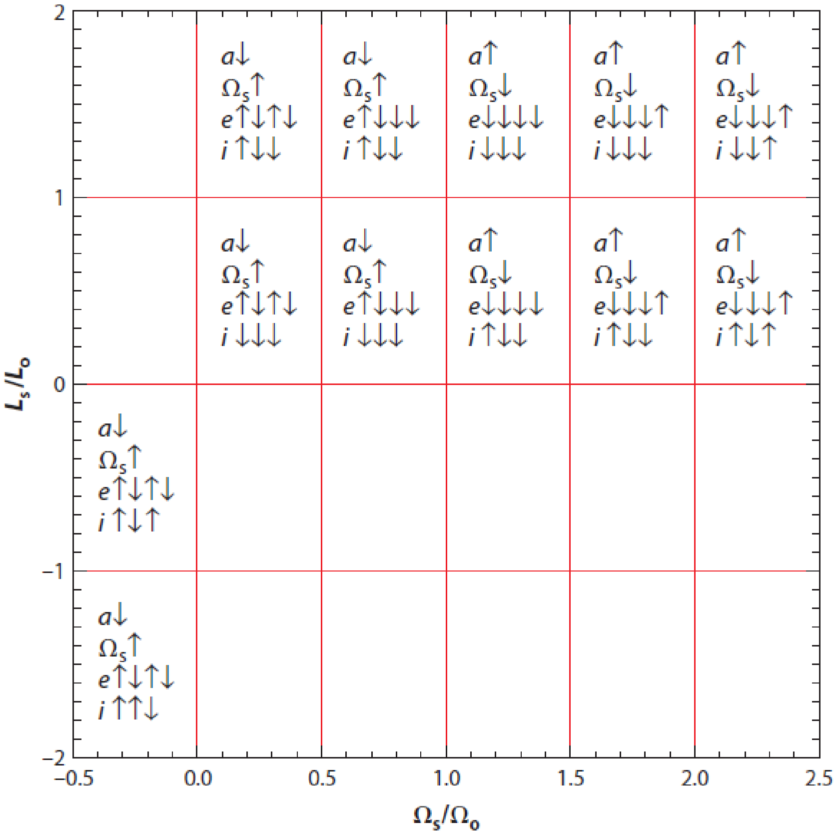

Figure 1.7: Signs of the leading order contributions to the evolution of orbit and spin parameters (the left hand sides of equations 1.20 to 1.23). An upward arrow denotes positive and a downwards arrow negative. Figure taken from Ogilvie (2014).

where $L_o = \frac{M_1 M_2}{M_1+M_2}(GMa)^{\frac{1}{2}}$ and T the component of vector $\boldsymbol{T}$ is the z direction. Substituting in the definition of angular momentum and the calculated torque, the evolution of the semi-major axis, a, can be shown to be (Ogilvie, 2016)

$$\frac{1}{a}\frac{\mathrm{d}a}{\mathrm{d}t} = -3\kappa_{2,2,2}\frac{M_2}{M_1}\left(\frac{R_1}{a}\right)^5 \Omega_o. \tag{1.20}$$

We can see clearly from this equation that there is a direct link between the exchange of angular momentum and the evolution of the orbit of Body 2. The evolution of the spin of Body 1 and other orbital parameters can be derived similarly (Ogilvie, 2014) leading to

$$\frac{1}{\Omega_s}\frac{\mathrm{d}\Omega_s}{\mathrm{d}t} = -\frac{3}{2}\kappa_{2,2,2}\frac{L_o}{L_s}\frac{M_2}{M_1}\left(\frac{R_1}{a}\right)^5\Omega_o, \tag{1.21}$$

$$\frac{1}{e}\frac{\mathrm{d}e}{\mathrm{d}t} = \frac{3}{16}(4\kappa_{2,2,2} - 6\kappa_{2,0,1} + \kappa_{2,2,1} - 49\kappa_{2,2,3})\frac{M_2}{M_1}\left(\frac{R_1}{a}\right)^5\Omega_o, \tag{1.22}$$

$$\frac{1}{i}\frac{\mathrm{d}i}{\mathrm{d}t} = \frac{3}{4}\left[(\kappa_{2,2,2}\left(1-\frac{L_o}{L_s}\right) - (\kappa_{2,1,0} - \kappa_{2,1,2})\left(1+\frac{L_o}{L_s}\right)\right]\frac{M_2}{M_1}\left(\frac{R_1}{a}\right)^5\Omega_o. \tag{1.23}$$

The directions of evolution of each of these quantities depends on the ratio and relative directions of the spin and orbital angular frequencies. The sign of the lowest-order contributions to these quantities can be seen in Figure 1.7, taken from Ogilvie (2014).

Assuming that observations of orbital and spin parameters are sufficiently well constrained, observations over time can be related to the rates of dissipation within planetary interiors. Then, in turn, we can in principle constrain planetary interior models due to the strong dependence of dissipation on the internal structure of a planet.

1.3.3 Observations of tidal evolution

We observe the effects of tidal dissipation and the consequential evolution of the spin-orbit coupling in multiple astrophysical applications.

We consider first our own Earth and its satellite, the Moon. In this case, the Moon's orbital frequency is smaller than the rotational frequency of the Earth, therefore the tidal bulge lags behind the Moon's orbit and the resultant spin-orbit coupling leads to the Moon migrating outwards and to the lengthening of the Earth's day (Munk & MacDonald, 1960; Cartwright, 2000). Some studies show that it is possible that the Moon formed with a highly elliptical orbit (large eccentricity) and has evolved to the current orbit (Ćuk et al., 2016; Ćuk et al., 2021). Due to the obvious importance of understanding Earth's tides, it is a large and active area of research, but not the focus of this study.

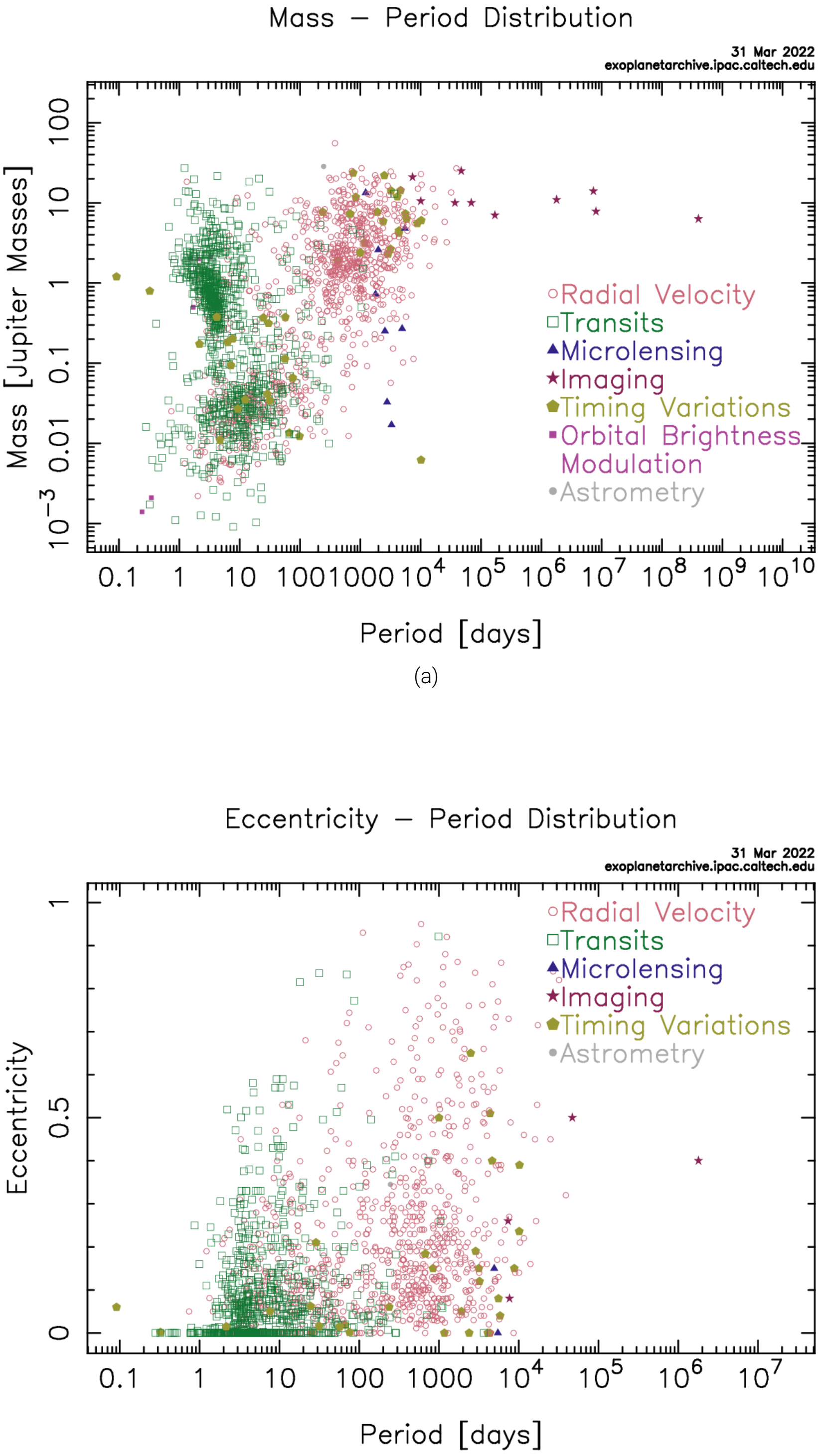

(a)

(b)

Figure 1.8: Mass-period and eccentricity-period plots for confirmed exoplanets, collated from multiple detection methods. Taken from the NASA Exoplanet Archive (2022).

Since 1992 we have been observing exoplanets around stars other than our own Sun. A significant number of these exoplanets are classified to be hot Jupiters. These are planets as massive as Jupiter that are observed orbiting close in to their host star. Figure 1.8a from the NASA exoplanet archive shows the mass vs orbital periods for confirmed exoplanets. It shows a concentration of confirmed planets with Jupiter's mass or larger that have orbital periods of less than approximately 10 Earth days. Figure 1.8b is a similar plot from the NASA exoplanet archive showing eccentricity vs orbital period from which we can see a concentration at low eccentricity. Most formation models expect that planets of this size form further out from their host stars and therefore a mechanism such as tidal dissipation must have occurred to cause inward migration. As scientists have now been observing these planets over several decades we are beginning to collect data on the inward migration of planets. In some cases this can be observed such as in WASP-12b (Yee et al., 2019; Turner et al., 2021) but not in other cases e.g. WASP-18b (Wilkins et al., 2017).

The giant planets in our solar system also supply evidence of tidal migration. In this case we are observing the migration rate of the moons of Jupiter and Saturn. Both planets have a significant number of moons, and the consequential tidal effects vary significantly depending on the size and orbit, as can be estimated for example with the tidal amplitude factor, ϵ. Astrometric measurements have been able to monitor the migration rates of these natural satellites and have established that their moons are migrating outwards at rates that require efficient tidal dissipation inside these planets (Lainey et al., 2009; Lainey et al., 2012, 2017, 2020).

These measurements suggest the rates of tidal dissipation to be much stronger than previously believed (Goldreich & Soter, 1966). It is uncertain how such efficient tidal dissipation can be explained theoretically, therefore suggesting the consideration of additional mechanisms for tidal dissipation. It is this application of tidal migration that we focus our attention on in this thesis.

1.3.4 Possible mechanisms for tidal dissipation

There are multiple possible mechanisms for tidal dissipation that are active areas of research to explain the enhanced dissipation observed, and in reality, the solution is probably a combination of multiple mechanisms.

One possibility, and the one which motivates the research in this thesis, is that the presence of stably-stratified layers, or layers of semi-convection, within giant planets could be enabling the excitation (and subsequent dissipation) of both internal gravity waves and gravito-inertial waves. These layers can also impact on the internal modes in adjacent convection regions. Studies have been done to show the tidal dissipation in convection zones through the excitation and dissipation of inertial waves in convective regions (Ogilvie & Lin, 2004; Wu, 2005a,b; Favier et al., 2014), and in older planet models including a stratified layer near the surface (Ioannou & Lindzen, 1993a,b). The resonant locking of tidal gravito-inertial modes with internal oscillation modes of the planet can cause rapid tidal migration giving a mechanism for tidal dissipation rates to change over time. However this may also require a stable layer to operate effectively (Fuller et al., 2016). It is possible that inner rocky/icy cores of giant planets exhibit visco-elastic properties. This would allow for tidal dissipation within the core, which may lead to additional dissipation (Remus et al., 2012).

Note that the effective viscosity of turbulent convection acting on the non-wavelike tidal flows is unlikely to be important in the case of giant planets and is more likely to play a role in the circularisation of binary/giant star systems or planetary migration around these stars (e.g. Goldreich & Nicholson, 1977; Duguid et al., 2019, 2020).

1.4 Boussinesq approximation

Throughout this thesis we adopt what is regarded as the Boussinesq approximation. This approximation assumes that perturbations to the density are sufficiently small that they can be neglected in places where they occur in the equations. They are only retained in the governing equations when accompanied by gravity, as this term can be large. This is beneficial to allow us to obtain analytical solutions to complement our numerical work. It removes the sound waves from the system, which are often high frequency and can make the system numerically demanding to resolve in numerical simulations. Although this would not be strictly true for planetary applications, we have found this to be a good initial starting point, and in later discussion sections we will comment on the limitations this has introduced.

To avoid repetition we do not include here a full derivation of the Boussinesq equations, as it is done in part later in the thesis, however full derivations can be found in Spiegel & Veronis (1960), or in various text books (e.g. Sutherland, 2010; Vallis, 2017).

The Boussinesq momentum equation in a frame rotating with uniform angular velocity $\mathbf{\Omega}$ is

$$\frac{\partial \boldsymbol{u}}{\partial t} + 2\mathbf{\Omega} \times \boldsymbol{u} = -\frac{1}{\rho_0}\boldsymbol{\nabla} p + b\hat{\boldsymbol{r}} + \nu \boldsymbol{\nabla}^2 \boldsymbol{u} + \boldsymbol{f}, \tag{1.24}$$

where $\boldsymbol{u}$ and p are the Eulerian perturbations to velocity and pressure, ρ_0 is the background reference density and ν the kinematic viscosity which is assumed to be constant. We define the buoyancy variable b to be $b = -g\frac{\rho}{\rho_0}$ and has units of acceleration; the only term in which the density perturbation ρ has been retained. $\boldsymbol{f}$ denotes any external forcing (in our case this would be the tidal forcing). Note that in Chapters 4 to 6 we use a different definition of b to aid manipulation of g, however it is mathematically equivalent. Neglecting density perturbations in mass conservation gives,

$$\rho_0 \nabla \cdot \boldsymbol{u} = 0. \tag{1.25}$$

A combination of the thermodynamic equation and the equation of state becomes,

$$\frac{\partial b}{\partial t} + u_r N^2 = \kappa \boldsymbol{\nabla}^2 b, \tag{1.26}$$

where N^2 is the Brunt-Väisälä frequency or buoyancy frequency, and κ the thermal diffusivity which is assume to be constant. The Brunt-Väisälä frequency is defined as

$$N^2 = g\left(\frac{1}{\Gamma_1}\frac{\mathrm{d}\ln p_0}{\mathrm{d}r} - \frac{\mathrm{d}\ln \rho_0}{\mathrm{d}r}\right). \tag{1.27}$$

where $\Gamma_1 = \left(\frac{\partial \ln p_0}{\partial \ln \rho_0}\right)_{\mathrm{ad}}$ is the first adiabatic exponent. It is here where the information on the stratification is contained. Often (and throughout this study) for ease of interpretation we approximate this by assuming $\Gamma_1 \to \infty$, therefore neglecting the first term. This allows us to relate the buoyancy frequency to density gradients by,

$$N^2 \approx -\frac{g}{\rho_0}\frac{\mathrm{d}\rho_0}{\mathrm{d}r}. \tag{1.28}$$

The stability of a fluid can be related to the buoyancy frequency where $N^2 > 0$ describes a stably stratified medium, $N^2 < 0$ a convective medium and $N^2 = 0$ a well-mixed neutrally stratified medium.

1.5 Internal waves

As we are considering the dissipation of tidally forced waves, we now introduce the main types of internal waves. In general waves are classified by the restoring force generating them. Having made the Boussinesq approximation (and as we are assuming there are no magnetic effects) we are left with gravity and the Coriolis force to act as restoring forces. We therefore consider the following main forms of waves:

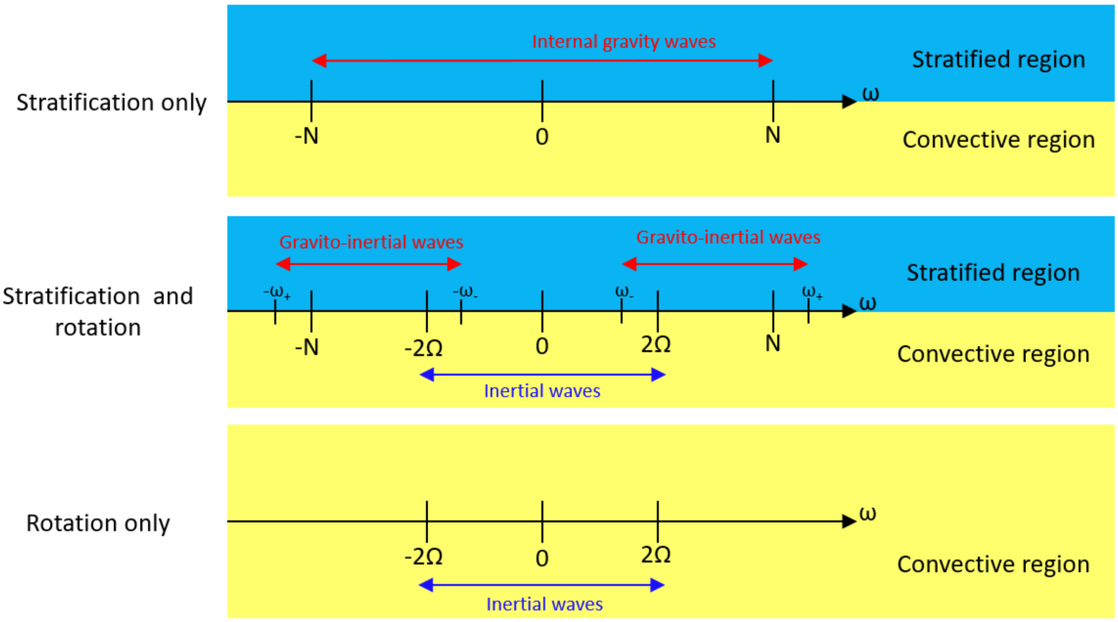

Figure 1.9: Figure showing the possible range of internal modes in stratified and convective regions of planets, adapted from Mathis et al. (2014).

- **Internal gravity waves (g-modes)** are wave-like perturbations occurring when there is a stable density gradient and gravity acts as a restoring force.
- **Surface gravity (f-mode) / interfacial waves** are oscillations of the boundary between fluids of two different densities.
- **Inertial waves** occur in a rotating body where the Coriolis acceleration acts as a restoring force.

Of course, in general applications are more complicated than isolated single wave type behaviour. In some cases, there is a significantly dominant force but in others this can lead to modes being split and mixed modes. In particular for this study, we consider the existence of gravito-inertial waves. Figure 1.9 shows the regimes in which these modes are expected to exist and will be expanded upon in the rest of this section. Neglected from this study are waves with other restoring forces, most notably acoustic waves (p-modes) which are driven by pressure variations neglected by taking the Boussinesq approximation, and Alfvén waves where tension in magnetic field lines acts as a restoring force.

Internal gravity waves

By considering perturbations of the form $\exp\left(i(\boldsymbol{k}\cdot\boldsymbol{r}-\omega t)\right)$, where frequency ω and wavenumber k are real, and considering equations 1.24 and 1.26 without rotation ($\Omega = 0$) or dissipative effects ($\nu = \kappa = 0$) the following dispersion relation can be found (Sutherland, 2010; Vallis, 2017; Christensen-Dalsgaard, 2014) for constant N

$$\omega^2 = \frac{N^2\,k_\perp^2}{k^2}, \tag{1.29}$$

where $k_\perp$ is the component of the wave number perpendicular to the direction of gravity, e.g. with g and N constant and in the z/r direction, in Cartesian geometry $k_\perp = \sqrt{k_x^2 + k_y^2}$ and $k = \sqrt{k_x^2 + k_y^2 + k_z^2}$, and in spherical geometry $k_\perp = \sqrt{l(l+1)}/r$.

From this we can see that as $k^2 \geq k_\perp^2$ this has a maximum value of N^2 and therefore the possible frequency range of internal gravity waves is bounded by $\omega < |N|$, see top panel of Figure 1.9. We note additionally for internal waves to form the fluid must be stably stratified, therefore $N^2 > 0$.

The phase velocity and group velocity can be shown to be,

$$\boldsymbol{c_p} = \frac{\omega}{k}\hat{\boldsymbol{k}} = \frac{N\,k_\perp}{k^2}\hat{\boldsymbol{k}}, \tag{1.30}$$

and,

$$\boldsymbol{c_g} = \frac{\partial \omega}{\partial \boldsymbol{k}} = \frac{N\,k_z}{k^3\,k_\perp}\left(k_x k_z, k_y k_z, -k_\perp^2\right), \tag{1.31}$$

from which we note that the group and phase velocity for an internal gravity wave are perpendicular to each other i.e. $\boldsymbol{c_p} \perp \boldsymbol{c_g}$.

Inertial waves

Similarly to above, by considering the same form of perturbation ($\exp\left(i(\boldsymbol{k}\cdot\boldsymbol{r}-\omega t)\right)$), and again neglecting dissipative effects ($\nu = \kappa = 0$), but now considering $N = 0$ and $\Omega \neq 0$, the dispersion relation for inertial waves can be shown to be (e.g. Rieutord, 2009; Sutherland, 2010; Christensen-Dalsgaard, 2014).

$$\omega^2 = \frac{(2\boldsymbol{\Omega} \cdot \boldsymbol{k})^2}{k^2}, \tag{1.32}$$

where k_z is the wavenumber in the direction parallel to the rotation axis. Again, we note that the range of frequencies is bounded, this time $\omega < |2\Omega|$. In general, we typically expect $N > 2\Omega$; therefore although both are considered to be low frequency waves, inertial waves are thought to occupy a lower range than internal gravity waves in most applications, see Figure 1.9. We also note that the frequency is independent of the magnitude of the wavenumber, depending on rotation rate and propagation angle only, therefore waves of different wavenumbers can exist with the same frequencies.

The phase and group velocities can be shown to be (e.g. André et al., 2017),

$$\boldsymbol{c_p} = \frac{\omega}{k}\hat{\boldsymbol{k}} = \mathrm{sgn}(\omega)\frac{(2\boldsymbol{\Omega} \cdot \boldsymbol{k})}{k^2}\hat{\boldsymbol{k}}, \tag{1.33}$$

and

$$\boldsymbol{c_g} = \frac{\partial \omega}{\partial \boldsymbol{k}} = \mathrm{sgn}(\omega)\frac{\boldsymbol{k} \times (2\boldsymbol{\Omega} \times \boldsymbol{k})}{k^3}, \tag{1.34}$$

which as for internal gravity waves are perpendicular.

Gravito-inertial modes

When considering both constant stratification and rotation with similar magnitudes it is possible to establish mixed gravito-inertial modes. Still neglecting viscosity and thermal diffusivity, the dispersion relation can be shown to be (e.g. Dintrans et al., 1999; André et al., 2017),

$$\omega^2 = \frac{N^2\, k_\perp^2}{k^2} + \frac{(2\boldsymbol{\Omega} \cdot \boldsymbol{k})^2}{k^2}. \tag{1.35}$$

The frequency range for these modes can be found for example by considering the Poincaré equation (see Rieutord, 2009; Mathis et al., 2014) where it can be shown that the critical surfaces which separate the regions in which a gravito-inertial wave can and cannot propagate satisfy

$$\omega^4 - (N^2 + 4\Omega^2)\omega^2 + 4\Omega^2 N^2 \cos^2\theta = 0, \tag{1.36}$$

where θ is the angle from the rotation axis. This can be solved to find,

$$\omega_\pm = \frac{1}{2}\sqrt{(N^2 + 4\Omega^2) \pm \sqrt{(N^2 + 4\Omega^2) - (4\Omega N \cos\theta)^2}}. \tag{1.37}$$

Therefore the frequency range of gravito-inertial modes can be shown to be $\omega_- < \omega < \omega_+$ which has limits of $0 < \omega < \sqrt{N^2 + 4\Omega^2}$.

The group velocity can be shown to be (e.g. André et al., 2017),

$$\boldsymbol{c_p} = \frac{\omega}{k}\hat{\boldsymbol{k}} = \frac{\mathrm{sgn}(\omega)}{k^2}\sqrt{N^2\, k_\perp^2 + (2\boldsymbol{\Omega}\cdot\boldsymbol{k})^2}, \tag{1.38}$$

and,

$$\boldsymbol{c_g} = \frac{\partial\omega}{\partial\boldsymbol{k}} = \frac{\mathrm{sgn}(\omega)}{\omega}\left[N^2\left(\frac{k_z}{k}\right)\frac{\boldsymbol{k}\times(-\hat{\boldsymbol{e}}_{\boldsymbol{z}}\times\boldsymbol{k})}{k^3} + \left(\frac{2\boldsymbol{\Omega}\cdot\boldsymbol{k}}{k}\right)\frac{\boldsymbol{k}\times(2\boldsymbol{\Omega}\times\boldsymbol{k})}{k^3}\right]. \tag{1.39}$$

Chapter 2

Free modes of a density staircase in spherical geometry

In this first chapter we aim to gain some understanding of the free modes of an idealised giant planet containing stably-stratified layers or a density staircase. We analyse how they depend on the parameters of the problem. We will build on this by exploring wave propagation and tidal dissipation in later chapters.

We will do this by considering the modes of the possible internal waves in spherical geometry. We start with an isolated region consisting of well-mixed convective layers separated by infinitesimally thin interfaces, i.e. a density staircase. This chapter extends the work of Belyaev et al. (2015) and André et al. (2017) to spherical geometry. We illustrate the regions in a giant planet where stable layers could be present in Figure 2.1, although we focus our attention on studying wave propagation in either the stable layer near the core of the planet or near the H/He molecular to metallic transition radius, where helium rain may occur.

2.1 Model

We adopt the Boussinesq approximation (Spiegel & Veronis, 1960) for simplicity, see Section 1.4 for more details, and to facilitate understanding before a more complicated physical model is studied. This is appropriate for studying waves with shorter wavelengths than a pressure or density scale height, and with phase speeds that are slow relative to the sound speed. This is likely to be a reasonable approximation for studying the free modes of a density staircase, though it is strictly not valid for studying the largest wavelength waves in a planet. We also adopt the Cowling approximation (Cowling, 1941), thereby neglecting perturbations to the gravitational potential (e.g. $\Phi = \Phi_0(r)$, where Φ_0 is the gravitational potential in hydrostatic equilibrium). This is a reasonable approximation for studying internal waves, particularly those with (horizontal and radial) wavelengths that are shorter than the planetary radius. It is likely that many low frequency tidally forced waves are in this regime making both these approximations reasonable.

In this chapter we also neglect viscous and thermal dissipation, which will be considered in later chapters. We are studying only the free resonances, therefore consider an unforced system. This allows the system to be solved analytically.

2.1.1 Governing equations

We briefly outline the derivation of the linear adiabatic equations of motion describing the non-radial oscillations of a non-rotating spherical planet (Gough, 1993; Thompson, 2006; Christensen-Dalsgaard, 2014). We use spherical polar coordinates (r, θ, ϕ), where $r = 0$ corresponds to the centre of the planet, and adopt a basic state that is a spherically-symmetric planetary model in hydrostatic equilibrium, with density $\rho_0(r)$, pressure $p_0(r)$ and gravitational potential $\Phi_0(r)$. We consider linear perturbations to this basic state of the form

$$p(\boldsymbol{r}, t) = p_0(r) + p'(\boldsymbol{r}, t),$$

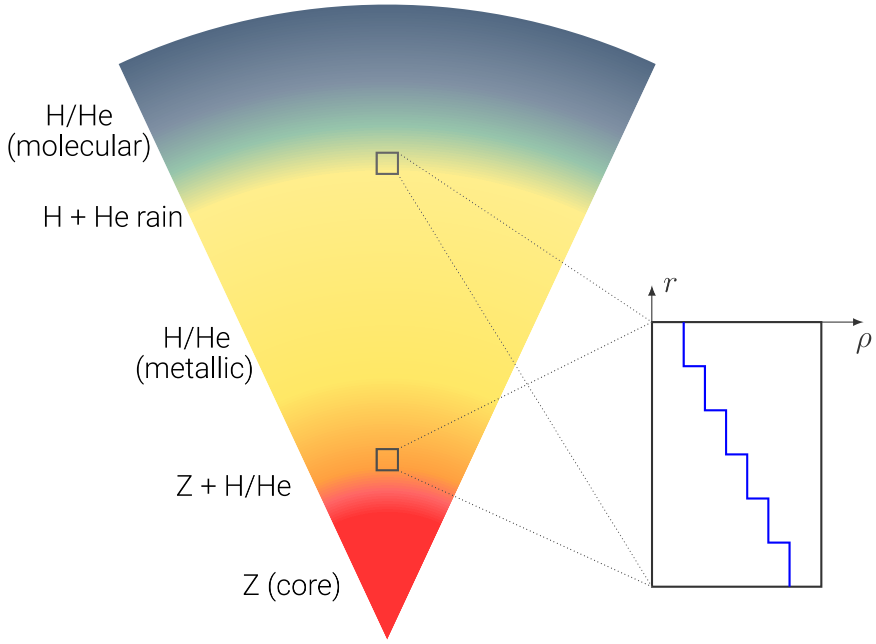

Figure 2.1: Diagram showing the expected radial locations of stably-stratified layers in giant planet interiors. Figure adapted from André et al. (2017).

and similarly for other variables, where a prime denotes the Eulerian perturbation. $\boldsymbol{\xi}$ is the Eulerian displacement such that $\boldsymbol{u} = \partial\boldsymbol{\xi}/\partial t$ is the fluid velocity. The resulting linearised adiabatic (thus far fully compressible) equations of motions are,

$$\rho' + \boldsymbol{\nabla}\cdot(\rho_0\boldsymbol{\xi}) = 0, \tag{2.1}$$

$$\rho_0\frac{\partial^2\boldsymbol{\xi}}{\partial t^2} = -\boldsymbol{\nabla}p' + \rho'\boldsymbol{g}_0, \tag{2.2}$$

$$p' + \boldsymbol{\xi}\cdot\boldsymbol{\nabla}p_0 = \frac{\Gamma_1 p_0}{\rho_0}\left(\rho' + \boldsymbol{\xi}\cdot\boldsymbol{\nabla}\rho_0\right), \tag{2.3}$$

where $\Gamma_1 = \left(\frac{\partial \ln p_0}{\partial \ln \rho_0}\right)_{\mathrm{ad}}$ is the first adiabatic exponent. The gravitational acceleration is $\boldsymbol{g}_0 = -\nabla\Phi_0$ where perturbations to gravitational potential ($\nabla^2\Phi' = 4\pi G\rho'$) have been neglected due to the Cowling approximation.

The displacement is split into radial and horizontal components,

$$\boldsymbol{\xi} = \xi_r\hat{\boldsymbol{r}} + \boldsymbol{\xi}_h,$$

where $\hat{\boldsymbol{r}}\cdot\boldsymbol{\xi}_h = 0$, and $\hat{\boldsymbol{r}}$ is the radial unit vector. Since the basic state is static and spherically-symmetric, we may expand perturbations using spherical harmonics with harmonic time-dependence, i.e.

$$\xi_r(r,\theta,\phi,t) = \tilde{\xi}_r(r) Y_l^m(\theta,\phi) \mathrm{e}^{-i\omega t},$$

and similarly for other variables, where the physical quantity is the real part of this expression, and we use orthonormalised spherical harmonics Y_l^m. Substituting this into equations 2.1 to 2.3, and using these to eliminate $\tilde{\boldsymbol{\xi}}_h$ and $\tilde{\rho}$, we obtain:

$$\frac{\mathrm{d}\tilde{\xi}_r}{\mathrm{d}r} = -\left(\frac{2}{r} + \frac{1}{\Gamma_1 p_0}\frac{\mathrm{d}p_0}{\mathrm{d}r}\right)\tilde{\xi}_r + \frac{1}{\rho_0\omega^2 c^2}\left(S_l^2 - \omega^2\right)\tilde{p}', \tag{2.4}$$

$$\frac{\mathrm{d}\tilde{p}'}{\mathrm{d}r} = \rho_0\left(\omega^2 - N^2\right)\tilde{\xi}_r + \frac{1}{\Gamma_1 p_0}\frac{\mathrm{d}p_0}{\mathrm{d}r}\tilde{p}', \tag{2.5}$$

where the squared adiabatic sound speed is

$$c^2 = \Gamma_1 \frac{p_0}{\rho_0}, \tag{2.6}$$

the squared Lamb frequency is

$$S_l^2 = \frac{l(l+1)c^2}{r^2}, \tag{2.7}$$

and the squared buoyancy frequency, or Brunt-Väisälä frequency, is

$$N^2 = g\left(\frac{1}{\Gamma_1}\frac{\mathrm{d}\ln p_0}{\mathrm{d}r} - \frac{\mathrm{d}\ln\rho_0}{\mathrm{d}r}\right). \tag{2.8}$$

We have also defined $\boldsymbol{g}_0 = -g(r)\hat{\boldsymbol{r}}$. The radial dependence of $g(r)$ involves the density structure of the entire region within that radius, not just the staircase.

Note that in general

$$N^2 = -\frac{T_0\alpha_T}{c_p}\boldsymbol{g}_0 \cdot \nabla s_0, \tag{2.9}$$

where α_T is the coefficient of thermal expansion, c_p is the specific heat capacity at constant pressure, and T_0 and s_0 are the temperature and specific entropy profiles for the basic state. Specific entropy is defined to be $s_0 = c_p \ln(p/\rho_0^{\Gamma_1})$ and we have assumed we are considering a perfect gas. This means that $N^2 \propto \partial_r s_0$. In the next section, we will specify a background profile of $s_0(r)$ that represents a layered profile, and we are strictly considering an "entropy staircase", once we correctly account for the difference between the density and entropy of the gas.

For clarity of presentation and comparison with prior work, we will refer to this as a "density staircase", which will be represented by a particular choice of $\rho_0(r)$, that is related to the buoyancy frequency in the incompressible limit by

$$N^2 \approx -\frac{g}{\rho_0}\frac{\mathrm{d}\rho_0}{\mathrm{d}r}. \tag{2.10}$$

To simplify our analysis we assume that the background variations in density and pressure are much smaller than their maximum values, and that the wave speed is much smaller than the adiabatic sound speed, or equivalently, that $\omega^2 \ll S_l^2$ and $\Gamma_1 \to \infty$. The above system then reduces to

$$\frac{\mathrm{d}\tilde{\xi}_r}{\mathrm{d}r} = -\frac{2\tilde{\xi}_r}{r} + \frac{1}{\rho_0\omega^2}\frac{l(l+1)}{r^2}\tilde{p}', \tag{2.11}$$

$$\frac{\mathrm{d}\tilde{p}'}{\mathrm{d}r} = \rho_0\omega^2\left(1 - \frac{N^2}{\omega^2}\right)\tilde{\xi}_r, \tag{2.12}$$

which can be combined to give

$$\frac{\mathrm{d}^2\tilde{\xi}_r}{\mathrm{d}r^2} + \frac{4}{r}\frac{\mathrm{d}\tilde{\xi}_r}{\mathrm{d}r} + \left[\left(\frac{N^2}{\omega^2} - 1\right)l(l+1) + 2\right]\frac{\tilde{\xi}_r}{r^2} = 0. \tag{2.13}$$

We note that equation 2.13 can be simplified using the substitution $\chi = r^2\tilde{\xi}_r$, reducing it to the form,

$$\frac{\mathrm{d}^2\chi}{\mathrm{d}r^2} + \left(\frac{N^2}{\omega^2} - 1\right)l(l+1)\frac{\chi}{r^2} = 0, \tag{2.14}$$

where the effective radial wavenumber can therefore be more easily identified as,

$$k_r^2 = \frac{l(l+1)}{r^2}\left(\frac{N^2}{\omega^2} - 1\right). \tag{2.15}$$

Equivalence with the Boussinesq approximation

We can show that equation 2.13 is equivalent to adopting the Boussinesq approximation from the outset, which we now outline starting from the linearised Boussinesq system (neglecting viscosity and thermal diffusion).

$$\frac{\partial \boldsymbol{u}}{\partial t} = -\frac{1}{\rho_0}\boldsymbol{\nabla} p + b\boldsymbol{r}, \tag{2.16}$$

$$\frac{\partial b}{\partial t} + u_r \frac{N^2}{r} = 0, \tag{2.17}$$

where $b = -\frac{g\rho}{r\rho_0}$ is a buoyancy variable, N^2 is defined by equation 2.10, and $\boldsymbol{u}$ is incompressible. We note that the definition of b here is different to that used in Chapters 4 to 6, which is addressed in those chapters. The radial and horizontal components of the Eulerian displacement satisfy

$$\frac{\partial^2 \xi_r}{\partial t^2} = -\frac{1}{\rho_0}\frac{\partial p}{\partial r} + rb, \tag{2.18}$$

$$\frac{\partial^2 \boldsymbol{\xi}_h}{\partial t^2} = -\frac{1}{\rho_0}\boldsymbol{\nabla}_h p. \tag{2.19}$$

Using incompressibility, together with equation 2.19, we can eliminate $\boldsymbol{\xi}_h$ to obtain

$$\frac{1}{r^2}\frac{\partial}{\partial r}\left(r^2 \frac{\partial^2 \xi_r}{\partial t^2}\right) - \frac{1}{\rho_0}\boldsymbol{\nabla}_h^2 p = 0. \tag{2.20}$$

When perturbations are expanded using spherical harmonics with harmonic time-dependence (as previously done), and with some algebra, equations 2.17, 2.18, and 2.20, can be combined to eliminate $\tilde{b}$ and $\tilde{p}$, resulting in equation 2.13.

2.2 Density profile

We consider a staircase like that shown in Figure 2.2. We define our (semi-convective) density staircase to have a typical radius r_0 (i.e. 1 in dimensionless radii) from the centre of the planet, which represents its inner radius. The staircase

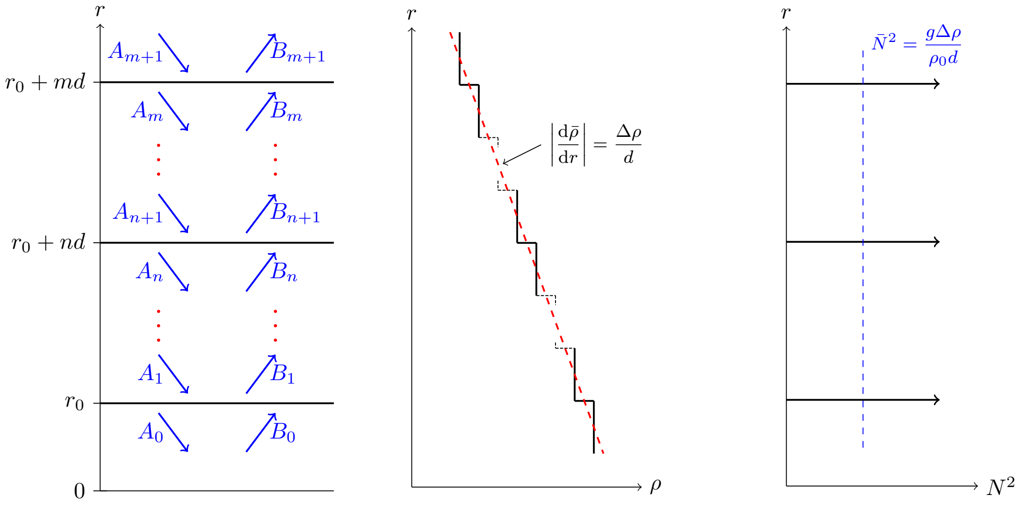

(a) (b) (c)

Figure 2.2: Illustrations of our model, which consists of m steps of size d, separated by $m+1$ interfaces with density jumps of $\Delta\rho$, with initial radius r_0. In Panel a amplitudes of the downward (A_n) and upward (B_n) propagating waves in each layer are shown. Panel b shows the density profile with a mean gradient $\frac{\Delta\rho}{d}$, shown by the red dashed line. Panel c shows the corresponding buoyancy frequency squared, consisting of δ-functions with mean value $\bar{N}^2 = \frac{g\Delta\rho}{\rho_0 d}$. Figures adapted from André et al. (2017).

consists of m steps of well-mixed (constant density), convective fluid layers with uniform depth d, in which $N = 0$. These layers are separated by $m+1$ equal-sized density jumps of magnitude $\Delta\rho$. In reality, we might expect a staircase to possess a range of layer depths and density jumps, but we will primarily adopt equal-sized layers with equal density jumps to simplify the analysis. Extending our model to explore a range of layer depths and density jumps is straightforward, and is partly explored later in Section 3.2.2 (see also Sutherland, 2016; André et al., 2017, in Cartesian geometry). We define a dimensionless parameter

$$\epsilon = \frac{d}{r_0}, \tag{2.21}$$

which represents the fractional depth of each convective layer relative to the typical inner radius of the staircase. We usually expect $\epsilon \ll 1$ (e.g. Leconte & Chabrier, 2012), though this need not be the case if the layer is close to the centre of the planet.

We will vary the properties of the end regions that connect to the inner and outer radii of the staircase. First, we will consider an isolated staircase in which, similarly to the steps, the end regions are also well-mixed convective layers with $N = 0$. This means gravity waves are evanescent in these layers. In the absence of a solid core, if we include $r = 0$, a regularity condition must be imposed there. We will generally adopt a core of radius $r_c \ll r_0$, which we will treat as perfectly absorbing for the purposes of calculating the transmission of waves through the staircase.

The density profile is modelled as a series of δ-functions at each interface between adjacent steps, such that the mean buoyancy frequency is $\bar{N}$, i.e.,

$$N^2 = \sum_{n=0}^{m} d\bar{N}^2 \delta(r_0 + nd - r), \tag{2.22}$$

where we define

$$\bar{N}^2 \equiv \frac{g\Delta\rho}{\rho_0 d}, \tag{2.23}$$

ρ_0 is the (constant) reference density, and $\Delta\rho$ is the density jump at each interface. The factor of d in equation 2.22 arises from combining the density gradient, $\frac{\mathrm{d}\rho}{\mathrm{d}r} = -\Delta\rho\delta(r - r_0 - nd)$, and the given definition of $\bar{N}$. This preserves the overall dimensions of the quantity as it balances the inverse length units of the δ-function when its argument has units of length. As previously discussed, we are strictly considering entropy jumps and would not necessarily expect to have equal-sized density jumps, but we consider them here to obtain concrete analytical results.

In what follows we non-dimensionalise quantities, using a mean buoyancy frequency $\bar{N}^{-1}$ as our unit of time, and a typical radius r_0 as our unit of length. However, we choose to retain (but set to 1 in calculations) $\bar{N}$ and r_0 in some formulae and figures, even if these strictly should not appear, so that they can be more easily tracked in the derivations.

2.3 Solutions for the radial displacement in the staircase

When we substitute equation 2.22 into equation 2.13 we obtain a discontinuous differential equation, so we may obtain the solution in each region separately as long as we apply suitable matching conditions at the interfaces. Within the n-th convective step $N^2 = 0$ so that

$$\frac{\mathrm{d}^2\xi_n}{\mathrm{d}r^2} + \frac{4}{r}\frac{\mathrm{d}\xi_n}{\mathrm{d}r} - \frac{l(l+1)-2}{r^2}\xi_n = 0, \tag{2.24}$$

which has solutions for the radial displacement

$$\xi_n = A_n r^{l-1} + B_n r^{-l-2}. \tag{2.25}$$

We have omitted the subscript r from ξ_r, and replaced it with a new subscript n to identify the appropriate step number to which the solution applies. The radial displacement across the entire region is therefore described by

$$\xi = \begin{cases} A_0 r^{l-1} + B_0 r^{-l-2} & \frac{r_c}{r_0} < r < 1, \\ A_n r^{l-1} + B_n r^{-l-2} & r_{n-1} < r < r_n, \\ A_{m+1} r^{l-1} + B_{m+1} r^{-l-2} & r > 1 + m\epsilon, \end{cases} \tag{2.26}$$

where $r_n = 1 + n\epsilon$, and $n = 1, \ldots, m$.

It can be verified that the coefficients A_n and B_n denote the upwards and downwards component of the solution, respectively, by considering the flux of the relevant component, see Section 3.1.1 for details on the flux calculation.

Solution for radial displacement in a stratified region

If we instead consider an extended region with a spatially uniform (constant) buoyancy frequency $N = \bar{N}$, then equation 2.13 would have the solution

$$\xi = Ar^{\lambda_+} + Br^{\lambda_-}, \tag{2.27}$$

where A and B denote the amplitude of the downward/upward propagating wave, and

$$\lambda_{\pm} = -\frac{3}{2} \pm \frac{1}{2}\sqrt{1 + 4\left(1 - \frac{\bar{N}^2}{\omega^2}\right)l(l+1)}. \tag{2.28}$$

We will later use this solution when we consider the transmission of waves through a staircase sandwiched by two stably-stratified layers, and also when we compare the frequencies of the free modes of a staircase with those of a uniformly stably-stratified layer.

2.3.1 Interface conditions and transfer matrices

Since equation 2.13 is a second-order differential equation in r, we must apply two boundary conditions at each interface. Here, we generalise those used in André et al. (2017) to spherical geometry. Firstly, we must ensure that there is no separation of the fluid on either side of each interface, therefore ξ must be continuous there. This requires

$$\xi_{n+1}(1 + n\epsilon) = \xi_n(1 + n\epsilon), \tag{2.29}$$

and using equation 2.26 we find

$$A_{n+1} - A_n + \big(B_{n+1} - B_n\big)\big(1 + n\epsilon\big)^{-2l-1} = 0. \tag{2.30}$$

Our second condition follows from the requirement that the momentum flux, and therefore the pressure perturbation, is continuous across each interface. We obtain this condition by integrating equation 2.13 over a small volume of radial extent 2Δ around an interface. For the n-th interface, we obtain,

$$\int_{1+n\epsilon-\Delta}^{1+n\epsilon+\Delta} r^2\frac{\mathrm{d}^2\xi}{\mathrm{d}r^2}\mathrm{d}r + \int_{1+n\epsilon-\Delta}^{1+n\epsilon+\Delta} 4r\frac{\mathrm{d}\xi}{\mathrm{d}r}\mathrm{d}r =$$

$$\int_{1+n\epsilon-\Delta}^{1+n\epsilon+\Delta} (l(l+1)-2)\xi\mathrm{d}r - \int_{1+n\epsilon-\Delta}^{1+n\epsilon+\Delta} \frac{N^2}{\omega^2}l(l+1)\xi\mathrm{d}r. \quad (2.31)$$

We can then take the limit of vanishing volume, such that Δ tends to 0, to derive the boundary condition. We use integration by parts on the left hand side (LHS) of the equation and apply the continuity of ξ (equation 2.29), so that the limit $\Delta \to 0$ leads to

$$\mathrm{LHS} = \left(1+n\epsilon\right)^2\left[\frac{\mathrm{d}\xi_{n+1}}{\mathrm{d}r} - \frac{\mathrm{d}\xi_n}{\mathrm{d}r}\right]_{r=1+n\epsilon}. \quad (2.32)$$

On the right hand side (RHS), we also apply the continuity of ξ such that on taking $\Delta \to 0$ the first term does not contribute. Upon substitution of equation 2.22 the second term becomes

$$\mathrm{RHS} = -\frac{\bar{N}^2\epsilon}{\omega^2}l(l+1)\int_{1+n\epsilon-\Delta}^{1+n\epsilon+\Delta} \delta(1+n\epsilon-r)\xi\mathrm{d}r. \quad (2.33)$$

After integration we obtain our second interface condition:

$$\left[\frac{\mathrm{d}\xi_{n+1}}{\mathrm{d}r} - \frac{\mathrm{d}\xi_n}{\mathrm{d}r}\right]_{r=1+n\epsilon} = -\frac{\bar{N}^2 l(l+1)\epsilon}{\omega^2(1+n\epsilon)^2}\xi_n\bigg|_{r=1+n\epsilon}. \quad (2.34)$$

Using equation 2.26 we then find

$$(l-1)(A_{n+1}-A_n) - (l+2)\Big(B_{n+1} - B_n(1+n\epsilon)^{-2l-1}\Big)$$

$$= \frac{-\bar{N}^2 l(l+1)\epsilon}{\omega^2(1+n\epsilon)^2}\Big[A_n(1+n\epsilon) + B_n(1+n\epsilon)^{-2l}\Big]. \quad (2.35)$$

The two interface conditions (equations 2.30 and 2.35) allow the solution in each step to be written in terms of the solution in an adjacent step. Therefore, with some algebra, the coefficients in adjacent layers are related by

$$\begin{bmatrix} A_{n+1} \\ B_{n+1} \end{bmatrix} = T_n \begin{bmatrix} A_n \\ B_n \end{bmatrix}, \tag{2.36}$$

where the transfer matrix T_n is defined as,

$$T_n = \begin{bmatrix} 1 - \dfrac{\epsilon l(l+1)\bar{N}^2}{(2l+1)(1+n\epsilon)\omega^2} & \dfrac{-\epsilon l(l+1)\bar{N}^2}{(2l+1)\left(1+n\epsilon\right)^{2(l+1)}\omega^2} \\ \dfrac{\epsilon l(l+1)(1+n\epsilon)^{2l}\bar{N}^2}{(2l+1)\omega^2} & 1 + \dfrac{\epsilon l(l+1)\bar{N}^2}{(2l+1)(1+n\epsilon)\,\omega^2} \end{bmatrix}. \tag{2.37}$$

We identify that we can consider two limits; first we can recover the results found in Cartesian geometry in Belyaev et al. (2015), Sutherland (2016) and André et al. (2017) by taking the limits $l \gg 1$, $n\epsilon \ll 1$ and $n\epsilon l \ll 1$, identify $k_\perp^2 = \frac{l(l+1)}{r_0^2}$ and noting that in the evanescent region $k_\perp = k_r$.

$$T_n = \begin{bmatrix} 1 - k_\perp d\dfrac{\bar{N}^2}{\omega^2} & -k_\perp d\dfrac{\bar{N}^2}{\omega^2} \\ k_\perp d\dfrac{\bar{N}^2}{\omega^2} & 1 + k_\perp d\dfrac{\bar{N}^2}{\omega^2} \end{bmatrix}. \tag{2.38}$$

In the second case we take $\epsilon \to 0$, therefore removing the interfaces, and note that T_n reduces to the identity matrix.

This formalism allows us to determine the solution in the $(m+1)$-th layer in terms of the solution in the 0-th layer by repeatedly applying the transfer matrix. Note that T_n depends on the radius of the n-th interface, which complicates the following analysis compared with the Cartesian case (even with constant d and $\Delta\rho$) in André et al. (2017). But we may still define a 2×2 matrix such that,

$$\begin{bmatrix} A_{m+1} \\ B_{m+1} \end{bmatrix} = X \begin{bmatrix} A_0 \\ B_0 \end{bmatrix}, \tag{2.39}$$

where

$$X = T_m T_{m-1} \dots T_1 T_0 \tag{2.40}$$

relates the solution in the end regions. With appropriate choices of the end regions, this formalism allows us to analyse the free modes of a density staircase (Section 2.4).

2.4 Free modes of a density staircase

We now derive a dispersion relation that describes the free internal modes of a density staircase. We will consider three cases

1. A finite staircase confined between two well-mixed convective regions.
2. A finite staircase confined by a solid wall at either end.
3. A finite staircase with a solid wall at the inner boundary (closest to the core) and a well-mixed convective region at the outer boundary.

The first would be most representative of a staircase forming near a H/He transition region and the third a staircase forming just above a solid inner core. In each case we analyse the properties of the free modes and how they depend on the parameters describing the staircase.

2.4.1 Finite staircase embedded in a convective medium

Our first example considers a finite staircase embedded in a convective medium, which could represent a staircase in the helium rain region. We enforce boundary conditions such that the solution decays away from the first and last interface as would be expected in a convective medium. This corresponds with setting $B_0 = 0$ and $A_{m+1} = 0$, the coefficient of the non-decaying components of the solution.

Therefore, by considering equation 2.39 the top left entry of X is then required to be zero, i.e.,

$$X_{1,1} = 0. \tag{2.41}$$

This represents a polynomial in ω^2, which is the dispersion relation describing the free modes of the staircase. The polynomial has degree $(m+1)$, implying that there are an equal number of (oppositely-signed pairs of) free modes in the system as there are interfaces in the staircase (see also Belyaev et al., 2015; André et al., 2017).

Single step ($m = 1$)

We first solve equation 2.41 for a staircase consisting of a single convective step and two interfaces ($m = 1$) which gives the dispersion relation

$$\omega^2 = \frac{\epsilon l(l+1)\bar{N}^2(1+2\epsilon)^{-1-l}}{2(2l+1)(1+\epsilon)} \left((1+2\epsilon)^l(2+3\epsilon) \pm \sqrt{4(1+\epsilon)^{2l+2} + \epsilon^2(1+2\epsilon)^{2l}}\right). \tag{2.42}$$

This describes the frequencies of two (pairs of oppositely-signed) free modes. We can further analyse the two solutions by expanding in the small parameter ϵ. The first solution is

$$\omega^2 = \frac{1}{2}l(l+1)\bar{N}^2\epsilon^2 + O(\epsilon^3), \tag{2.43}$$

and therefore $\omega^2 \propto l^2$ for large l. This is similar to the behaviour of an internal gravity wave (see Section 1.5). The second solution is

$$\omega^2 = \frac{2l(l+1)\bar{N}^2\epsilon}{2l+1} + O(\epsilon^2), \tag{2.44}$$

so that $\omega^2 \propto l$ for large l. This can be compared with the properties of an interfacial gravity wave. Figure 2.3 shows the dependence of the mode frequencies on l and d (red line).

To justify our assertions, we consider the dispersion relation of internal

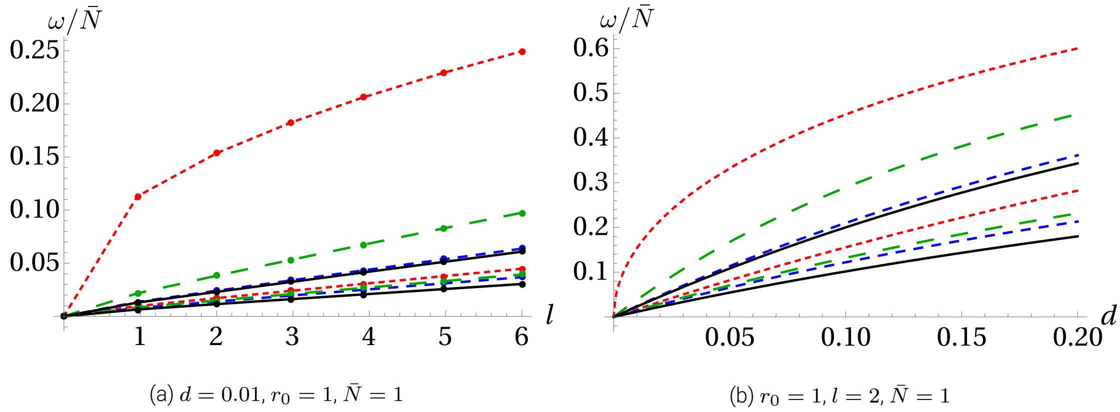

(a) $d = 0.01, r_0 = 1, \bar{N} = 1$

(b) $r_0 = 1, l = 2, \bar{N} = 1$

Figure 2.3: Dependence of the mode frequency ω for each mode on the parameters of the staircase and the boundary conditions on the end regions, shown for the single step, $m = 1$, case. The red (thin-dashed) lines show a finite staircase embedded in a convective medium, blue (dashed) lines show a finite staircase with solid wall boundary conditions. The green (thick-dashed) lines show a finite staircase with a solid wall beneath and a convective medium above. Finally, the black (solid) line shows the solution with a constant stratification between two solid walls. Panel a shows dependence of ω for each mode on the angular wavenumber l and Panel b shows dependence on step size d.

gravity waves in spherical geometry to be described by the following (Christensen-Dalsgaard, 2014):

$$\omega^2 \approx \bar{N}^2 \frac{k_\perp^2 d^2}{k_r^2 d^2 + k_\perp^2 d^2} \approx \frac{l(l+1)}{k_r^2 d^2} \bar{N}^2 \epsilon^2, \tag{2.45}$$

in the “plane-wave limit" in which $k_r \gg k_\perp$, and we identify $k_\perp^2 = l(l+1)/r_0^2$. Still within this limit, we again consider large l, we find $\omega^2 \propto l^2$, just like in equation 2.43. By comparing equation 2.45 to equation 2.43, we observe that these are equivalent if $k_r^2 \approx \frac{2}{d^2}$. Indeed, we have confirmed numerically that the free modes in the single step case are well described by equation 2.45 if $k_r \approx 145$, which is just slightly higher than $\sqrt{2}/d \approx 141$. The corresponding wavelength $\lambda_r = \frac{2\pi}{k_r} > d$, as we would expect for a mode with the character of an internal gravity wave.

Single interface (m=0)

The dispersion relation describing an interfacial gravity mode can be found by considering the case of a single interface ($m = 0$) to be

$$\omega^2 = \frac{l(l+1)\bar{N}^2\epsilon}{(2l+1)} = \frac{l(l+1)}{(2l+1)} \frac{g\Delta\rho}{r_0\rho_0}. \tag{2.46}$$

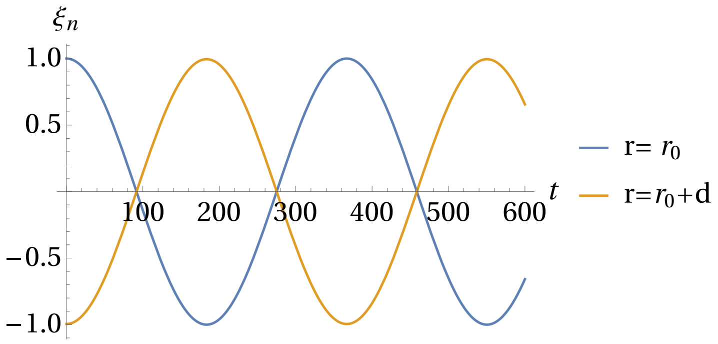

(a) $m = 1, l = 2, r_0 = 1, \bar{N} = 1, d = 0.01$

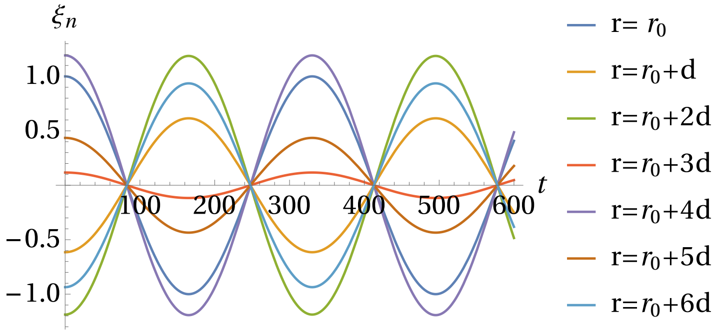

(b) $m = 6, l = 2, r_0 = 1, \bar{N} = 1, d = 0.01$

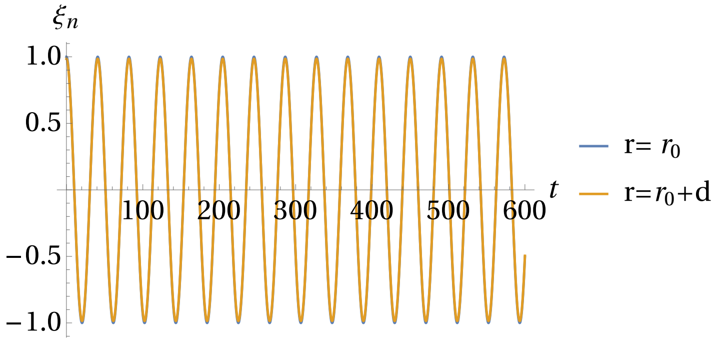

(c) $m = 1, l = 2, r_0 = 1, \bar{N} = 1, d = 0.01$

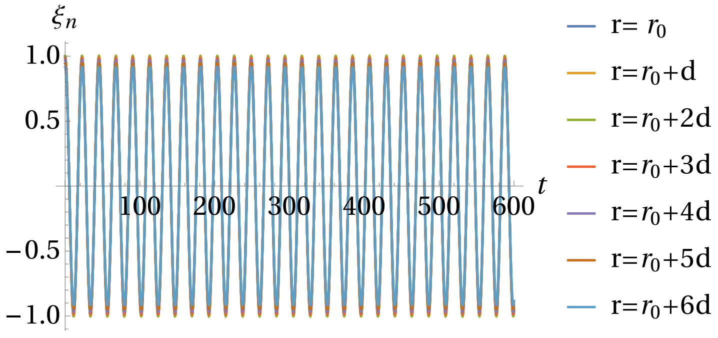

(d) $m = 6, l = 2, r_0 = 1, \bar{N} = 1, d = 0.01$

Figure 2.4: Radial displacement at each interface for the case of a staircase embedded within a convective medium. Panels a and c show the one step $(m = 1)$ case where a shows the internal wave-like solution with the two interfaces oscillating out of phase, and c shows the interfacial wave solution with both interfaces in phase. Panels b and d similarly show the interfaces for the six step $(m = 6)$ case.

For large l, we find $\omega^2 \propto l$, which behaves similarly to equation 2.44. This appears to differ from equation 2.44 by a factor of 2, but this only arises because it is the total density jump (across both steps) that is relevant, and this is twice as large in the single step case.

We show the radial displacement as a function of time at both interfaces in Figures 2.4a and 2.4c for both types of solution. Note that the overall amplitude is arbitrary but the relative amplitudes are meaningful. Figure 2.4a shows the solution corresponding to equation 2.43, in which both interfaces oscillate out of phase with each other, as we would expect if they are located either side of a node in a corresponding internal gravity mode. Figure 2.4c shows the solution corresponding to equation 2.44. This solution clearly has interfacial wave character because both interfaces oscillate in phase with one other, behaving as an “extended interface".

Multiple steps ($m > 1$)

We can also explore the free modes of an m-step staircase in a similar way when $m > 1$, except that we now obtain a polynomial of degree $(m + 1)$. The solutions are too complicated to gain any insight from writing them down, but we can use a computer algebra package (e.g. Mathematica) to analyse their properties. The solutions for multiple steps exhibit similar behaviour to the case of a single step. We again find that the highest frequency mode is an interfacial gravity-like mode, in which all of the interfaces oscillate in phase, so that the whole staircase behaves like a single extended interface. The other modes behave more like internal gravity modes, in which the interfaces do not all oscillate in phase, and the number of interfaces that are in phase can be related to the number of nodes in the corresponding gravity mode.

For the case with $m = 6$ steps, we show the radial displacement at each interface (again, with an arbitrary overall amplitude) in Figure 2.4d for the one interfacial mode in which all interfaces oscillate in phase, and one example (chosen from 6) of an internal gravity-like mode in Figure 2.4b. In the latter, the interfaces do

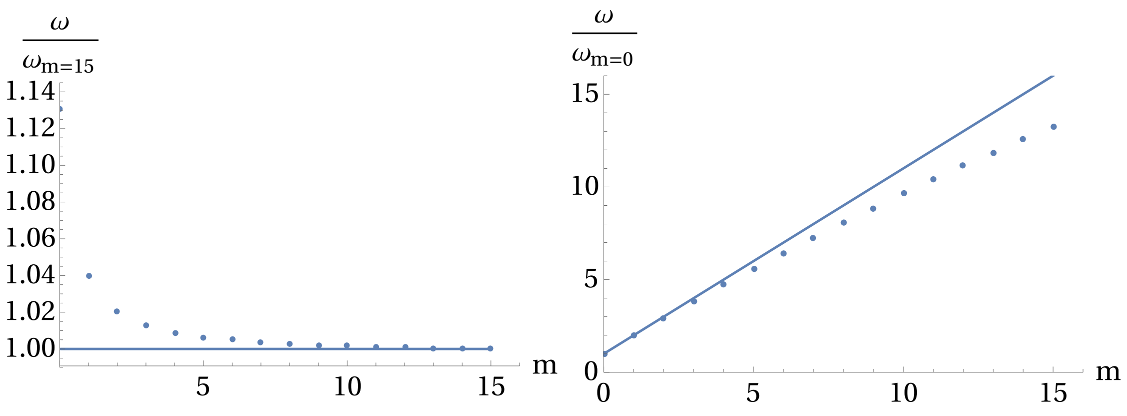

(a) $x = (m+1)\epsilon = 0.1$

(b) $\epsilon = 0.01$

Figure 2.5: Dependence of the frequency of the interfacial mode for each step number m, for $l = 2$, $\bar{N} = 1$. Panel a interfacial-like mode for a fixed staircase size $x = (m+1)\epsilon = 0.1$, such that the step size ϵ and density jump $\Delta\rho$ decrease as the step number increases. Solid line showing $y = 1$. Panel b interfacial-like mode for a fixed step size $\epsilon = 0.01$, such that the total length of the staircase and total density jump increase as the step number increases. Solid line showing $y = m+1$.

not all oscillate in phase, indicating that this is like an internal gravity mode (with a continuous uniform stratification) with 3 nodes. For multiple steps, the dependence on l, d and r_0 is qualitatively similar to that of a single step. Series expansions to explore the dependence of the frequencies of the waves on the parameters were not carried out in this case because the behaviour can be obtained qualitatively.

There are two ways to explore how the dispersion relation depends on the number of steps. If we fix the mean stratification, the total density jump and total length of the staircase, x, but we increase the number of steps, then ϵ and $\Delta\rho$ will decrease as steps are added such that $\Delta\rho = \frac{1}{(m+1)}\Delta\rho_{\text{total}}$ and $\epsilon = \frac{1}{(m+1)}x$. Figure 2.5a shows the interfacial wave solutions dependence on m for the case of a staircase with fixed size and total density jump. All solutions have been normalised by the $m = 15$ solution and tend to 1 as m is increased. This suggests that the total density jump $\Delta\rho_{\text{total}}$ is an important quantity for the dispersion relation.

If the step size and mean stratification are maintained, this will lead to a longer staircase and increased total density jump; the frequency therefore increases. Figure 2.5b shows the solution for ω for different numbers of steps, which corresponds to the interfacial wave solution, normalised by the $m = 0$ solution. We would expect to see a roughly linear dependence on m. We can see the trend falls away from the $y = m + 1$ line for large m. As the total staircase gets larger we would expect the approximation to one thin interface to be less accurate and therefore expect the solution to depart from this prediction.

2.4.2 Finite staircase with solid walls

We now consider the case of a finite staircase confined between solid walls at both ends, which might be relevant for the case of a stably-stratified terrestrial planetary core, for example. In particular, we consider solid walls at r_0 and $r_0 + (m + 2)d$, on which we enforce $\xi_r = 0$. The first interface is at $r_0 + d$, and the buoyancy frequency is defined as,

$$N^2 = \sum_{n=1}^{m+1} \bar{N}^2 \epsilon \delta(1 + n\epsilon - r). \tag{2.47}$$

The interface conditions remain unchanged and, as before, we construct a transfer matrix to relate our coefficients in the first and last layer,

$$\begin{bmatrix} A_{m+1} \\ B_{m+1} \end{bmatrix} = X' \begin{bmatrix} A_0 \\ B_0 \end{bmatrix}, \tag{2.48}$$

where

$$X' = T_{m+1} T_m \dots T_1. \tag{2.49}$$

Instead of considering decaying solutions we now consider solid wall boundary conditions such that the radial displacement at either end of the staircase is zero, i.e.

$$\xi_0(r = 1) = \xi_{m+1}(r = 1 + (m + 2)\epsilon) = 0. \tag{2.50}$$

These combine to give four simultaneous equations,

$$A_0 + B_0 = 0, \tag{2.51}$$

$$A_{m+1}(1 + (m + 2)\epsilon)^{l-1} + B_{m+1}(1 + (m + 2)\epsilon)^{-l-2} = 0, \tag{2.52}$$

$$A_{m+1} = A_0 X'_{1,1} + B_0 X'_{1,2}, \tag{2.53}$$

$$B_{m+1} = A_0 X'_{2,1} + B_0 X'_{2,2}. \tag{2.54}$$

We seek non-trivial solutions, which requires

$$X'_{1,2} + (1 + (m+2)\epsilon)^{-2l-1} X'_{2,2} = (X'_{1,1} + (1 + (m+2)\epsilon)^{-2l-1} X'_{2,1}). \tag{2.55}$$

This allows us to determine the dispersion relation describing the free modes of the staircase. We again obtain a polynomial of degree $(m+1)$, and so we obtain $(m+1)$ (pairs of) free modes.

The solution can be found for the single step $(m = 1)$ case, and we also expand each solution assuming $\epsilon \ll 1$ to obtain,

$$\omega^2 = l(l+1)\bar{N}^2\epsilon^2 + O(\epsilon^3), \tag{2.56}$$

and

$$\omega^2 = \frac{1}{3}l(l+1)\bar{N}^2\epsilon^2 + O(\epsilon^3). \tag{2.57}$$

As for the cases with decay boundary conditions in Section 2.4.1, we observe that there are modes for which $\omega^2 \propto l^2$ for large l, which is the expected behaviour for an internal gravity wave. However, the highest frequency mode no longer corresponds with an interfacial wave, and in fact none of the waves have the dependence $\omega^2 \propto l$ for large l expected of such waves. This is due to the boundary conditions that we have adopted. The highest frequency mode still has all of its interfaces oscillating in phase, but it no longer behaves as an interfacial wave. Instead, it behaves more like a gravity mode with no internal nodes. We show the roots of the dispersion relation in Figure 2.3 (blue dashed line).

2.4.3 Finite staircase with mixed boundary conditions

Finally, we consider the case where the staircase has a solid wall at the lower boundary and lies below a convective region. This case might be a better representation of a stratified layer at the edge of a solid inner core, which connects onto a convective envelope at its outer radius. The method used is a combination of the previous two methods, with a solid wall at r_0 and modes that decay above the staircase. The buoyancy profile N^2 and matrix X' are unchanged from Section 2.4.2.

Considering zero radial displacement at the bottom of the staircase to give,

$$\xi_0(r_0 = 1) = 0, \tag{2.58}$$

and forcing purely decaying solutions at the top of the staircase requires,

$$A_{m+1} = 0. \tag{2.59}$$

These combine to give three simultaneous equations,

$$A_0 + B_0 = 0, \tag{2.60}$$

$$A_0 X'_{1,1} + B_0 X'_{1,2} = 0, \tag{2.61}$$

$$B_{m+1} = A_0 X'_{2,1} + B_0 X'_{2,2}. \tag{2.62}$$

Non-trivial solutions require

$$X'_{1,2} = X'_{1,1}. \tag{2.63}$$

Similarly to the previous cases this allows us to determine the dispersion relation describing the free modes of the staircase. We again obtain a polynomial of degree $(m + 1)$, and so we obtain $(m + 1)$ (pairs of) free modes.

Expanding each solution in the single step case, assuming $\epsilon \ll 1$, we obtain the two solutions,

$$\omega^2 = \frac{1}{2}(3 + \sqrt{5})l(l + 1)\bar{N}^2\epsilon^2 + O(\epsilon^3), \tag{2.64}$$

and

$$\omega^2 = \frac{1}{2}(3 - \sqrt{5})l(l + 1)\bar{N}^2\epsilon^2 + O(\epsilon^3). \tag{2.65}$$

As in the case of solid wall boundary conditions in Section 2.4.2 we observe only modes where $\omega^2 \propto l^2$ for large l, corresponding to internal gravity wave behaviour.

The highest frequency modes with all interfaces oscillating in phase also act as an internal mode with no nodes instead of an interfacial mode. The roots of these two solutions are shown in Figure 2.3 (green thick-dashed line), which shows that they lie between the two previous cases.

2.4.4 Comparison with a uniform, continuously-stratified medium

We aim to further understand how density staircases behave differently from a uniform and continuously-stratified medium. Therefore we now turn to comparing the frequencies of the free modes of a staircase with those of a continuously-stratified medium with the same mean (constant) buoyancy frequency. We choose to compare the case with solid wall boundary conditions at either end (i.e. $\xi_r(1) = \xi_r(1 + (m + 2)\epsilon) = 0$), which we have already computed for a staircase in Section 2.4.2. We apply these boundary conditions to the solution given by equations 2.27 and 2.28 to obtain an infinite set of modes in the continuous case. We index these by a positive integer n which refers to the number of radial nodes in the solution. The resulting frequencies are

$$\omega = \pm\sqrt{\frac{4l(l+1)\bar{N}^2(\log(1+(m+2)\epsilon))^2}{(2l+1)^2(\log(1+(m+2)\epsilon))^2 + 4\pi^2 n^2}}. \tag{2.66}$$

For these calculations we fix the total size of the region and the total density jump across the staircase, and vary the number of steps m.

To compare the infinite set of free modes found in the stratified case to the free modes of the staircase, we take the first $m+1$ modes of the uniformly-stratified layer and compare these to the free modes of the staircase. Figure 2.6a shows the wave frequencies for all modes as a function of the number of steps m. It is clear that as m increases, the difference between the uniformly-stratified case and the staircase decreases.

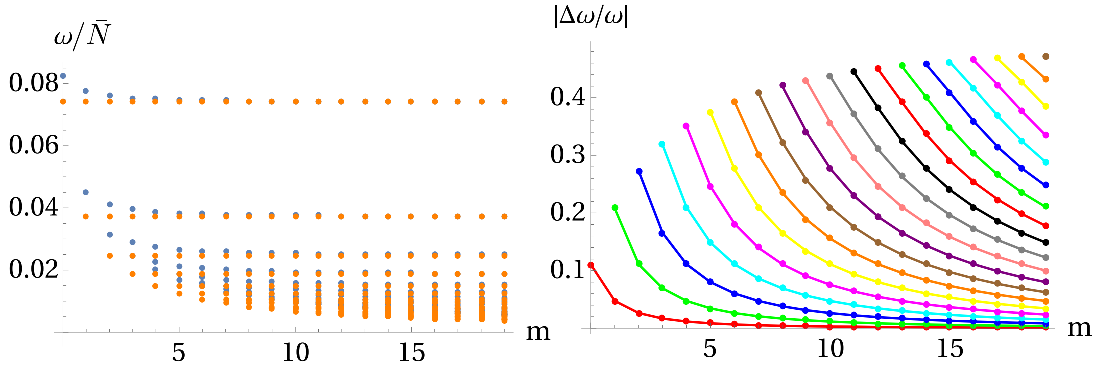

(a) Frequencies vs m for a uniformly-stratified layer (orange) and a staircase (blue).

(b) Fractional frequency difference (equation 2.67) between the modes of a uniformly-stratified layer and a staircase vs m.

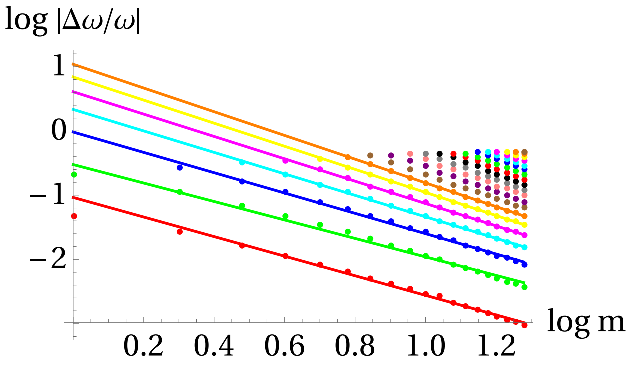

(c) Same as Panel b but on a log-log (base 10) plot.

Figure 2.6: Comparison of the frequencies of the free modes of a uniformly-stratified layer with a density staircase with the same mean stratification $\bar{N}$. This shows that the frequencies of the modes of a staircase approach those of a uniformly-stratified layer (behaving like m^{-2}) as the number of steps is increased, but that there is a consistently positive frequency shift.

To more clearly and quantitatively analyse the differences in frequency between a staircase and a uniformly-stratified medium, we define the fractional difference as

$$\frac{\Delta\omega}{\omega} = \frac{\omega_c - \omega_s}{\omega_c}, \tag{2.67}$$

where ω_s is the frequency of the staircase mode and ω_c is the frequency of the constant stratification mode. The magnitude of this quantity is plotted in Figure 2.6b, and is re-plotted using a log-log scale (base 10) in Figure 2.6c to determine its scaling behaviour. We find the mode frequencies in the case of a uniformly-stratified layer are always smaller than those in the staircase. Similar results are also expected with mixed boundary conditions, which might be considered the most astrophysically relevant case (e.g. Section 2.4.3).

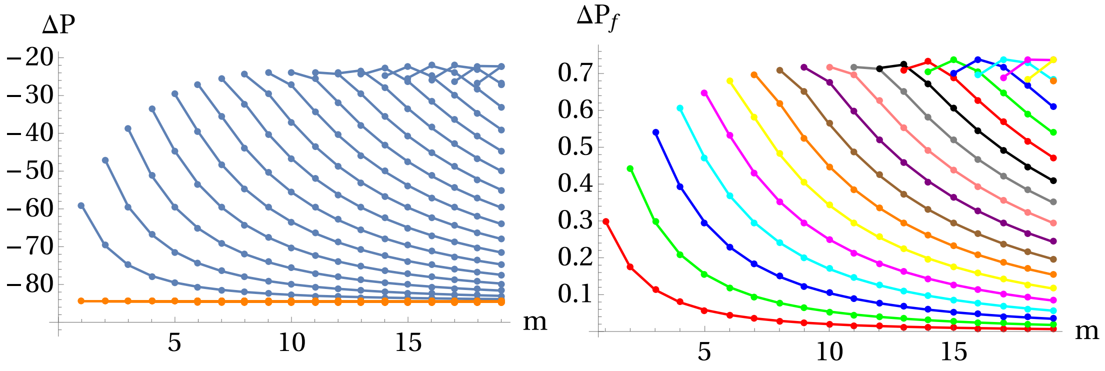

(a) Period spacing (equation 2.68) vs m for a uniformly-stratified layer (orange) and a staircase (blue).

(b) Fractional period difference (equation 2.70) between the modes of a uniformly-stratified layer and a staircase vs m.

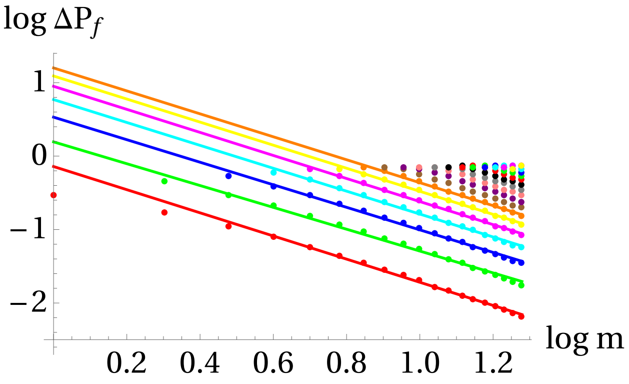

(c) Same as Panel b but on a log-log (base 10) plot.

Figure 2.7: Comparison of the period spacing of the adjacent free modes for a uniformly-stratified layer with a density staircase with the same $\bar{N}$.

Figure 2.6 shows that as the number of steps is increased, the fractional difference decreases, indicating that the free modes of a staircase converge to those of a uniformly-stratified medium with the same mean buoyancy frequency. This agrees with the results in Cartesian geometry found by Belyaev et al. (2015). As steps are added, the number of modes in the staircase increases. The fractional difference for each mode with a given number of radial nodes decreases as we increase the number of steps. However, the lowest frequency mode with the shortest corresponding radial wavelength (largest number of radial nodes) is always the most affected by the staircase and has the largest fractional frequency difference. This is expected as when the wavelength is sufficiently large compared to the step size it "sees the staircase" as a continuous medium with constant buoyancy frequency $\bar{N}$.

The dependence of the fractional frequency difference can be fitted with a power law for the purposes of extrapolation to a staircase with a large number of steps. We find

$$\frac{\Delta\omega}{\omega} \propto (m+1)^{-\alpha} \sim \epsilon^{\alpha}, \tag{2.68}$$

with a range in exponent $\alpha \approx 1.7 - 2.3$ found for the highest frequency modes. This is consistent with Belyaev et al. (2015), who found in their Cartesian model that $\alpha = 2$. This power law is useful as it allows us to extrapolate the frequency shifts to a large number of steps. This is important since the number of steps in a stably-stratified layer of a giant planet is uncertain (e.g. Leconte & Chabrier, 2012).

The staircase also alters the period spacing between two adjacent modes (Belyaev et al., 2015). This is interesting to analyse because the period spacing between adjacent internal gravity modes in a continuously-stratified medium is independent of the number of nodes (i.e the mode frequency) in the short-wavelength limit. However, the presence of a staircase may modify this relation and lead to potentially observable shifts in the period spacings. To analyse the period spacing between adjacent modes, we define

$$\Delta P_x = 2\pi\left(\frac{1}{\omega_{x,n}} - \frac{1}{\omega_{x,n+1}}\right). \tag{2.69}$$

Therefore, the dependence on a staircase can be analysed by considering the fractional difference,

$$\Delta P_f = \frac{\Delta P_c - \Delta P_s}{\Delta P_c}, \tag{2.70}$$

where again the subscript s refers to a staircase mode, and a subscript c refers to a continuous stratification mode. Figure 2.7a shows that the staircase decreases the period spacing between adjacent modes (blue symbols and lines), and the constant stratification result is independent of node number (orange). As found in the analysis of the frequency shifts above, the fractional difference between a stably-stratified medium and a staircase structure decreases as the number of steps increases, and is largest for the lowest frequency modes with the shortest wavelengths in each case. The fitted dependence is also found, for the purpose of extrapolation,

$$\Delta P_f \propto (m+1)^{-\beta} \sim \epsilon^{\beta}, \tag{2.71}$$

where $\beta \approx 1.8 - 2$ for the highest frequency modes. This is also consistent with Belyaev et al. (2015), who found the staircase decreases the spacing with a squared dependence in ϵ.

2.5 Conclusion

We have built on previous work that analysed the free modes of a density staircase (Belyaev et al., 2015; André et al., 2017). We extended these works by adopting a simplified global (spherical) Boussinesq model. As a first step to tackling this problem in a global model, we have omitted planetary rotation. Our model allows us to analyse the behaviour of waves with wavelengths comparable with the radius of the stratified layer, which may be important for the inner regions of these planets, and those with small harmonic degrees that may be the easiest to observe. Global effects may also be important for the modes of an extended staircase region and are likely to be required to study tidal forcing self-consistently, which we turn to in Chapters 4 to 6.

In this chapter we have presented idealised calculations to study the properties of waves in stably-stratified planetary layers containing a layered density structure. We have analysed the properties of the free modes and our main result is that wave propagation is strongly affected by the presence of a density staircase. This extends and confirms prior work in Cartesian geometry (Belyaev et al., 2015; André et al., 2017).

By determining the free modes in a region containing a density staircase we found they consist of both internal and interfacial gravity waves, with the presence of the latter depending on the properties of the surrounding fluid. Solid wall boundary conditions do not exhibit modes with interfacial-like behaviour, whereas a staircase embedded in a convective medium (decaying boundary conditions) has a clear interfacial wave solution.

We have compared the free modes in a density staircase with those of a continuously-stratified layer. In the limit of infinitely many steps, the frequencies of the free modes converge towards those of a continuously-stratified medium. However, for a finite number of steps, the modes of a staircase typically have larger frequencies than those of a continuously-stratified medium. We have quantified this frequency shift due to the presence of a staircase as a function of its properties, as well as the shift in the period spacing between adjacent modes. In both cases we find they scale as $(m+1)^{-2}$, where m is the number of steps in the staircase. This is consistent with the Cartesian results of Belyaev et al. (2015). For the largest wavelength modes with low harmonic degrees, the shift is found to be very small if there are as many as 10^6 steps, so this may be difficult to detect observationally. But if such a signal is detected by analysing the properties of the mixed f-g modes that are resonant with density waves in the rings (e.g. Marley & Porco, 1993; Fuller, 2014; Hedman & Nicholson, 2013; Hedman et al., 2018), for example, then this could constrain the properties of any stable layer that is present in the planetary interior. We note that semi-convection in massive stars ($M_* \gtrsim 15M_\odot$) could also produce stable layers that could in principle be constrained in a similar way using asteroseismology (Schwarzschild & Härm, 1958; Sakashita & Hayashi, 1959).

Chapter 3

Transmission through a density staircase in spherical geometry

Now we have explored the properties of the free modes we turn our attention to exploring the transmission of internal waves through density staircases. We continue to adopt spherical geometry, which extends prior work in Cartesian geometry (Sutherland, 2016; André et al., 2017).

Planetary models suggest that it is possible that only parts of a stratified layer have a layered density structure. Therefore, an internal gravity wave (that may be excited by tidal forcing or by interaction with neighbouring convection zones) can propagate in the continuously stratified region adjacent to layers of semi-convection.

In this chapter, we consider a staircase embedded in a medium that supports internal waves. This allows us to analyse how the density staircase affects the transmission of these waves. This will further the understanding of how these waves travel through the interior of the planet, particularly where they can propagate, and where they may dissipate.

3.1 Model

We now consider a staircase-like structure embedded within a stably-stratified layer which permits the propagation of internal gravity waves. To do so, we must alter the density profile used in Section 2.1 to have non-zero buoyancy frequency in each end region. We now define the buoyancy frequency as,

$$N^2 = \begin{cases} N_a^2 & \frac{r_c}{r_0} \ll r < 1, \\ \displaystyle\sum_{n=0}^{m} \bar{N}^2 \epsilon \delta(1 + n\epsilon - r) & 1 < r < 1 + m\epsilon, \\ N_b^2 & r > 1 + m\epsilon, \end{cases} \tag{3.1}$$

where N_a^2 and N_b^2 are assumed to be positive constants. We continue to consider a perfectly absorbing core to exist at a small radius $r_c \ll r_0$, which removes the requirement to impose a regularity condition at $r = 0$. If we were to include $r = 0$, then we would simply be modelling the transmission of a wave from a radius r_0, to the centre, and back again. Since we neglect dissipative processes in this first instance, this would not be an informative calculation.

By combining equations 2.13 and 3.1 and solving as before, the entire solution for the radial displacement is

$$\xi_n = \begin{cases} A_0 r^{\lambda_{a+}} + B_0 r^{\lambda_{a-}} & \frac{r_c}{r_0} \ll r < 1, \\ A_n r^{l-1} + B_n r^{-l-2} & r_{n-1} < r < r_n, \\ A_{m+1} r^{\lambda_{b+}} + B_{m+1} r^{\lambda_{b-}} & r > 1 + m\epsilon, \end{cases} \tag{3.2}$$

where $r_n = 1 + n\epsilon$, $n = 1, \dots, m$, and

$$\lambda_{a/b_\pm} = -\frac{3}{2} \pm \frac{1}{2}\sqrt{1 + 4\left(1 - \frac{N_{a/b}^2}{\omega^2}\right) l(l+1)}. \tag{3.3}$$

For the wave to propagate in the end regions, we require complex solutions where $\mathrm{Im}[\lambda_{a/b_\pm}] \neq 0$. Therefore, from equation 3.3, the following condition must be satisfied for waves to exist in an end region:

$$\frac{\omega^2}{N_x^2} < \frac{4l(l+1)}{4l(l+1)+1}, \tag{3.4}$$

where N_x takes the appropriate value for the region considered. This restricts the allowable values of $k_\perp$ and ω that permit wave-like solutions in the end regions. We will later mark these limits on our plots showing the transmission of waves.

3.1.1 Transmission coefficient

We would like to analyse how efficiently an incident internal gravity wave is transmitted (and how much is reflected) when it propagates through a staircase. To do so, we define the transmission coefficient to be the ratio of the radial energy flux of the incident wave (F_{in}) with that of the outgoing wave (F_{tr}),

$$T = \frac{F_{\mathrm{tr}}}{F_{\mathrm{in}}}. \tag{3.5}$$

The energy flux is defined using the standard definition for a linear wave

$$F = \pi r^2 \int_0^\pi \mathrm{Re}[-i\omega\xi_r p^*] \sin\theta d\theta, \tag{3.6}$$

where ξ_r is the radial displacement and p^* is the complex conjugate of the pressure perturbation, containing the r and θ and ϕ. We are only concerned with the ratio of the energy flux at different radial locations, and therefore it is not necessary to evaluate the energy flux exactly. As a result, we drop unnecessary factors from this analysis, and hence find

$$F \propto \mathrm{Im}[\omega\tilde{\xi}_r\tilde{p}^*]r^2. \tag{3.7}$$

We then use equation 2.11 to eliminate $\tilde{p}^*$, so that

$$F \propto \mathrm{Im}\left[\omega^3\left(r^2\tilde{\xi}_r\frac{\mathrm{d}\tilde{\xi}_r^*}{\mathrm{d}r}+2r\tilde{\xi}_r\tilde{\xi}_r^*\right)\right]r^2, \tag{3.8}$$

and using equation 3.2 we find

$$F \propto \mathrm{Im}\left[r^2\lambda_\pm^*|A/B_n|^2 r^{2\,\mathrm{Re}[\lambda_\pm]-1}+2r|A/B_n|^2 r^{2\,\mathrm{Re}[\lambda_\pm]}\right]r^2. \tag{3.9}$$

Therefore, the flux in the downward and upward propagating waves is

$$F_{\mathrm{down}} \propto \mathrm{Im}[\lambda_+^*]|A_n|^2, \tag{3.10}$$

and

$$F_{\mathrm{up}} \propto \mathrm{Im}[\lambda_-^*]|B_n|^2, \tag{3.11}$$

which allow us define two different transmission coefficients depending on the direction of propagation of the incident wave. For a downward propagating wave,

$$T_{\mathrm{down}} = \frac{|A_0|^2}{|A_{m+1}|^2}\frac{\mathrm{Im}[\lambda_{a_+}^*]}{\mathrm{Im}[\lambda_{b_+}^*]}, \tag{3.12}$$

and for an upward propagating wave,

$$T_{\mathrm{up}} = \frac{|B_{m+1}|^2}{|B_0|^2}\frac{\mathrm{Im}[\lambda_{b_-}^*]}{\mathrm{Im}[\lambda_{a_-}^*]}. \tag{3.13}$$

These can be shown to be equivalent to the transmission coefficient obtained in the Cartesian case by André et al. (2017). From these formulations we can see that the transmission depends on both the amplitudes and vertical wavenumbers of the solution in the end regions. This difference in wavenumbers originates from the varying group velocity. The group velocity of an internal gravity wave depends on the stratification of a region and therefore if the stratification in the end regions is different (e.g. $N_a \neq N_b$) this factor contributes to the result.

We use the same interface conditions as in Section 2.1 (equations 2.34

and 2.34) and the matrix X is constructed as before.

We consider first a downwards propagating wave, originating above the staircase and travelling towards the centre of the planet. By considering the left hand panel of Figure 2.2, we have an incident wave with coefficient A_m, which is partially transmitted (and partially reflected) at each interface. Therefore, the solution within each layer is a combination of both an incident and reflected component, except the final layer where we have assumed no reflection from the core. As a result of this we define the upward component in that layer to be zero ($B_0 = 0$) to give,

$$\begin{bmatrix} A_{m+1} \\ B_{m+1} \end{bmatrix} = X \begin{bmatrix} A_0 \\ 0 \end{bmatrix}, \tag{3.14}$$

so that the transmission coefficient becomes

$$T_{\mathrm{down}} = \frac{1}{|X_{1,1}|^2} \frac{\mathrm{Im}[\lambda^*_{a+}]}{\mathrm{Im}[\lambda^*_{b+}]}. \tag{3.15}$$

For an upward propagating wave, starting near the centre of the planet and propagating outwards, there is similarly no reflected wave in the upper layer ($A_{m+1} = 0$), so that

$$\begin{bmatrix} 0 \\ B_{m+1} \end{bmatrix} = X \begin{bmatrix} A_0 \\ B_0 \end{bmatrix}, \tag{3.16}$$

giving a transmission coefficient,

$$T_{\mathrm{up}} = \frac{1}{|X^{-1}_{2,2}|^2} \frac{\mathrm{Im}[\lambda^*_{b-}]}{\mathrm{Im}[\lambda^*_{a-}]}. \tag{3.17}$$

Equations 3.15 and 3.17 allow us to determine the transmission of an incident down-going or up-going wave through a density staircase. The properties of the staircase enter through the entries of the X matrix, and that of the incident wave and the end regions enter through the wavenumber ratio. As a result of the spherical geometry, it is possible for T_{up} and T_{down} to differ for the same incident wave and staircase/end region properties, unlike in the Cartesian case. We expect the transmission to recover the Cartesian results when $\epsilon \ll 1$ (and $r_0 \gg (m+1)d$), at least for waves with $l \gg 1$. On the other hand, spherical effects are expected to become important when $\epsilon \sim 1$ (or $r_0 \sim (m+1)d$) or $l \sim \mathcal{O}(1)$.

3.2 Results for wave transmission

We present our results for the transmission coefficient as a function of incident wave frequency ω, and horizontal wavenumber $k_\perp = \sqrt{l(l+1)}/r$, where r will take the value of the location of the first interface for the incident wave, in a series of plots for various parameter values (varying m, ϵ, N_a and N_b). We have treated $k_\perp d$ as a continuous parameter to aid plotting and interpretation, although l strictly only takes integer values and therefore gives discrete values for $k_\perp d$. Unless specified otherwise, we show the downward transmission coefficient in these figures, according to equation 3.15, though we explore the difference between this and the upward propagation result in one case (Section 3.2.4).

In each figure, we also over-plot the frequencies of the free modes of the staircase computed from equation 2.41 using blue dashed lines, in the case where the staircase is sandwiched between two convective layers (decaying boundary conditions), following Section 2.4.1. The frequency cut-off for wave propagation in the end regions, according to equation 3.4 is shown by the solid coloured lines. The yellow and green lines show the criterion for solutions in the top and bottom layer to be propagative, respectively, while the red line shows the region in which the wave is propagative if this region was instead of a staircase a uniformly-stratified layer with the same mean stratification. For cases in which $N_a = N_b = \bar{N}$ only the red line is shown and for cases where $N_a = N_b \neq \bar{N}$ only the red and yellow lines are shown.

We begin by verifying our method by reproducing results from Cartesian geometry. To do so, we take the double limit $l \gg 1$, and $(m+1)\epsilon \ll 1$, where for the latter we simply choose $\epsilon \ll 1$. Figure 3.1 shows the transmission through a one

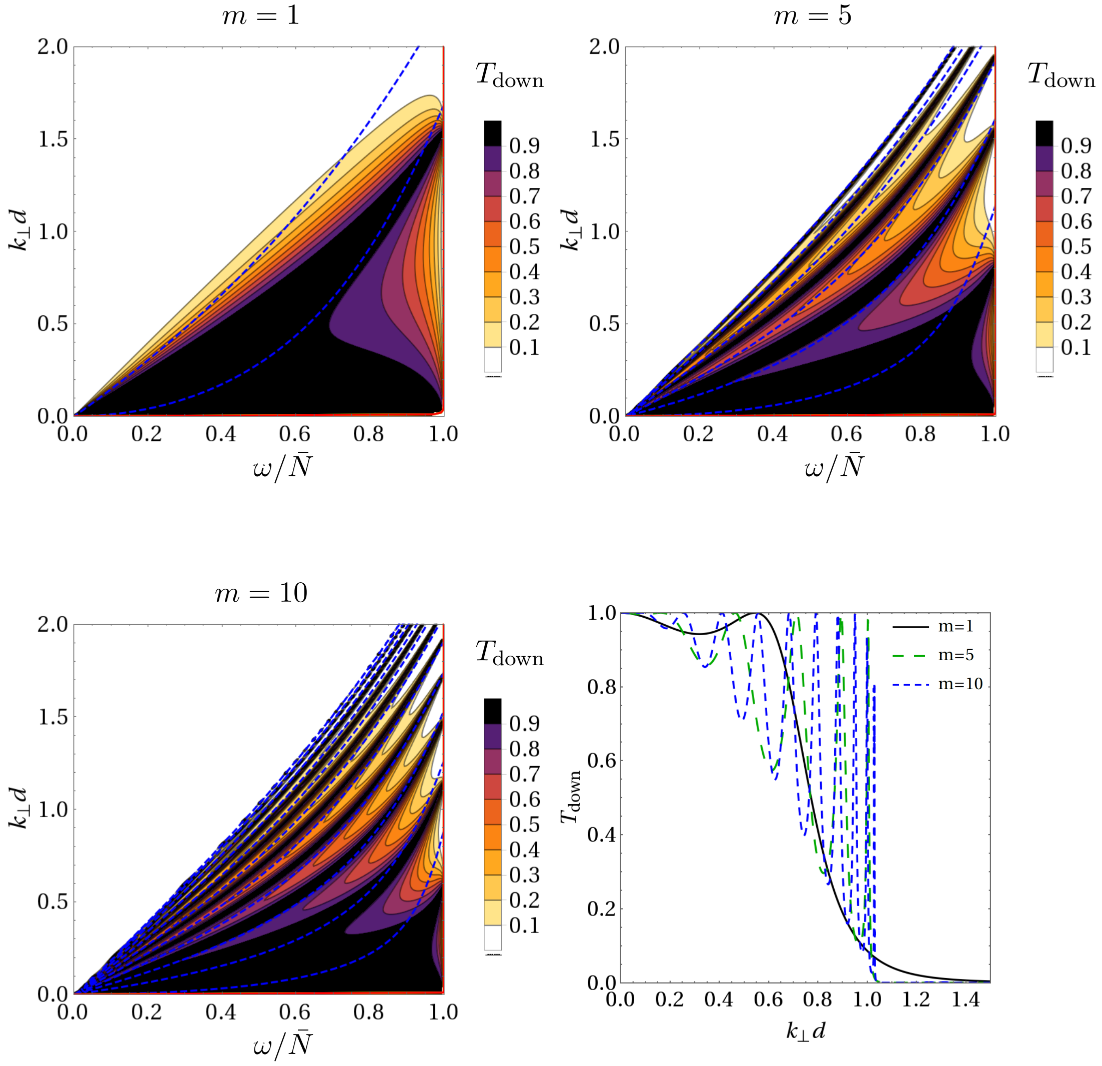

Figure 3.1: Transmission coefficient for a downward propagating wave T_{down} as a function of incident wave frequency $(\omega/\bar{N})$ and scaled horizontal wavenumber $k_\perp d = \sqrt{l(l+1)}\epsilon$, for a range of step numbers and a fixed small staircase size $(m+1)\epsilon$. Top left panel shows $(m+1)\epsilon = 0.01$, with $m = 1$, the top right and bottom left panels show the same case with $m = 5$ and $m = 10$, respectively. Each panel has $N_a = N_b = \bar{N} = 1$. Over-plotted are the free modes of the same staircase (blue dashed lines), the frequency limits for wave propagation in the end regions and for the staircase if this was instead uniformly-stratified (red, close to axis). The bottom right panel shows a 1D profile at $\omega = 0.5$, for $m = 1$ (black), $m = 5$ (green) and $m = 10$ (blue).

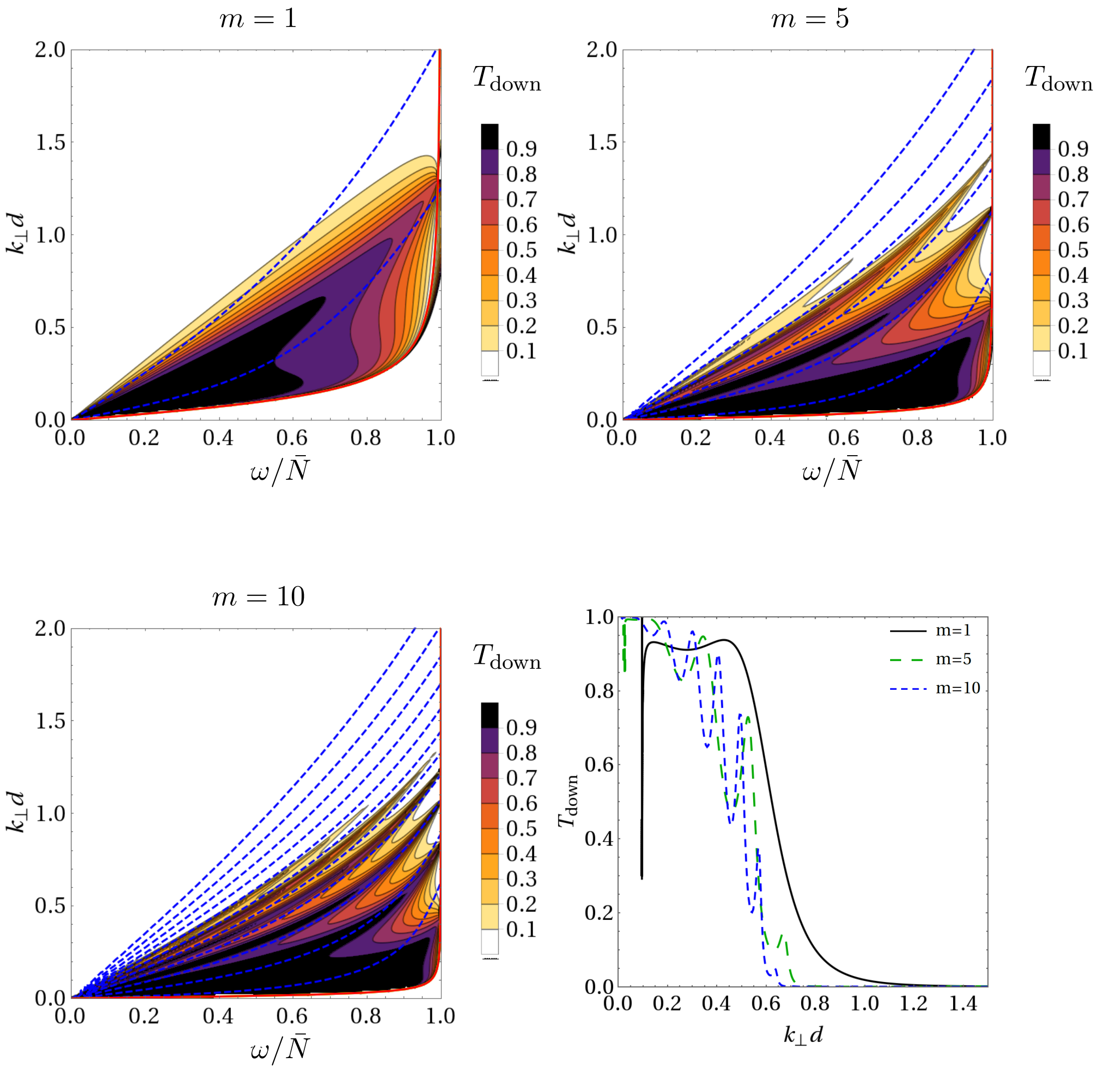

Figure 3.2: Same as Figure 3.1, except that the staircase is larger relative to the radius of the planet such that $(m+1)\epsilon = 1$.

$(m = 1)$, five $(m = 5)$, and ten $(m = 10)$ step staircase, assuming ϵ is small. These agree quantitatively with Figures 9a and 18b in André et al. (2017). We observe that long wavelength (low wavenumber) waves are near-perfectly transmitted. This limit is when the waves "sees" the staircase as a continuously-stratified medium, and is little affected by the discreteness of the steps. On the other hand, shorter wavelength waves, such that $k_\perp d \sim 1$ are only transmitted when they are resonant with a free mode of the staircase. As a result, we observe bands of enhanced transmission that align well with the free modes of the staircase as calculated in Chapter 2.

The number of peaks of enhanced transmission is always one smaller than the number of free modes of the staircase. The transmission peaks do not lie directly on top of the free modes of the staircase, with the agreement depending on the parameters adopted. This is presumably because the stratified end regions and the boundary conditions these dictate modify the wave frequencies, as was found in Chapter 2.

3.2.1 Dependence on ϵ (relative step size)

In spherical geometry, the transmission depends on the relative step size, ϵ, in addition to how this modifies $k_\perp$. This differs from the Cartesian case in André et al. (2017) where the two quantities always arise in equations as the product $k_\perp d$.

First, we explore the dependence on step size by fixing the total size of the staircase $x = (m + 1)\epsilon$ and increasing the number of steps, m, therefore decreasing ϵ.

Figure 3.1 and Figure 3.2 show the overall transmission for $x = 0.01$ and $x = 1$, respectively. In the case of a small staircase $(x = 0.01)$, ϵ remains small for all panels, leading to little change in the region of transmission. The only observable effects are the additional and narrower bands of enhanced transmission, reducing the overall transmission. In the case of the large staircase the variation in ϵ has a

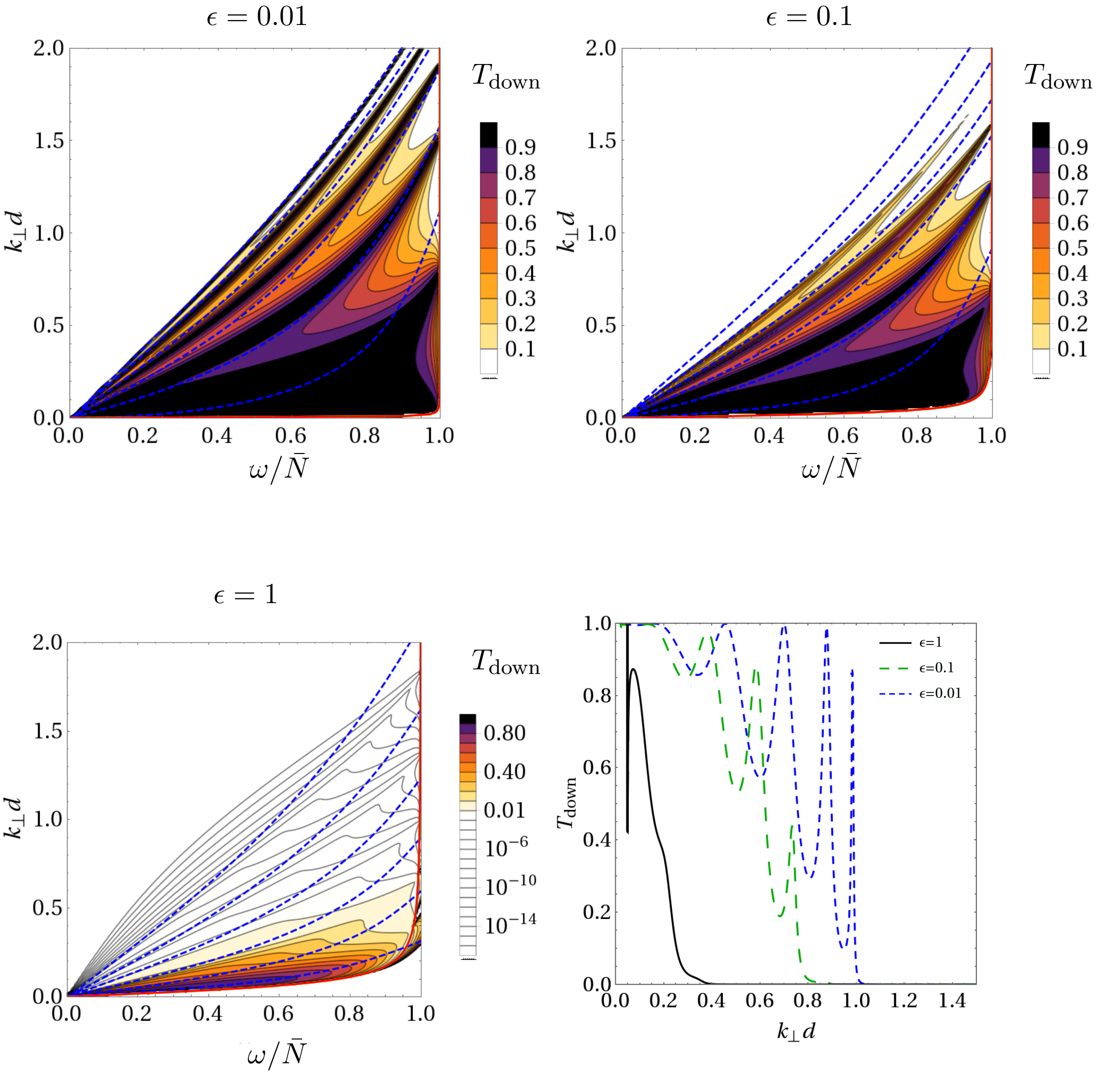

Figure 3.3: Transmission coefficient for a downward propagating wave T_{down} as a function of incident wave frequency $(\omega/\bar{N})$ and scaled horizontal wavenumber $k_\perp d = \sqrt{l(l+1)}\epsilon$, for a range of relative step sizes ϵ. Top left panel shows $m = 5$ steps, with $\epsilon = 0.01$, the top right and bottom left panels show the same case with $\epsilon = 0.1$ and $\epsilon = 1$, respectively. Each panel has $N_a = N_b = \bar{N} = 1$. Over-plotted are the free modes of the same staircase (blue dashed lines), the frequency limits for wave propagation in the end regions and for the staircase if this was instead uniformly-stratified (red). The bottom right panel shows a 1D profile at $\omega = 0.5$, for $\epsilon = 0.01$ (blue), $\epsilon = 0.1$ (green) and $\epsilon = 1$ (black).

greater effect as the size of the staircase is comparable to the staircase radius r_0. We can see the reduced size of the transmission region as ϵ increases, as well as the additional bands observed before. The frequency range in which a wave-like solution can exist (described by equation 3.4) also becomes smaller.

By analogy with equation 2.15, we expect that as ω decreases k_r will increase and due the dependence of both quantities on l, we note that for a given ω, as $k_\perp$ increases so will k_r. As we expect short radial wavelength waves to be more strongly affected by the staircase we predict to observe the largest effect on transmission at high $k_\perp$ and low ω values. This is shown in the bottom right panel of Figure 3.2 by observing that the peaks at the largest $k_\perp d$ for a given ω are affected the most strongly as ϵ is increased.

Additionally, we explore how the transmission depends on ϵ as the step number remains constant. Figure 3.3 shows transmission decreasing as ϵ is increased. As ϵ is increased the peaks of transmission at high $k_\perp$ values become sufficiently small that these are only visible with extra contours for smaller T values. This behaviour is due to the fact that, as ϵ is increased (for fixed m, $\Delta\rho$ and $\bar{N}$), the total size of the staircase increases, thus the total size of the evanescent layers increases, leading to reduced transmission. An additional effect of ϵ observed here is that as ϵ is increased, the transmission peaks shift from lying below to above the free mode predictions.

3.2.2 Non-uniform step size

In reality, we might expect the sizes and density jumps of the convective layers to vary. To explore this effect, we consider non-uniformly sized convective layers by building upon the Cartesian analysis (Sutherland, 2016; André et al., 2017). The

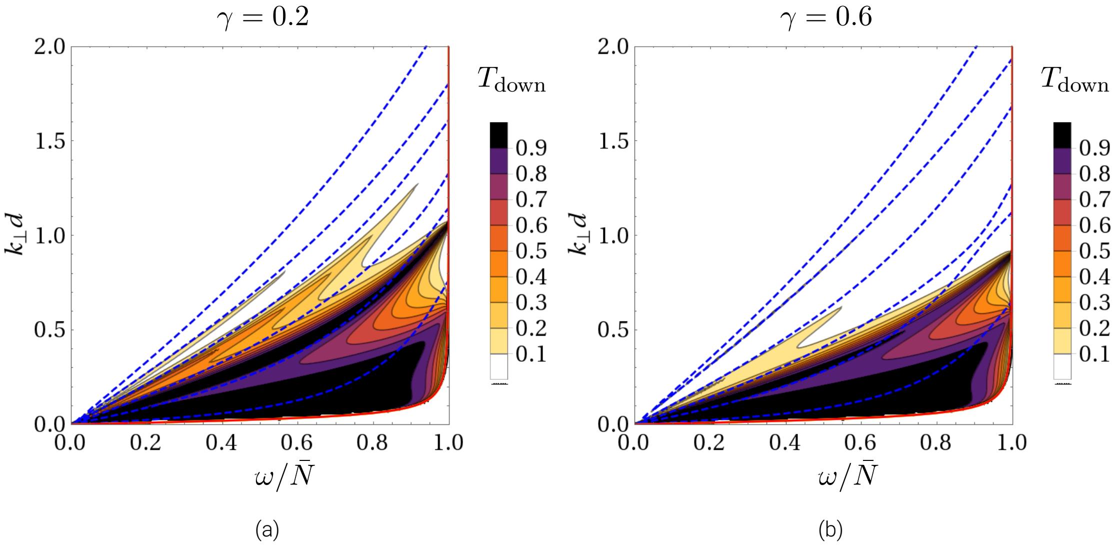

(a)

(b)

Figure 3.4: Transmission coefficient for a downward propagating wave T_{down} as a function of incident wave frequency $(\omega/\bar{N})$ and scaled horizontal wavenumber $k_\perp d = \sqrt{l(l+1)}\epsilon$, for non-uniform step size and $x = (m+1)\epsilon = 1$. Over-plotted are the free modes of the same staircase (blue dashed lines), the frequency limits for wave propagation in the end regions and for the staircase if this was instead uniformly-stratified (red). Panel a $\gamma = 0.2$ and Panel b $\gamma = 0.6$.

location of each interface is now taken to be

$$r_n = 1 + n\epsilon_n, \tag{3.18}$$

$$\epsilon_n = \epsilon\left(1 + \frac{\gamma}{n}\sigma_n\right), \tag{3.19}$$

where γ is a free parameter taken to be less than 1, and σ_n is a random number between -1 and 1 for $n = 1, \ldots, (m-1)$, and $\sigma_0 = 0$ and $\sigma_m = 0$.

Figure 3.4 shows the transmission for two cases with the same set of σ_n values with $\gamma = 0.2$ and $\gamma = 0.6$. We observe the location of the bands of enhanced transmission have shifted to align with the now irregular spacing of the free modes. Overall, the transmission of waves is reduced by the non-uniform step size and continues to decrease as γ is increased. The bands of enhanced transmission become narrower. We note that this remains true for a small shift in the interface locations ($\gamma = 0.2$), where the effect on the free modes is small whilst the effect on transmission remains significant.

3.2.3 Changing the properties of the end regions (N_a, N_b)

The stratification at the bottom and top of the staircase (N_a and N_b) can be varied independently of other staircase properties. Figure 3.5 shows that as the stratification is altered such that they differ from the mean stratification of the staircase, the bands of enhanced transmission become narrower with reduced transmission for adjacent non-resonant modes.

As we require wavelike solutions at both the bottom and top of the staircase, the range of frequencies transmitted are constrained by the smallest buoyancy frequency in these regions (N_a and N_b), as defined by equation 3.4. The wave is always evanescent inside the staircase, therefore the value of mean stratification $\bar{N}$ does not restrict the range of frequencies transmitted. An interesting consequence is that this allows the staircase to increase the range of transmitted waves to frequencies larger than that of the mean stratification, which would not be transmitted by a uniformly-stratified medium – see the bottom panel of Figure 3.5, for example.

3.2.4 Testing up/down symmetry

We always observe that the upward and downward transmission differs only by the definition of incident $k_\perp d$. This symmetry is expected in the Cartesian limit due to the up/down symmetry of the Boussinesq system (e.g. Sutherland, 2010). However, this symmetry no longer holds in spherical geometry. Figure 3.6 shows the upward and downward transmission, where in both cases $k_\perp d$ value is taken at the top of the staircase, $k_\perp = \frac{\sqrt{l(l+1)}}{1+m\epsilon}$. The transmission is identical in both cases when we scale the y-axis in this way. If we were instead to plot the same data as a function of the incident wavenumber, this would only re-scale the y-axis values in the right panel. This is consistent with the transmission peaks aligning with the free modes of the staircase, which do not depend on the direction of propagation of the incident wave.

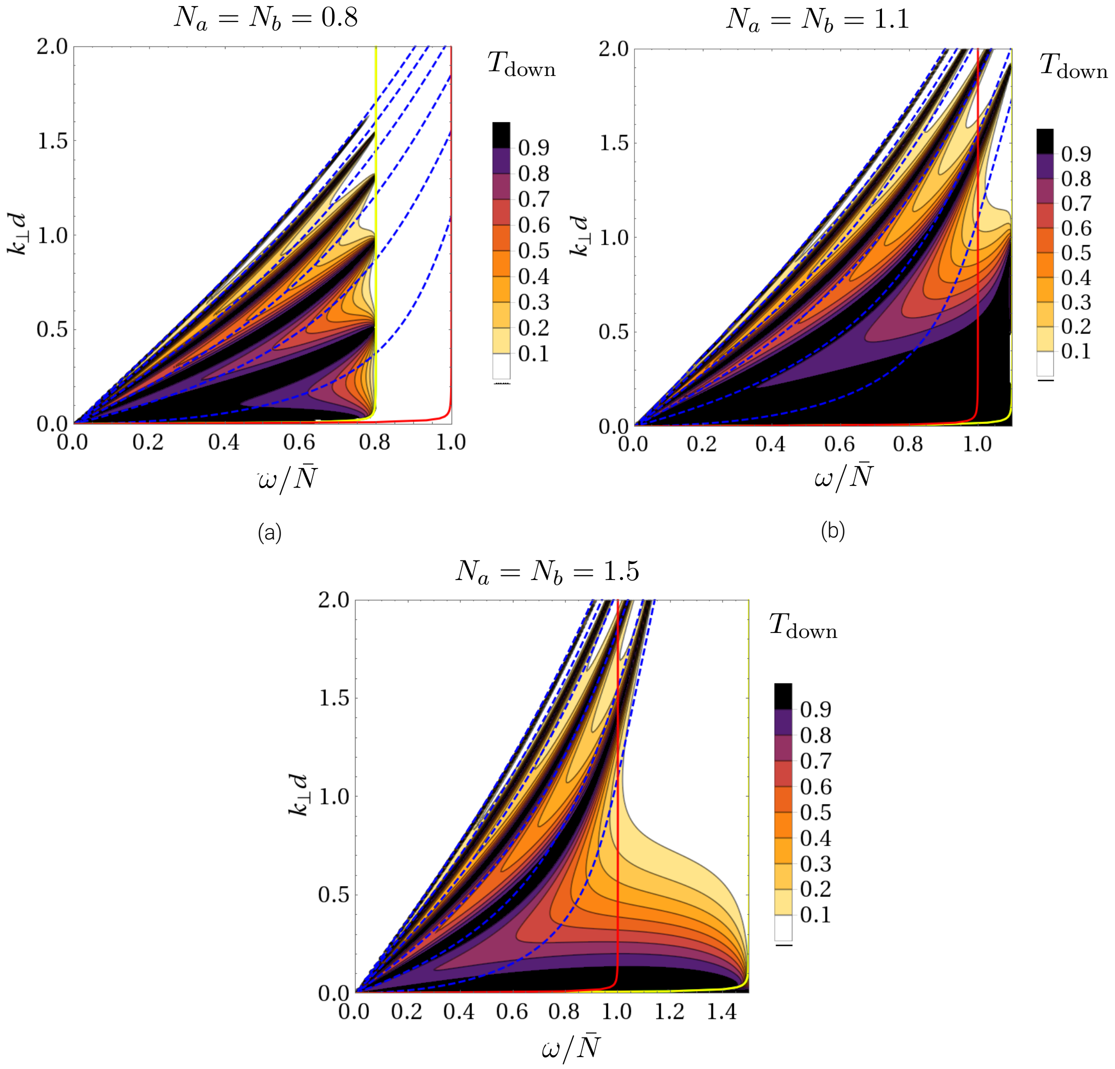

(a)

(b)

(c)

Figure 3.5: Transmission coefficient for a downward propagating wave T_{down} as a function of incident wave frequency ($\omega/\bar{N}$) and scaled horizontal wavenumber $k_\perp d = \sqrt{l(l+1)}\epsilon$, for a range of stratification values in the adjacent regions, N_a, N_b and a fixed step number, $m = 5$ and a fixed staircase size $(m+1)\epsilon$=0.1. Panels a, b, c show $N_a = N_b = 0.8, 1.1, 1.5$, respectively. Over-plotted are the free modes of the same staircase (blue dashed lines), the frequency limits for wave propagation in the end regions (yellow) and for the staircase if this was instead uniformly-stratified (red).

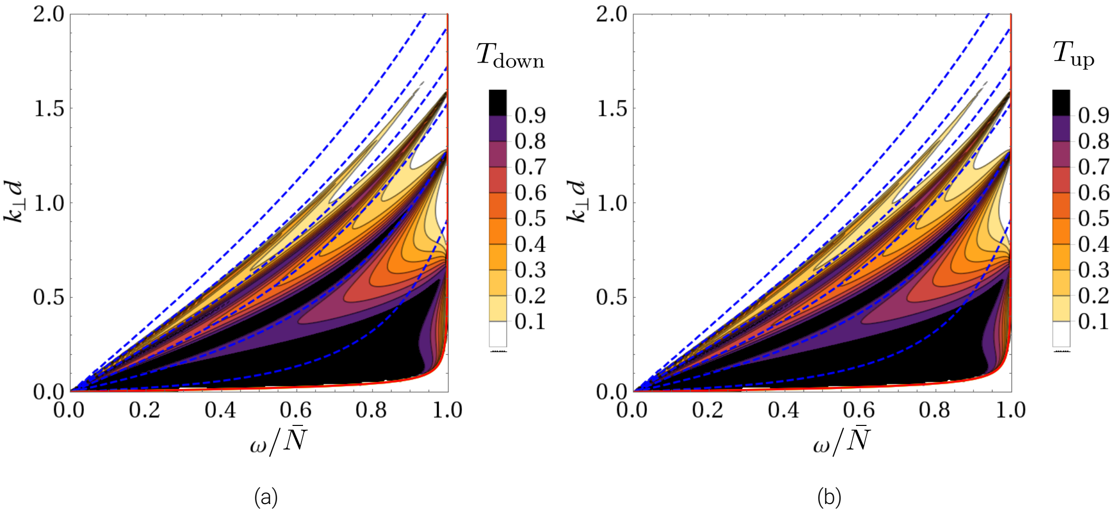

Figure 3.6: Comparison of the transmission coefficient for a downward (T_{down}, panel a) and upward (T_{up}, panel b) propagating incident wave as a function of the scaled wave frequency ($\omega/\bar{N}$) and horizontal wavenumber $k_\perp$ (specified in the text). Both panels have $m = 5$ steps, $\epsilon = 0.1$, and $N_a = N_b = \bar{N} = 1$. Over-plotted are the free modes of the same staircase (blue dashed lines) and the frequency limits for wave propagation in the end regions and for the staircase if this was instead uniformly-stratified (red). This shows the symmetry between upward and downward propagating waves, even when ϵ is no longer small.

In Cartesian geometry the transmission is also symmetric with respect to exchanging N_a and N_b, which ultimately results from the up/down symmetry of the Boussinesq system in that case. This can be observed when looking at transmission in the Cartesian limit (with $\epsilon = 0.01$) in Figure 3.7. On the other hand, when we increase ϵ, spherical effects become important and the symmetry between upward and downward propagating waves does not hold when N_a and N_b are swapped. This shows that the Boussinesq symmetry previously observed no longer holds in the global case. In all cases the effect of reducing the stratification on the transmission is seen in agreement with the discussion in Section 3.2.3.

3.2.5 Reflection coefficient

We note at this point that it is also possible to consider the reflection coefficient. This is defined to be the ratio of the radial energy flux of the incident wave (F_{in}) with that of the reflected wave (F_{re}),

$$R = \frac{F_{re}}{F_{in}}. \tag{3.20}$$

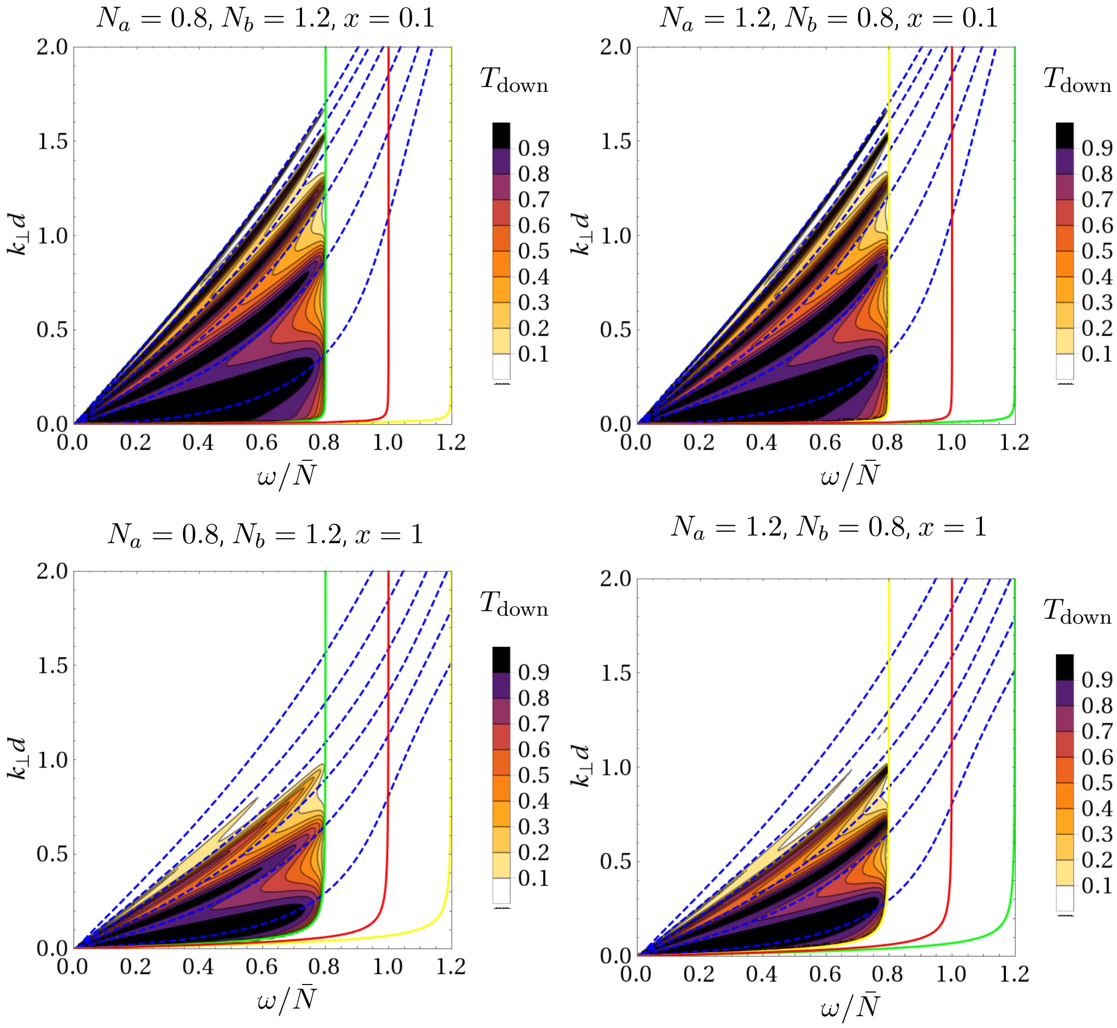

Figure 3.7: Transmission coefficient for a downward propagating wave $T_{\rm down}$ as a function of incident wave frequency ($\omega/\bar{N}$) and scaled horizontal wavenumber $k_\perp d = \sqrt{l(l+1)}\epsilon$, for a range of stratification in the adjacent regions, N_a, N_b and a fixed step number, $m = 5$. Four cases $x = 1$ and $x = 0.1$ and $N_a = 0.8$, $N_b = 1.2$ and $N_a = 1.2$, $N_b = 0.8$. Over-plotted are the free modes of the same staircase (blue dashed lines), the frequency limits for wave propagation in the end regions (yellow for the top region and green for the bottom, respectively) and for the staircase if this was instead uniformly-stratified (red).

By similar analysis as is used to calculate the transmission coefficient, the reflection coefficient for downward and upward propagating waves can be shown to be,

$$T_{down} = \frac{|B_{m+1}|^2}{|A_{m+1}|^2}\frac{\mathrm{Im}[\lambda^*_{b_-}]}{\mathrm{Im}[\lambda^*_{b_+}]} = -\frac{|X^{-1}_{2,1}|}{|X^{-1}_{2,2}|}, \tag{3.21}$$

and,

$$T_{up} = \frac{|A_0|^2}{|B_0|^2}\frac{\mathrm{Im}[\lambda^*_{a_+}]}{\mathrm{Im}[\lambda^*_{a_-}]} = -\frac{|X_{1,2}|}{|X_{1,1}|}. \tag{3.22}$$

As there is no energy source or dissipation in the system, we know that,

$$R = 1 - T, \tag{3.23}$$

and the results have been validated by plotting $R+T$, and $R+T=1$ was verified to be true, to within machine precision.

3.3 Conclusion

In this chapter we have presented idealised calculations to study the transmission of waves in stably-stratified planetary layers containing a layered density structure. As in Chapter 2, for this first step in using a global model, we have omitted planetary rotation and adopted a simplified Boussinesq model in spherical geometry.

We have analysed the transmission of internal waves through a density staircase and found that additionally to the dependence on the free modes, trends in the transmission are affected by the parameters of a density staircase. This again extends and confirms prior work in Cartesian geometry (Sutherland, 2016; André et al., 2017).

The transmission of internal waves through a density staircase was shown to be a strong function of the properties of the incident wave and of the staircase. Waves with large wavelengths are efficiently transmitted, but shorter wavelength waves (comparable with a step-size) are strongly affected by the staircase and can be weakly transmitted. Efficient transmission for short-wavelength waves only occurs when the incident wave is resonant with a free mode of the staircase. This agrees with prior results in Cartesian geometry (André et al., 2017). Spherical geometry introduces an additional frequency cut-off to the propagation of waves dictated by the allowed frequencies in the adjacent convective regions. This has the most significant effect on transmission when the staircase size is comparable with the distance from the centre of the planet.

Chapter 4

Governing equations and numerical model

In the following three chapters we explore the tidal dissipation due to internal and inertial waves in giant planets by examining numerically how stable stratification can alter the excitation and dissipation of tidally forced waves. In this chapter we outline our methodology for studying these waves and will address the results in Chapters 5 and 6. We do this by extending André et al. (2019), in which tidal dissipation in semi-convective layers is studied in a Cartesian box model. Our extension employs a global spherical model and adopts similar methods to Ogilvie (2009).

In this initial study we adopt the simplified Boussinesq approximation, see Section 1.4, as this is the simplest computationally and allows for complementary analytical calculations. As we have discussed in the analysis in the preceding two chapters, although this is not a strictly valid approximation, it is likely to be reasonable for studying the dominant effects of stable stratification on tidally forced waves.

4.1 Governing equations

We build a global spherical model using spherical polar co-ordinates (r, θ, ϕ), which are centred on the planet of mass M and radius r_0. We will neglect the distortion from spherical geometry caused by centrifugal effects and tidal forcing by using spherical harmonics to describe the angular structure of solutions. Neglecting the tidal deformation is reasonable in giant planets due to the small tidal amplitudes (see Table 1.1). The neglect of rotational distortion, however, is more significant; although it would be possible to include this (e.g. Dewberry & Lai, 2022) we choose not to in this case as it would complicate analysis considerably, and is unlikely to significantly alter the conclusions.

We now outline how we arrive at the governing equations used in our numerical calculation. Considering the incompressible form of the momentum equation,

$$\rho\left(\frac{\partial \boldsymbol{u}}{\partial t} + \boldsymbol{u}\cdot\nabla\boldsymbol{u} + 2\boldsymbol{\Omega}\times\boldsymbol{u}\right) = -\nabla p + \rho\boldsymbol{g} + \rho\nu\nabla^2\boldsymbol{u} - \rho\nabla\psi, \tag{4.1}$$

where $\boldsymbol{u}$, p are velocity and pressure, ρ density and ψ the tidal potential and $\boldsymbol{\Omega}$ the uniform rotation of the body (neglecting differential rotation). We include dissipative effects, therefore ν denotes the kinematic viscosity which we are assuming to be constant in space and time. We have neglected self-gravity to allow us to more easily explore our system analytically and because it is only likely to lead to a small linear effect on the quantitative results. We linearise about a stationary background state, $\rho = \rho_0 + \tilde{\rho}$, $u = \tilde{u}$, $p = p_0 + \tilde{p}$, $\psi = \tilde{\psi}$, where terms denoted with a subscript 0 refer to the background state and those with a tilde the Eulerian perturbation. We note that the tidal potential does not have a zeroth order quantity ($\Psi_0 = 0$) leading to a spherically symmetric background state. By taking the Boussinesq approximation (see Section 1.4), to first order in perturbation it can be shown that,

$$\rho_0\left(\frac{\partial \boldsymbol{u}}{\partial t} + 2\boldsymbol{\Omega}\times\boldsymbol{u}\right) = -\boldsymbol{\nabla} p + \rho\boldsymbol{g} - \rho_0\boldsymbol{\nabla}\psi + \rho_0\nu\boldsymbol{\nabla}^2\boldsymbol{u}, \tag{4.2}$$

where tildes have been dropped for concise notation. Therefore, by defining the buoyancy variable $b = -\frac{\rho}{\rho_0}$, we find,

$$\frac{\partial \boldsymbol{u}}{\partial t} + 2\boldsymbol{\Omega} \times \boldsymbol{u} = -\frac{1}{\rho_0}\boldsymbol{\nabla} p + b\boldsymbol{g} - \boldsymbol{\nabla}\psi + \nu\boldsymbol{\nabla}^2\boldsymbol{u}. \tag{4.3}$$

Note that this is not the standard definition for the buoyancy variable b and does not have units of acceleration; instead it is a dimensionless quantity. This is done to allow us to define the radial dependence of the gravitational term separately, $\boldsymbol{g} = -g(r)\hat{r}$, which allows for easy manipulation of the model to account for different gravity profiles. In this study we focus predominantly on the gravity profile for a homogeneous body by considering $g = g_0 r$, where g_0 is the surface gravity with r measured in units of planetary radius. We will discuss how the results vary for a centrally condensed mass in Section 5.5, where we consider $g = \frac{g_0}{r^2}$. We consider our system to be incompressible and conservation of mass gives

$$\boldsymbol{\nabla} \cdot \boldsymbol{u} = 0. \tag{4.4}$$

Considering the following form of the heat equation (e.g. Landau & Lifshitz, 1987),

$$\frac{\partial T}{\partial t} + \boldsymbol{u} \cdot \nabla T = \kappa \nabla^2 T, \tag{4.5}$$

where T is our temperature and κ is the thermal diffusivity which, like viscosity, we consider to be constant in space and time. We again linearise by introducing a small perturbation, $T = T_0 + \tilde{T}$, $u = \tilde{u}$, and dropping the tildes, the first order perturbation is

$$\frac{\partial T}{\partial t} + \boldsymbol{u} \cdot \nabla T_0 = \kappa \nabla^2 T. \tag{4.6}$$

Using the thermodynamic relation, $\rho = \rho_0 - \alpha_T \rho_0 T$, where $\alpha_T = \frac{1}{V}\left(\frac{\partial V}{\partial T}\right)_p$ is the coefficient of expansion of the fluid (Tritton, 2012), it can be shown that

$$\frac{\partial b}{\partial t} + \frac{u_r}{g} N^2 = \kappa \boldsymbol{\nabla}^2 b, \tag{4.7}$$

where N^2 is the radially dependent Brunt-Väisälä frequency, or buoyancy frequency, defined to be,

$$N^2 = g\left(\frac{1}{\Gamma_1}\frac{\mathrm{d}\ln p_0}{\mathrm{d}r} - \frac{\mathrm{d}\ln \rho_0}{\mathrm{d}r}\right), \tag{4.8}$$

where $\Gamma_1 = \left(\frac{\partial \ln p_0}{\partial \ln \rho_0}\right)_{\mathrm{ad}}$ is the first adiabatic exponent. This is equivalent to the system used in Chapters 2 and 3, as well as Pontin et al. (2020), except for the addition of dissipative terms and realistic tidal forcing. As in those chapters, we approximate the buoyancy frequency to represent a density gradient as

$$N^2 \approx -\frac{g}{\rho_0}\frac{\mathrm{d}\rho_0}{\mathrm{d}r}. \tag{4.9}$$

We introduce tidal forcing into our model by considering the dominant $l = m = 2$ component of the tidal potential, see discussion in Section 1.3.1,

$$\psi = \psi_0\, r^2 Y_2^2(\theta, \phi) e^{-i\omega t}, \tag{4.10}$$

where $\psi_0 = \sqrt{\frac{6\pi}{5}}\frac{M_2}{M_1}\omega_d^2\left(\frac{r_0}{a}\right)^3$. In this case we have taken the $l = m = n = 2$ dimensional tidal amplitude for a circular orbit as defined in Ogilvie (2014). The forcing frequency is $\omega = 2(\Omega_s - \Omega_o)$, where Ω_o is the orbital frequency of the satellite and Ω_s the spin frequency of the planet. This is most relevant for a circular aligned orbit of a non-synchronously orbiting moon.

We expand the perturbations using spherical harmonics with a harmonic time-dependence such that,

$$u_r(r,\theta,\phi,t) = \sum_{l=m}^{\infty} \tilde{u}_r^l(r) Y_l^m(\theta,\phi) e^{-i\omega t}, \tag{4.11}$$

$$u_\theta(r,\theta,\phi,t) = r\sum_{l=m}^{\infty}\left[\tilde{u}_b^l(r)\frac{\partial}{\partial\theta} + \frac{\tilde{u}_c^l(r)}{\sin\theta}\frac{\partial}{\partial\phi}\right] Y_l^m(\theta,\phi) e^{-i\omega t}, \tag{4.12}$$

$$u_\phi(r,\theta,\phi,t) = r\sum_{l=m}^{\infty}\left[\frac{\tilde{u}_b^l(r)}{\sin\theta}\frac{\partial}{\partial\phi} - \tilde{u}_c^l(r)\frac{\partial}{\partial\theta}\right] Y_l^m(\theta,\phi) e^{-i\omega t}, \tag{4.13}$$

$$p(r,\theta,\phi,t) = \sum_{l=m}^{\infty} \tilde{p}^l(r) Y_l^m(\theta,\phi) e^{-i\omega t}, \tag{4.14}$$

$$b(r,\theta,\phi,t) = \sum_{l=m}^{\infty} \tilde{b}^l(r) Y_l^m(\theta,\phi) e^{-i\omega t}, \tag{4.15}$$

where the spherical harmonics have been normalized such that,

$$\int_0^{2\pi}\int_0^{\pi} [Y_{l'}^{m'}(\theta,\phi)]^* Y_l^m(\theta,\phi) \sin^2\theta \mathrm{d}\theta\mathrm{d}\phi = \delta_{l,l'}\delta_{m,m'}.$$

The resulting equations are (where again tildes have been dropped for clearer notation)

$$\begin{aligned}(-i\omega)u_r^l + 2\Omega r\Big(-imu_b^l + (l-1)q_l u_c^{l-1} - (l+2)q_{l+1}u_c^{l+1}\Big)& \\ = -\frac{1}{\rho_0}\frac{\mathrm{d}p}{\mathrm{d}r} + gb^l - \frac{\mathrm{d}\psi^l}{\mathrm{d}r}\delta_{l,2} - \nu\frac{l(l+1)}{r^2}\Big[u_r^l - \frac{\mathrm{d}}{\mathrm{d}r}(r^2u_b^l)\Big],&\end{aligned} \tag{4.16}$$

$$\begin{aligned}(-i\omega)r^2u_b^l + 2\Omega r^2\left(\frac{-im}{l(l+1)}\left(\frac{u_r^l}{r}+u_b^l\right) + \frac{l-1}{l}q_l u_c^{l-1} + \frac{l+2}{l+1}q_{l+1}u_c^{l+1}\right)& \\ = -\frac{p^l}{\rho_0} - \psi^l\delta_{l,2} + \nu\left[\frac{2u_r^l}{r} + \frac{1}{r^2}\frac{\mathrm{d}}{\mathrm{d}r}\left(r^4\frac{\mathrm{d}u_b^l}{\mathrm{d}r}\right) - (l-1)(l+2)u_b^l\right],&\end{aligned} \tag{4.17}$$

$$\begin{aligned}(-i\omega)r^2u_c^l + 2\Omega r^2\Bigg(\frac{-im}{l(l+1)}u_c& \\ + \frac{q_l}{l}\frac{u_r^{l-1}}{r} - \frac{q_{l+1}}{l+1}\frac{u_r^{l+1}}{r} + \frac{l-1}{l}q_l u_b^{l-1} - \frac{l+2}{l+1}q_{l+1}u_b^{l+1}\Bigg)& \\ = \nu\left[\frac{1}{r^2}\frac{\mathrm{d}}{\mathrm{d}r}\left(r^4\frac{\mathrm{d}u_c^l}{\mathrm{d}r}\right) - (l-1)(l+2)u_c^l\right],&\end{aligned} \tag{4.18}$$

$$\frac{1}{r^2}\frac{\mathrm{d}}{\mathrm{d}r}(r^2u_r^l) - l(l+1)u_b^l = 0, \tag{4.19}$$

$$(-i\omega)b^l + N^2\frac{u_r^l}{g} = \kappa\left[\frac{1}{r^2}\frac{\mathrm{d}}{\mathrm{d}r}\left(r^2\frac{\mathrm{d}b^l}{\mathrm{d}r}\right) - \frac{l(l+1)}{r^2}b^l\right], \tag{4.20}$$

where $q_l = \left(\frac{l^2-m^2}{4l^2-1}\right)^{\frac{1}{2}}$, consistent with those in Ogilvie (2009). The equations for each m are inherently uncoupled due to the axisymmetric basic state, but the Coriolis term couples components with different angular wavenumber l. Hence, we solve our system for $m = 2$ and l from 2 to l_{max}, where l_{max} is taken to be sufficiently large such that the solution converges. Typically when including rotation l_{max} is taken to be between 60 and 100.

We non-dimensionalise our system using units of length in terms of the planetary radius r_0, the Boussinesq reference density ρ_0 for density, and our unit of time is the dynamical frequency of the system, $\omega_d = \sqrt{GM/r_0^3}$, where G is the gravitational constant, M the planet mass. Therefore, we introduce the following dimensionless parameters, $r = r_0\hat{r}$, $u_r = r_0\omega_d\hat{u}_r$, $u_b = \omega_d\hat{u}_b$, $u_c = \omega_d\hat{u}_c$, $\psi = \psi_0\hat{\psi}$, $b = \hat{b}$, $g = g_0\hat{g}$, $p = \rho_0 r_0 g\hat{p}$, $\omega = \sqrt{\frac{g_0}{r_0}}\hat{\omega}$, where $g_0 = \omega_d^2 r_0$ is the surface gravity. We then drop the hats to simplify notation, giving us,

$$(-i\omega)u_r^l + 2\sqrt{\frac{r_0\Omega^2}{g_0}}r\Big(-imu_b^l + (l-1)q_l u_c^{l-1} - (l+2)q_{l+1}\xi_c^{l+1}\Big) = -\frac{1}{\rho_0}\frac{\mathrm{d}p^l}{\mathrm{d}r} + gb - \frac{\psi_0}{r_0 g_0}\frac{\mathrm{d}\psi^l}{\mathrm{d}r}\delta_{l,2} - \frac{\nu}{\sqrt{r_0^3 g_0}}\frac{l(l+1)}{r^2}\left[u_r^l - \frac{\mathrm{d}}{\mathrm{d}r}(r^2 u_b^l)\right], \quad (4.21)$$

$$(-i\omega)r^2 u_b^l + 2\sqrt{\frac{r_0\Omega^2}{g_0}}r^2\left(\frac{-im}{l(l+1)}\left(\frac{u_r^l}{r} + u_b^l\right) + \frac{l-1}{l}q_l u_c^{l-1} + \frac{l+2}{l+1}q_{l+1}u_c^{l+1}\right) = -p^l - \frac{\psi_0}{r_0 g_0}\psi^l\delta_{l,2} + \frac{\nu}{\sqrt{r_0^3 g_0}}\left[\frac{2u_r^l}{r} + \frac{1}{r^2}\frac{\mathrm{d}}{\mathrm{d}r}\left(r^4\frac{\mathrm{d}u_b^l}{\mathrm{d}r}\right) - (l-1)(l+2)u_b^l\right], \quad (4.22)$$

$$(-i\omega)r^2 u_c^l + 2\sqrt{\frac{r_0\Omega^2}{g_0}}r^2\Bigg(\frac{-im}{l(l+1)}u_c + \frac{q_l}{l}\frac{u_r^{l-1}}{r} - \frac{q_{l+1}}{l+1}\frac{u_r^{l+1}}{r} + \frac{l-1}{l}q_l u_b^{l-1} - \frac{l+2}{l+1}q_{l+1}u_b^{l+1}\Bigg) = \frac{\nu}{\sqrt{r_0^3 g_0}}\left[\frac{1}{r^2}\frac{\mathrm{d}}{\mathrm{d}r}\left(r^4\frac{\mathrm{d}u_c^l}{\mathrm{d}r}\right) - (l-1)(l+2)u_c^l\right], \quad (4.23)$$

$$\frac{1}{r^2}\frac{\mathrm{d}}{\mathrm{d}r}(r^2 u_r^l) - l(l+1)u_b^l = 0, \quad (4.24)$$

$$(-i\omega)b^l + \frac{N^2 r_0}{g_0}\frac{u_r^l}{g} = \frac{\kappa}{\sqrt{r_0^3 g_0}}\left[\frac{1}{r^2}\frac{\mathrm{d}}{\mathrm{d}r}\left(r^2\frac{\mathrm{d}b^l}{\mathrm{d}r}\right) - \frac{l(l+1)}{r^2}b^l\right]. \quad (4.25)$$

We highlight that we have four key dimensionless parameters,

$$\frac{\Omega}{\omega_d},\quad \frac{N^2}{\omega_d^2},\quad \frac{\nu}{r_0^2\omega_d}\quad \text{and}\quad \frac{\kappa}{r_0^2\omega_d}\quad \left(\text{or alternatively } Pr = \frac{\nu}{\kappa}\right),$$

which are varied in later analysis, and referred to simply as Ω, N^2, ν and Pr as we used units of $r_0 = 1$ and $\omega_d = 1$.

4.2 Boundary conditions

In our numerical calculations we enforce boundary conditions at either end of the domain, which extends from a non-zero inner core boundary αr_0 to the planet's radius r_0. We assume there is a rigid inner core that remains spherical, thereby neglecting any deformation caused by rotation or the tidal forcing. Therefore, we impose no normal flow at the inner core,

$$u_r^l = 0 \quad \text{at} \quad r = \alpha r_0. \tag{4.26}$$

At the tidally-perturbed outer boundary we consider it to be a free surface on which the normal stresses vanish. Therefore, we consider the perturbations to the normal stress to include the Lagrangian pressure perturbation Δp, and the normal viscous stress, i.e.

$$\Delta p - 2\nu e_{rr} = (\tilde{p} + \boldsymbol{\xi}\cdot\nabla p_o) - 2\nu e_{rr} = 0, \tag{4.27}$$

where $\tilde{p}$ is the Eulerian perturbation for this equation only. This can be evaluated to give the boundary condition,

$$W - \frac{g_0}{(-i\omega)}u_r^l - 2\nu\frac{\mathrm{d}u_r^l}{\mathrm{d}r} = \psi_0\delta_{l2} \quad \text{at} \quad r = r_0, \tag{4.28}$$

where g_0 is the surface gravity, which can be related to the dynamical frequency of the system $g\hat{\boldsymbol{r}} = -\omega_d^2 r\hat{\boldsymbol{r}}$ evaluated at r_0, and $W = \frac{p}{\rho_0} + \psi$, neglecting self-gravity.

At both boundaries, we consider stress-free conditions (no tangential stress), which is consistent with a free surface. Realistically we expect the inner core would be closer to non-slip but it is numerically convenient to consider stress-free conditions without it having any significant effect on the qualitative or quantitative results. This means that

$$\frac{\mathrm{d}u_b^l}{\mathrm{d}r} + \frac{u_r^l}{r^2} = 0 \quad \text{at} \quad r = \alpha r_0 \quad \text{and} \quad r = r_0, \tag{4.29}$$

$$\frac{\mathrm{d}u_c^l}{\mathrm{d}r} = 0 \quad \text{at} \quad r = \alpha r_0 \quad \text{and} \quad r = r_0. \tag{4.30}$$

We considered different boundary conditions on the buoyancy variable, however, we found that there was no significant effect on the results as long as the condition chosen did not contradict the governing equations. For the results shown in this study, we have considered the inner core to be fixed entropy, such that there is no perturbation to the quantity b, i.e.

$$b^l = 0 \quad \text{at} \quad r = \alpha r_0, \tag{4.31}$$

and no perturbation to the buoyancy flux through the surface, i.e.

$$\frac{\partial b^l}{\partial r} = 0 \quad \text{at} \quad r = r_0. \tag{4.32}$$

4.3 Energy balance

As we aim to further understanding on the dissipation of tidally forced internal waves, so we turn our attention to the energetic quantities and their balances. Considering the standard definition for work, the mean rate of energy injection by the tidal forcing is defined to be

$$I = \int_V \rho_0 (\boldsymbol{u} \cdot \boldsymbol{F}) \mathrm{d}V, \tag{4.33}$$

where $\boldsymbol{F} = -\nabla\psi$ is the tidal acceleration.

Therefore, by taking the scalar product of equation 4.3 with $\rho_0 \boldsymbol{u}$, using equation 4.7 and integrating over the volume, the following energy balance is found,

$$I = \frac{\mathrm{d}E_K}{\mathrm{d}t} + \frac{\mathrm{d}E_{PE}}{\mathrm{d}t} + \frac{1}{V}\oint_S p\boldsymbol{u}\cdot \mathrm{d}\boldsymbol{S} + D_{ther} + D_{visc}. \tag{4.34}$$

The rate of change of kinetic energy is,

$$\frac{\mathrm{d}E_K}{\mathrm{d}t} = \int_V \frac{\rho_0}{2}\frac{\partial |\boldsymbol{u}|^2}{\partial t}\mathrm{d}V, \tag{4.35}$$

and the rate of change of potential energy,

$$\frac{\mathrm{d}E_{PE}}{\mathrm{d}t} = \int_V \frac{g^2}{2N^2}\frac{\partial b^2}{\partial t}\mathrm{d}V, \tag{4.36}$$

except when $N = 0$, in which case $E_{PE} = 0$ and $\frac{\mathrm{d}E_{PE}}{\mathrm{d}t} = 0$. The volume integrated viscous dissipation rate is given by,

$$D_{visc} = -\int_V \rho_0 \nu \boldsymbol{u}\cdot\nabla^2\boldsymbol{u}\mathrm{d}V, \tag{4.37}$$

and volume integrated thermal dissipation rate is written,

$$D_{ther} = -\int_V \rho_0 \kappa \frac{g^2}{N^2} b\nabla^2 b\mathrm{d}V, \tag{4.38}$$

again as for potential energy when $N = 0$, $D_{ther} = 0$.

In Appendix A, we show how the viscous dissipation can be divided into two separate components. These consist of the viscous dissipation within the bulk of the fluid and the normal viscous stresses. The viscous dissipation within the bulk can be written (Ogilvie, 2009),

$$\begin{aligned} D_{interior} = \frac{\rho_0 \nu}{2}\sum_l \Bigg(l(l+1)\left(\left|\frac{u_r^{l*}}{r} + r\frac{\mathrm{d}u_b^l}{\mathrm{d}r}\right|^2 + \left|r\frac{\mathrm{d}u_c^l}{\mathrm{d}r}\right|^2\right) + 3\left|\frac{\mathrm{d}u_r^l}{\mathrm{d}r}\right|^2 \\ + (l-1)l(l+1)(l+2)\left(|u_b^l|^2 + |u_c^l|^2\right)\Bigg). \end{aligned} \tag{4.39}$$

Throughout this thesis when considering viscous dissipation we consider the quantity defined in equation 4.37, however we note that in this model, with the parameters considered, the difference between these quantities is negligible.

Using the divergence theorem, the mean energy injection rate from the tidal forcing can be written in the form,

$$I = \int_V \rho_0 \boldsymbol{u} \cdot (-\nabla\psi)\mathrm{d}V = -\oint_S \rho_0 \psi \boldsymbol{u} \cdot \mathrm{d}\boldsymbol{S}. \tag{4.40}$$

In a steady state, averaged over the forcing period of $\frac{2\pi}{\omega}$, the kinetic and potential energy terms (equations 4.35 and 4.36) will be identically zero. Therefore, the injection rate I will balance the total viscous and thermal dissipation terms, D_{vsic} and D_{ther}. It can be shown numerically that an additional balance between the dissipation within the bulk of the fluid defined in equation 4.39, and the pressure integral in equation 4.34 also exists. In the following chapters we will analyse further how the dissipation rates D_{visc} and D_{ther} depend on other properties of the system. For some analysis in this thesis D_{ther} has been calculated by considering this balance, as it is less numerically demanding to reach a converged result.

4.4 Density structure

We want to consider regions in a giant planet where stable layers have formed, or which could have evolved into semi-convective layers due to double-diffusive convection. As discussed in Chapter 1 there are two regions to consider, one close to the core, or alternatively somewhere near the H/He molecular to metallic transition radius.

To incorporate both continuous stable stratification and semi-convective layers in our model, as well as considering multiple locations for these layers, we define the buoyancy frequency in several ways. First, we consider a density profile representative of a continuous stably stratified region, with a constant N which sits

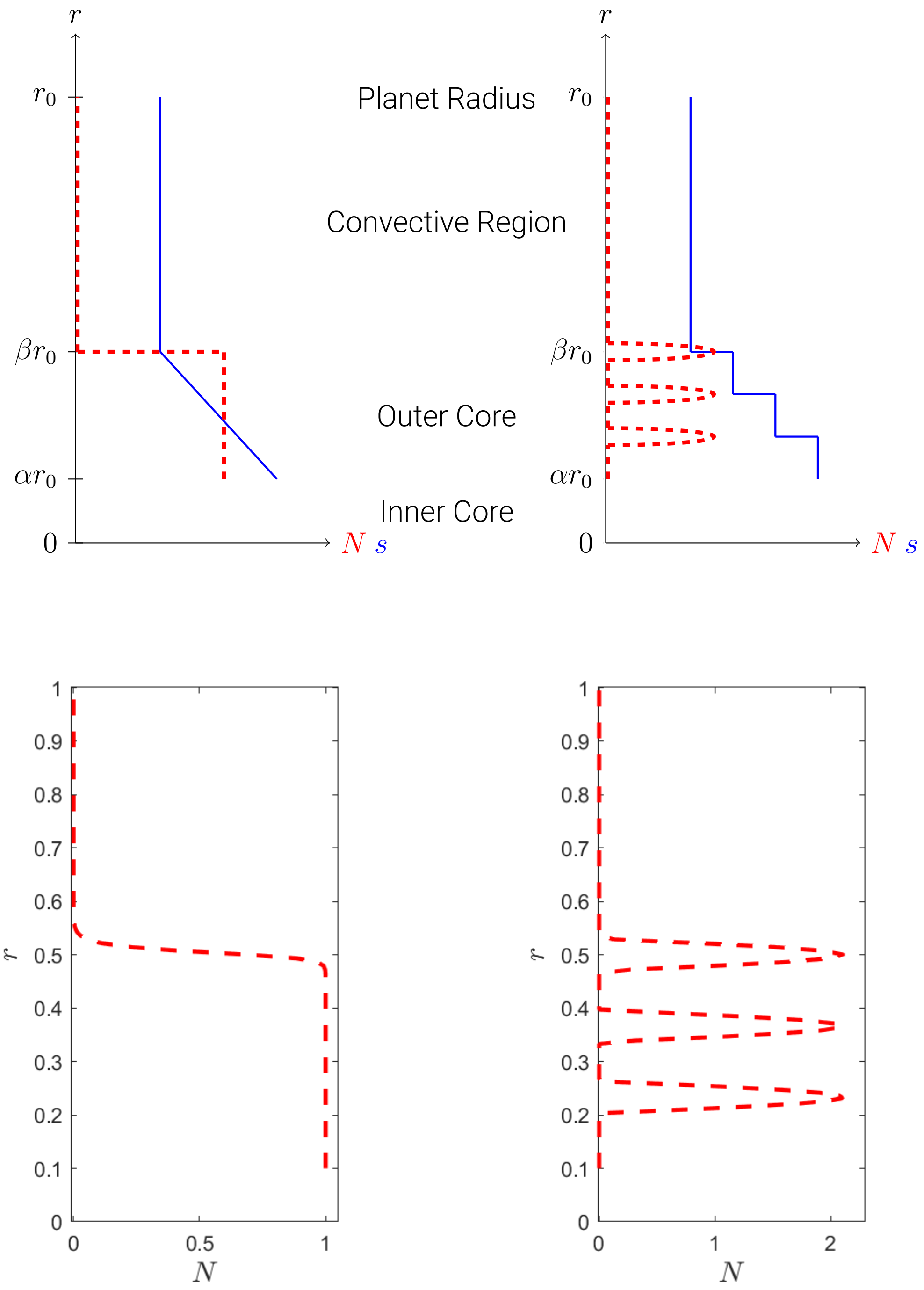

Figure 4.1: Illustrative examples of the entropy profile and Brunt-Väisälä frequency (N^2) for both a continuously stratified layer (left hand side) and semi-convective layers (right hand side). In both cases there is a solid inner core that extends to αr_0, outer core containing a stable stratification extending to βr_0, and planetary radius r_0. The bottom panels show examples of the numerically smooth profiles used.

above the solid core extending a defined distance into the planetary envelope. This is shown on the left hand side of Figure 4.1. This is described by a step function in the buoyancy profile $N^2(r)$ that is non-zero from the inner core boundary αr_0 to the outer core boundary βr_0. To allow for numerical calculations to be executed, when the stable layer does not extend to the planetary surface ($\beta \neq 1$), we consider a smoothly varying buoyancy profile,

$$N^2(r) = \frac{\bar{N}^2}{2}\Big(\tanh\big(\Delta(\beta r_0 - r)\big) + 1\Big). \tag{4.41}$$

Unless specified otherwise the value of $\Delta = 100$. For numerical reasons, the buoyancy term is set to be identically zero away from the step, when $N^2(r) < \frac{\bar{N}^2}{10^7}$. For cases where $\beta = 1$ the buoyancy profile is constant throughout the domain,

$$N^2(r) = \bar{N}^2. \tag{4.42}$$

The second density structure used represents a semi-convective structure with n_{max} steps within the stratified layer. We want to consider a series of δ-functions in the buoyancy variable to give a staircase-like density profile, shown on the right hand side of Figure 4.1. To do this numerically, we consider finitely thin and smoothly varying interfaces by taking N to be,

$$N^2(r) = \begin{cases} \frac{N_0^2}{2}\Big(1 + \cos\Big(2\pi\frac{r-r_n}{\delta r}\Big)\Big) & |r - r_n| < \frac{\delta r}{2}, \\ 0 & \text{otherwise}, \end{cases} \tag{4.43}$$

for $1 < n < n_{max}$, where $r_n = \alpha r_0 + nd$, $d = \frac{(\beta-\alpha)r_0}{n_{max}}$, and $\epsilon = \frac{\delta r}{d}$.

N_0^2 is set to a value which gives a mean stratification for the staircase equivalent to a region with constant stratification $\bar{N}^2$,

$$N_0^2 = \bar{N}^2\frac{(\beta-\alpha)r_0}{n_{max}\,\delta r}. \tag{4.44}$$

This allows for comparison between a stratified layer and semi-convective region.

Note that if $\beta = 1$, the profile is adjusted such that the final step isn't included at the planetary radius ($0 < n < n_{max} - 1$), and N_0 is adjusted to maintain the mean stratification.

Finally, the formulation in equation 4.43 can also be used to represent a stratified layer at the metallic/molecular transition zone, where instead of multiple steps we consider one wide step in the transition region,

$$N^2(r) = \begin{cases} \frac{N_0^2}{2}\left(1 + \cos\left(2\pi\frac{r-\beta}{\delta r}\right)\right) & |r - \beta| < \frac{\delta r}{2}, \\ 0 & \text{otherwise}, \end{cases} \tag{4.45}$$

and

$$N_0^2 = \bar{N}^2\frac{(r_0 - \alpha)r_0}{\delta r}. \tag{4.46}$$

This single step can be used as an isolated region of stable stratification embedded within a convective medium. The choice of N_0 to compare with a stratified layer across the entire domain is somewhat arbitrary as it is not insightful to make comparisons between these quantities.

4.5 Frequency-averaged dissipation

Although the response to tidal forcing is known to be inherently dependent on the forcing frequency (e.g. Ogilvie & Lin, 2004; Fuller et al., 2016; André et al., 2019), to fully explore the system's dependence on the parameters and functional form of the stratification profile, it is helpful to define a quantity that gives a quantitative measure of the dissipation that can be compared as the parameters are varied. Therefore, we consider the frequency-averaged dissipation as a measure of overall dissipation (Ogilvie, 2014),

$$\bar{D} = \int_{\omega_{min}}^{\omega_{max}} \frac{D(\omega)}{\omega}\,\mathrm{d}\omega. \tag{4.47}$$

This gives more emphasis to the lower frequency values which are expected to be more significant when considering a tidally forced system. We take a numerically appropriate non-zero limit for the lower bound of the integral, found by checking for convergence of the results. Unless otherwise stated, ω_{max} is taken to be $\bar{N}$. This allows analysis of the low frequency dependence without it being dominated by the surface gravity (f-mode) behaviour. Removing the surface gravity mode and this limit and the $\frac{1}{\omega}$ weighting is appropriate to study planet-satellite systems where we expect the tidal forcing to be small compared to the dynamical frequency of the body. Note, in Chapter 6 we compare this quantity with different integrated quantities.

4.6 Comparison to a simple harmonic oscillator

Parallels exist between the response of a body to a tidal potential and that of a forced, damped, simple harmonic oscillator. For this reason, a simple harmonic oscillator is often used as an analogy for a planet-moon system and is helpful for understanding some of our later results. Considering a forced, damped, simple harmonic oscillator for a quantity $a(t)$ with a single resonant frequency ω_0, we can write,

$$\frac{\mathrm{d}^2 a}{\mathrm{d}t^2} + \omega_0^2 a = \hat{F}\cos\omega t - \epsilon\omega_0 \frac{\mathrm{d}a}{\mathrm{d}t}, \tag{4.48}$$

where $\hat{F}\cos\omega t$ is the forcing and $\epsilon\omega_0\frac{\mathrm{d}a}{\mathrm{d}t}$ is the damping. By considering a solution of the form $\mathrm{Re}[\hat{a}\, e^{-i\omega t}]$, dissipation can be shown to be,

$$D = \left\langle \epsilon \left(\frac{\mathrm{d}a}{\mathrm{d}t}\right)^2 \omega_0 \right\rangle \propto \frac{\epsilon\omega_0\omega^2}{(\omega_0^2 - \omega^2)^2 + \epsilon^2\omega_0^2\omega^2}. \tag{4.49}$$

From this we can see there is a resonance at $\omega = \pm\omega_0$ and if we consider the dissipation at these frequencies, we find

$$D_{max} \propto \frac{1}{\epsilon\omega_0}, \tag{4.50}$$

showing there is a clear inverse relationship between the damping rate ϵ and the peak dissipation.

We define the edge of a peak to be the frequency at which the dissipation has decreased to half the maximum peak height. The frequencies either side of $\pm\omega_0$ where this value is reached are,

$$\omega_{+,\frac{1}{2}} = \frac{\omega_0}{2}\Big(\pm \epsilon + \sqrt{\epsilon^2+4}\Big), \tag{4.51}$$

and similarly for $-\omega_0$

$$\omega_{-,\frac{1}{2}} = \frac{\omega_0}{2}\Big(\pm \epsilon - \sqrt{\epsilon^2+4}\Big). \tag{4.52}$$

Therefore the half-width of the peak Δ is

$$\Delta = \epsilon\omega_0, \tag{4.53}$$

showing there is a linear relationship between damping rate and peak width. We refer to these two relationships when discussing our findings in later chapters.

4.7 Eigenvalue problem

It is informative to see how the dissipation patterns correspond with the expected free modes of the system. Although we gained some understanding of the possible free modes for the inviscid case in Chapter 2, we can also examine these by considering the numerical eigenvalues of the dissipative system.

To do this we consider the unforced case where $\psi_0 = 0$, which becomes the following generalised linear eigenvalue problem with eigenvalue $(-i\omega)$,

$$(-i\omega)\boldsymbol{A}\begin{bmatrix}\boldsymbol{u}\\ p\\ b\end{bmatrix} = \boldsymbol{B}\begin{bmatrix}\boldsymbol{u}\\ p\\ b\end{bmatrix}, \tag{4.54}$$

where $\boldsymbol{A}$ and $\boldsymbol{B}$ are matrices that describe equations 4.21 to 4.25 with $\psi_0 = 0$ and we keep the same boundary conditions. This is then solved using an inbuilt MATLAB linear algebra routine, to give the eigenvalues ($-i\omega$), and the corresponding eigenvectors for $\boldsymbol{u}$, p, b. We can then consider the $\mathrm{Re}[\omega]$ and $\mathrm{Im}[\omega]$ parts separately as they are the frequency of the mode, and the associated damping rate, respectively. We use the iterative "eigs" method to scan the relevant frequency range as a non-iterative method would be prohibitive in its memory requirements in the rotating case.

4.8 Numerical method

We solve the system of ordinary differential equations in radius, equations 4.21 to 4.25 for each l using a Chebyshev collocation method, where the ordinary differential equations in r are converted into a linear system of equations on a Chebyshev grid.

Remembering that the angular dependence has been handled by the use of spherical harmonics, we consider points in radius as a set of $(n_{cheb} + 1)$ Gauss-Lobatto-Chebyshev points, which are defined as,

$$x_j = \cos\left(\frac{j\pi}{N_c}\right), \quad j = 0, \cdots, N_c, \tag{4.55}$$

where N_c is taken as the value for which convergence is found. This value varies with choice of density structure and parameters, but we typically take $N_c = 100$ to $N_c = 400$. These are an appropriate choice of basis for many non-periodic problems and have been shown to have good convergence properties (Boyd, 2001). In particular, spectral methods such as this converge exponentially fast with resolution N_c for smooth solutions (Boyd, 2001).

We consider our system as a linear algebra problem by converting the differential operators into differentiation matrices using polynomial interpolation

(Trefethen, 2000; Boyd, 2001). By considering the linear interpolation of a polynomial $p(x)$, through two data points v_0 and v_1 at positions x_0 and x_1, respectively,

$$p(x) = \frac{(1+x)v_0 + (1-x)v_1}{x_0 - x_1}, \tag{4.56}$$

for which the derivative is

$$p'(x) = \frac{v_0 - v_1}{x_0 - x_1}. \tag{4.57}$$

We can see in this case that the 2×2 derivative matrix would be,

$$D = \begin{pmatrix} \frac{1}{x_0-x_1} & \frac{-1}{x_0-x_1} \\ \frac{1}{x_0-x_1} & \frac{-1}{x_0-x_1} \end{pmatrix}. \tag{4.58}$$

This can be extended to arbitrary N_c by considering the general form of polynomial interpolation (Trefethen, 2000),

$$p_j(x) = \frac{1}{a_j} \prod_{\substack{k=0 \\ k \neq j}}^{N_c} (x - x_k), \quad \text{where} \quad a_j = \prod_{\substack{k=0 \\ k \neq j}}^{N_c} (x_j - x_k), \tag{4.59}$$

which differentiates to,

$$p_j'(x) = p_j(x) \sum_{\substack{k=0 \\ k \neq j}}^{N_c} (x - x_k)^{-1}. \tag{4.60}$$

Therefore, the components of the general differentiation matrix are written,

$$D_{ij} = \frac{1}{a_j} \prod_{\substack{k=0 \\ k \neq j}}^{N_c} (x_i - x_k) = \frac{a_i}{a_j(x_i - x_j)} \quad \text{for} \quad i \neq j, \tag{4.61}$$

and

$$D_{jj} = \sum_{\substack{k=0 \\ k \neq j}}^{N_c} (x_j - x_k)^{-1}. \tag{4.62}$$

The general form for arbitrary N_c on a set of Chebyshev grid points $\{x_j\}$ is (Trefethen, 2000),

$$(D_{N_c})_{00} = \frac{2n^2 + 1}{6}, \tag{4.63}$$

$$(D_{N_c})_{N_cN_c} = \frac{-2n^2+1}{6}, \tag{4.64}$$

$$(D_{N_c})_{jj} = \frac{-x_j}{2(1-x_j)^2}, \quad j = 1, \dots, N_c - 1, \tag{4.65}$$

$$(D_{N_c})_{ij} = \frac{c_i}{c_j}\frac{(-1)^{i+j}}{(x_i - x_j)}, \quad i \neq j, \quad j = 1, \dots, N_c \quad \text{where} \quad c_i \begin{cases} 2, & i = 0 \text{ or } N_c, \\ 1, & \text{otherwise.} \end{cases} \tag{4.66}$$

which is shown more clearly in Figure 4.2 taken from Trefethen (2000).

Now we have a linear algebra problem which we solve using the inbuilt MATLAB routine “mldivide”, where matrices are stored in sparse form to reduce the numerical memory requirements. The solutions for $\boldsymbol{u}$, p and b can then be used in equations 4.37 and 4.38.

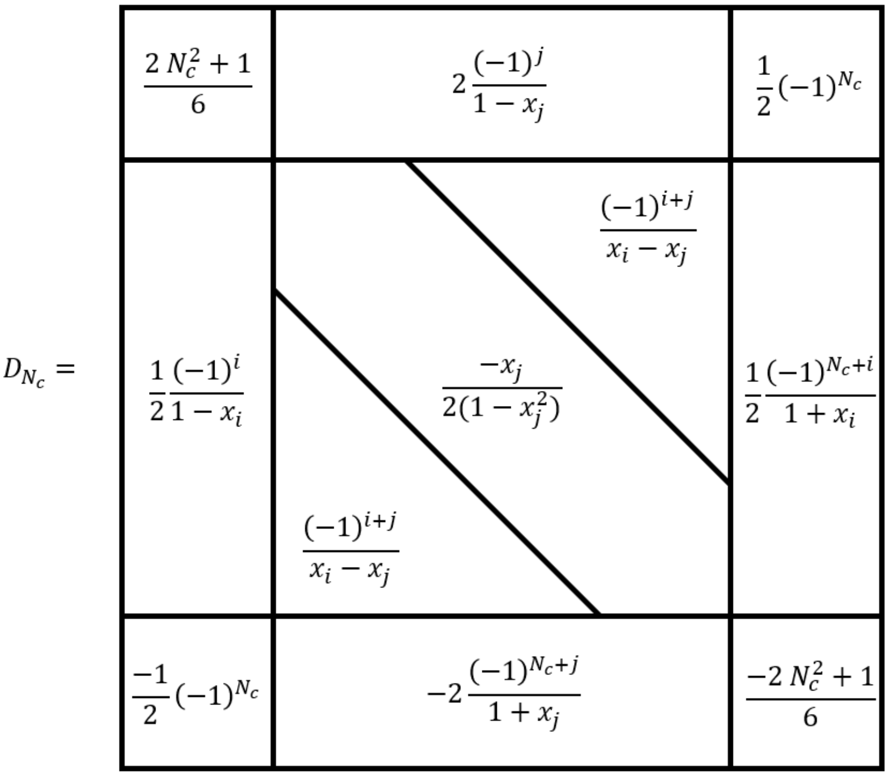

Figure 4.2: Schematic of the Chebyshev differentiation matrix using $N_c + 1$ points, adapted from Trefethen (2000).

Chapter 5

Tidal dissipation in stratified planets

Having established the framework for our numerical work in the preceding chapter we now consider the results for the case of a non-rotating body with $\Omega = 0$. This will allow us to gain an initial understanding of the system with reduced numerical cost, and complementary analytical calculations, before turning our attention to the inclusion of rotation and its additional effects in Chapter 6.

We use the governing equations and methods introduced in Chapter 4 to find the eigenvalues and linear response to tidal forcing, including dissipation rates of the system. We will discuss the basic properties of our system before considering how the dissipative properties depend on the model's key parameters, and discuss the implications for astrophysical tidal evolution.

5.1 Outline of key features

First, we summarise the overarching trends that we observed when evaluating the frequency dependence of the viscous, thermal and total dissipation, defined by equations 4.37 and 4.38. We know from previous studies, both with and without rotation, that the magnitude of the dissipation has a strong dependence on the

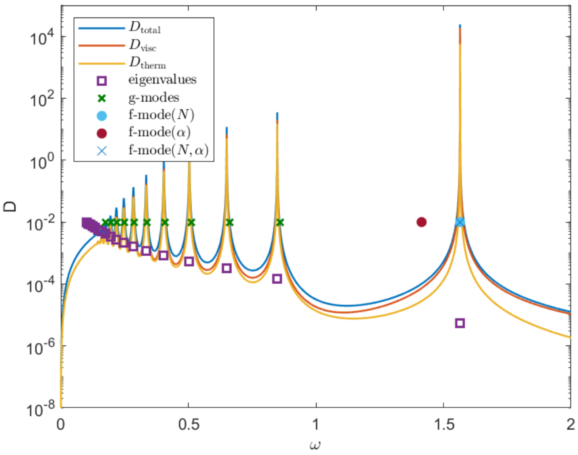

(a) $\alpha = 0.1$, $\beta = 1.0$, $\bar{N}^2 = 1$, $\nu = \kappa = 10^{-6}$

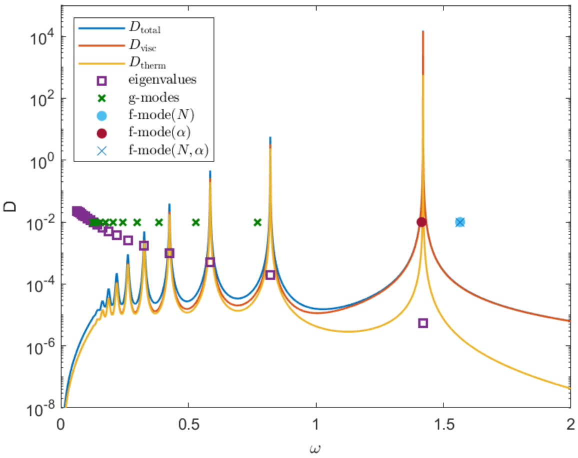

(b) $\alpha = 0.1$, $\beta = 0.5$, $\bar{N}^2 = 1$, $\nu = \kappa = 10^{-6}$

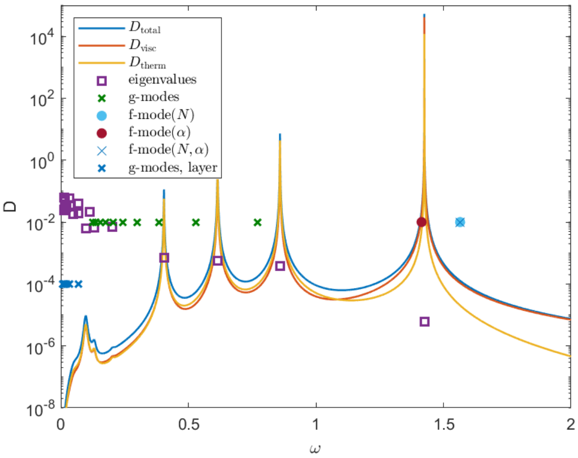

(c) $\alpha = 0.1$, $\beta = 0.5$, $\bar{N}^2 = 1$, steps$= 3$, $\delta r = 0.06$, $\nu = \kappa = 10^{-6}$

Figure 5.1: Illustrative examples of the dissipation as a function of frequency with eigenvalue solutions and analytical calculations for two cases considering uniform stratification (panels a and b), and one considering semi-convective layers (panel c). The y-axis values for the analytical calculations are arbitrary and those for eigenvalue frequencies are the associated damping rates.

forcing frequency (e.g. Ogilvie & Lin, 2004; Ogilvie, 2009; André et al., 2019) and indeed we find this again here.

Illustrative examples for three different profiles are shown in Figure 5.1, where we can see a strong frequency dependence. They show viscous (D_{visc}), thermal (D_{therm}), and total ($D_{visc} + D_{therm}$) dissipation rates as a function of the forcing frequency (ω). The eigenvalue solutions for the frequencies of the free modes for each case have been found using the methods described in Section 4.7. These are shown by the purple squares and in this case we plot the frequency of the mode ($\mathrm{Re}[\omega]$) on the x-axis and the damping rate ($\mathrm{Im}[\omega]$) on the y-axis. The green crosses show the analytical calculation for the frequencies of the g-modes, as derived in Appendix B. Circles show the analytical calculation for the frequencies of the f-mode, shown in Appendix C. For all analytical calculations the y-axis values are arbitrary. Dissipation D is measured in units of $\rho_0 r_0^5 \omega_d^3$, and ω is shown in units of ω_d. In all three cases we have fixed the following parameters; inner core $\alpha = 0.1$, mean stratification $\bar{N} = 1$,viscosity, thermal diffusivity and Prandtl number $\nu = \kappa = 10^{-6}$, $Pr = 1$.

Figure 5.1a is an example of a fully stratified interior, where a stably stratified layer with constant buoyancy frequency $\bar{N} = 1$ extends from the solid inner core all the way to the planetary radius, described by equation 4.41 with $\beta = 1$ and $\bar{N} = 1$. Figure 5.1b similarly contains a uniformly stratified region, however in this case it extends to half the planetary radius ($\beta = 0.5$). Finally, Figure 5.1c has a stratified layer that is equivalent to that shown in Figure 5.1b but with a staircase structure as described by equation 4.43 with $\beta = 0.5$. In this case we consider also steps $= 3$ and $\delta r = 0.06$. In these (and all following non-rotating) cases we only show positive frequencies as the results are symmetric about $\omega = 0$, $D(\omega) = D(-\omega)$, leading to no further information when considering negative frequencies.

In all three cases we observe many tall narrow peaks of enhanced dissipation which occur over an extended frequency range. We note that the locations and magnitudes of these peaks vary considerably between these three

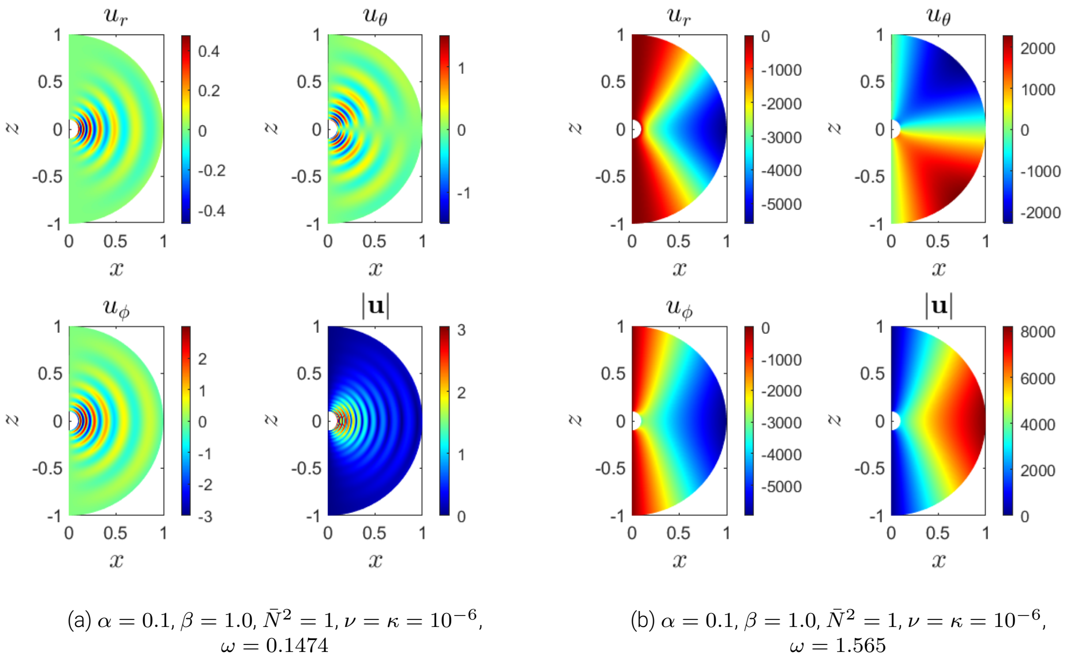

(a) $\alpha = 0.1, \beta = 1.0, \bar{N}^2 = 1, \nu = \kappa = 10^{-6}$, $\omega = 0.1474$

(b) $\alpha = 0.1, \beta = 1.0, \bar{N}^2 = 1, \nu = \kappa = 10^{-6}$, $\omega = 1.565$

Figure 5.2: Illustrative examples of the forced response at two different frequencies for uniform stable stratification with constant N^2. Panel a is an example of an internal gravity wave (g-mode) and panel b a surface gravity (f-mode) wave.

examples. This is due to the strong link between the stratification profile and the properties of the modes, something we explore further in this section. This is carried out by examining the peaks and trends in dissipation, as well as comparisons to both the eigenvalue solutions from Section 4.7 and analytical calculations for the modes from the Appendices B and C.

Uniform stable stratification extending to the planetary radius

We look first at Figure 5.1a, in which we are considering uniform stable stratification with $N^2 = 1$ throughout, which allows for internal gravity waves (g-modes) to be excited and subsequently dissipated. These appear as a regular, discrete set of peaks, visible at frequencies less than $\bar{N}$, in agreement with the expected range. The purple squares are the frequencies found from the corresponding eigenvalue problem, where the x-axis is the frequency of oscillation $\mathrm{Re}[\omega]$, and the y-axis is the magnitude of the damping rate of the mode $\mathrm{Abs}\left[\mathrm{Im}[\omega]\right]$; note all modes are stable, as expected for $\bar{N} > 0$. We see very good agreement between the eigenvalue solution and the sharp resonant peak and a clear increase in damping rate as the forcing frequency decreases. This corresponds with the clear decrease in peak height and increase in width in agreement with our expectations based on the forced damped simple harmonic oscillator discussed in Section 4.6. The green crosses which represent the analytical prediction of the internal gravity mode frequencies also agree well with the dissipation peaks. The slight discrepancies are expected due to neglected factors in the analytical calculation (viscosity, thermal diffusivity, and the departure from the free-surface condition by the use of solid wall boundary conditions). The discrepancies are more significant at higher frequencies, although these solutions have a larger characteristic wavelength and are therefore less affected by viscosity; they are more affected by the free surface condition, which has a larger contribution to shifting the mode frequency. In this case we do not have a straightforward value for the damping rate as dissipation was neglected to allow for analytical solutions, therefore the $y-$axis value is arbitrary.

To understand the mode properties further we look at the spatial structure of the solutions at a given frequency. Figure 5.2a shows the forced response for the uniform case shown in Figure 5.1a at a frequency of $\omega = 0.1474$, well within the range characteristic of internal gravity waves ($\omega < \bar{N}$). We observe a series of oscillations in r, characteristic of an internal gravity wave, where the number of nodes (and corresponding wavelength) is frequency dependent, with wavelength decreasing with decreasing frequency. Figure 5.2b shows the solution at $\omega = 1.565$, also for the model shown in Figure 5.1a. This is the surface gravity (f-mode) response, introduced because we are using the free surface boundary condition at the planetary surface. It corresponds to the large peak around $\omega = 1.5$, approximately $\omega = \omega_d\sqrt{\ell}$ with $l = 2$. This is the expected location of the surface gravity mode for a homogeneous body, neglecting self-gravity, being forced with a $l = m = 2$ forcing term (Barker et al., 2016). In this case the mode has been shifted to a higher frequency due to effects of both the finite core size and stable stratification. The analytical approximations incorporating both of these shifts are provided in Appendix C and are plotted on Figure 5.1a. The shift due to a stably

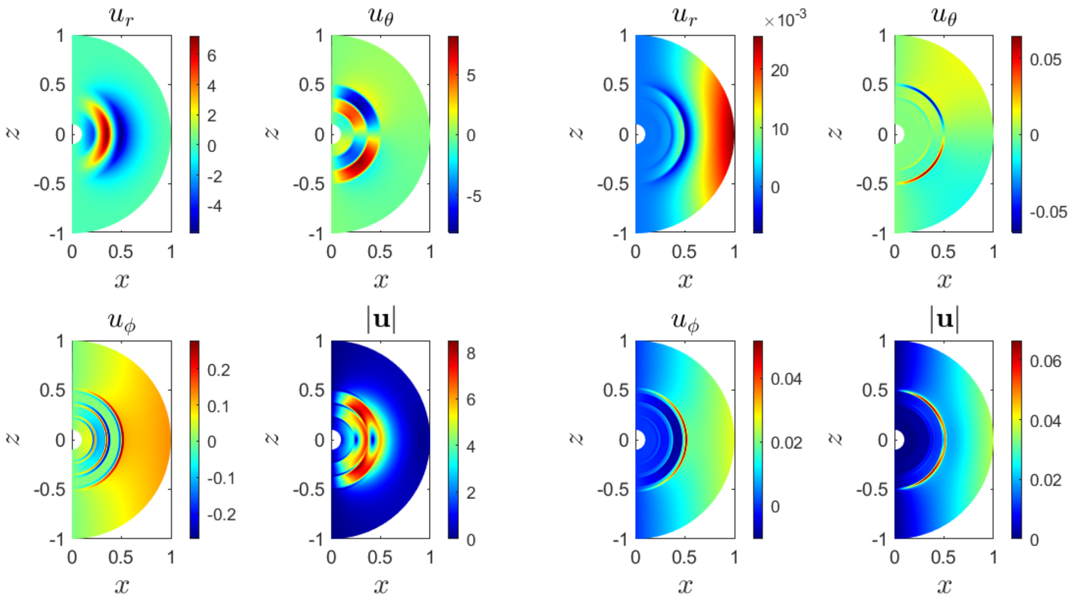

(a) $\alpha = 0.1$, $\beta = 0.5$, $\bar{N}^2 = 1$, steps$= 3$, $\nu = \kappa = 10^{-6}$, $\omega = 0.4037$

(b) $\alpha = 0.1$, $\beta = 0.5$, $\bar{N}^2 = 1$, steps$= 3$, $\nu = \kappa = 10^{-6}$, $\omega = 0.09359$

Figure 5.3: Illustrative examples of the forced response at two different frequencies for semi-convective layers with a staircase-like density structure. Panel a is an example of an interfacial mode where the staircase interfaces give a "g-mode like" response, and Panel b a short wavelength g-mode forming within the finite width of an interface.

stratified interior is shown by the blue circle and can be seen to agree well with the resulting resonance; the shift due to a finite core size in this case is far less significant than the shift due to stratification and therefore can be neglected. The shape of this response is characteristic of a Y_2^2 spherical harmonic shape, which can be identified by the single zero crossing in θ, as the number of zero crossings is equal to $l - |m|$. Note this calculation neglects rotation and therefore we only solve for $l = m = 2$ as all l's are decoupled.

Uniform stable stratification extending to half the planetary radius

Figure 5.1b, the case where uniform stratification extends to half the planetary radius, has many similar properties to Figure 5.1a. We again see the regular, discrete set of peaks at frequencies less than the buoyancy frequency, $\omega < \bar{N}$, corresponding to internal gravity modes, and a resonance with the surface gravity mode around $\sqrt{2}$, all of which agree well with the eigenvalue solutions. However, we can also see there are a number of differences, most notably in our agreement with analytical calculations. The agreement with the analytical calculation of the internal gravity modes (Appendix B) is significantly worse. As we are now considering a stratified layer beneath a convective medium, the use of solid wall boundary conditions is more significant. The frequency of the surface gravity mode peak agrees more closely with the predicted shift due to a finite core than that of a stratified planet, which is expected because our analytical calculation neglects the convective envelope. Finally we note that the overall magnitude of dissipation is lower; this will be discussed further in Section 5.2.2. Further analysis of the spatial structure shows similar behaviour as in the previous case and therefore has not been included.

Staircase structure extending to half the planetary radius

Figure 5.1c shows the dissipation in a system with a semi-convective layer where a staircase-like density profile sits above the core, extending to half the planetary radius, above which we have a convective region. This is relevant as a staircase is a potential result of double-diffusive convection in giant planet interiors. As in the first two examples, we see good agreement with the eigenvalue solutions (purple squares) in both oscillatory frequency and damping rate.

The staircase we are considering has three steps and we observe three clear corresponding peaks. These peaks align with three interfacial gravity wave frequencies of the system which correspond to the modes found and discussed in Chapter 2 and Pontin et al. (2020). Figure 5.3a shows the forced solution at $\omega = 0.4037$, where the adjacent interfaces can be seen to be oscillating out of phase with one another, exhibiting "g-mode like" behaviour. This mode is analogous to that of an internal gravity mode with three interior nodes. The green crosses show the predicted values for an equivalent uniformly stratified layer, and we can see that although the interfacial mode peaks appear in the same frequency range as the internal gravity modes $\omega < \bar{N}$, the exact frequency of the peaks has been shifted due to the properties of the staircase.

Additionally in Figure 5.1c, we can see a small collection of resonances at low frequencies, approximately near $\omega = 0.1$, an example of which is shown in Figure 5.3b. These are internal gravity wave modes sustained by the finite width of the interfaces. These small regions of stable stratification allow the internal modes to exist, which in turn allow wave resonances at low frequencies. The blue crosses predict the internal gravity mode resonances expected to form within the finite width of the interface (Appendix B), and can be seen to correspond to the additional peaks observed. We expect slightly different frequencies for each of the three steps, however here we plot just one set for clarity.

The surface gravity (f-mode) response is again significant in Figure 5.1c, however is no longer significantly affected by the stably stratified layer. As we can see the shift due to a finite core at $\alpha = 0.1$ (red circle) predicts the location of the peak well, but the adjustment predicted by stratification does not, due to its neglect of the convective region from βr_0 to r_0.

5.1.1 Travelling wave regime

To aid understanding of our numerical results we first consider an analytical limit of our model. We assume that the damping mechanism is sufficiently efficient that a wave propagating inwards is fully damped before reflecting from the core and forming a standing wave. Therefore, we can assume that all the energy from the wave is dissipated into the system and equate the inward travelling energy flux with the total tidal dissipation rate. In this model our damping mechanism is kinematic viscosity, and thermal diffusivity and therefore this regime applies to low frequency waves which have sufficiently short wavelengths.

For this approximation to hold, we consider frequencies for which the damping timescale is shorter than the group travel time. Full mathematical details

$\bar{N}$ $\nu = \kappa$	0.1	1	5
10^{-2}	0.128	0.717	2.40
10^{-4}	0.0403	0.227	0.758
10^{-6}	0.0128	0.0717	0.234
10^{-8}	0.00403	0.0227	0.0758

Table 5.1: The critical frequency ω_{crit} approximately below which the travelling wave approximation is valid, for different damping rates (ν, κ) and stratifications $(\bar{N})$, and $\alpha = 0.1$, $\beta = 1.0$. The values have been calculated with equation 5.1.

of the calculation are found in Appendix D, where the critical frequency is found to be approximately

$$\omega_{crit} = \left((1-\alpha) r_0 (\nu + \kappa)(N k_\perp)^3\right)^{\frac{1}{4}}. \tag{5.1}$$

For reference, the critical frequencies for some parameter values are shown in Table 5.1. Although we are only considering low frequencies, this regime is potentially relevant for planetary applications if the forcing frequency is sufficiently low compared with the dynamical frequency of the planet, provided the waves are fully damped. As this calculation is independent of the damping mechanism it therefore holds when considering other mechanisms such as wave breaking or critical layer absorption, provided complete absorption has also occurred (Barker & Ogilvie, 2010; Su et al., 2020).

Figure 5.4a shows the radial dependence of the solution at a forcing frequency of $\omega = 0.05$ for various different viscosity and thermal diffusivity values, with other parameters kept fixed at $\alpha = 0.1$, $\beta = 1$, $\bar{N} = 1$ and $Pr = 1$. We can see that as the viscosity increases, as well as altering the wavelength of the solution (see Section 5.2.3), the depth within the planet that the wave propagates to before being absorbed is decreased. We see that for both the $\nu = 10^{-2}$ (black solid) and $\nu = 10^{-4}$ (red-dashed) cases, which are well below the critical frequency at which the waves are absorbed before reaching the inner boundary. For the $\nu = 10^{-4}$ (blue-dotted) case where we are approaching the critical frequency the wave propagates

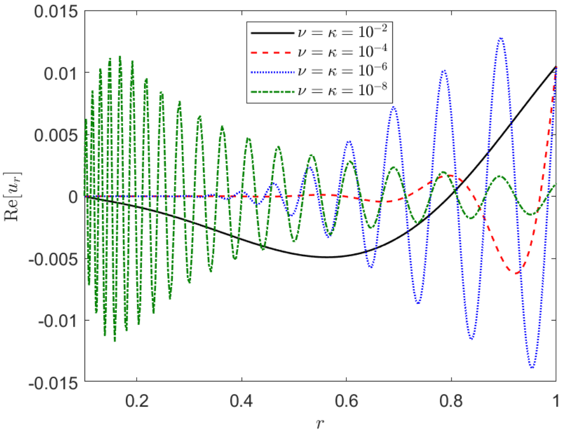

(a) Radial dependence of forced solution to illustrate the propagation depth and critical frequency, for $\alpha = 0.1$, $\beta = 1.0$, $\bar{N} = 1$, $\omega = 0.05$.

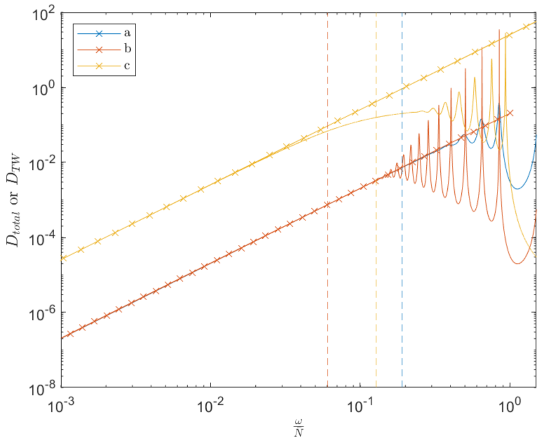

(b) Total dissipation for analytical travelling wave calculation (crosses and straight lines) and numerical result (solid line). Vertical lines show the critical frequency given by equation 5.1.

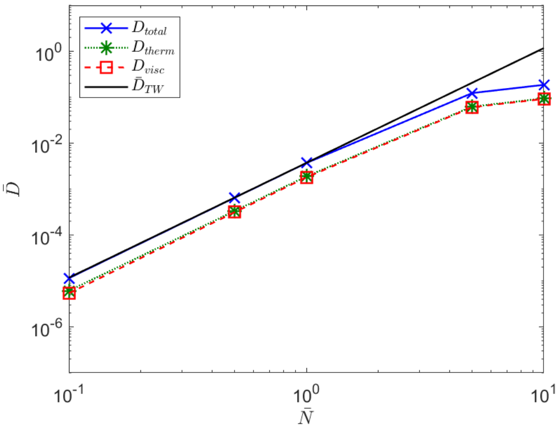

(c) Comparison of the analytical travelling wave calculation and the numerical frequency-averaged dissipation using $\omega_{max} = \omega_{crit}$.

Figure 5.4: Comparison of the travelling wave calculations and numerical results, for all cases $\alpha = 0.1$, $\beta = 1$ and in Panel c $\nu = \kappa = 10^{-4}$.

most of the way through the interior. Finally in the $\nu = 10^{-8}$ (green dot-dashed) case we are above the critical frequency and the wave behaviour extends throughout the entire domain.

As complete wave absorption has occurred, we only need to consider the inwardly travelling component of the wave solution, setting the outward coefficient to be identically zero. This allows us to calculate the total energy flux in the wave and equate it to the total dissipation. Full mathematical details of the calculation are found in Appendix D, where we show that if $\beta = 1$, the total dissipation is described by

$$D_{TW} = \frac{|\psi_0|^2 r_0^5 \bar{N} \omega^2}{2\sqrt{l(l+1)}}. \tag{5.2}$$

Figure 5.4b shows the analytical dissipation as described by equation 5.2, compared to numerical results for three cases. All three cases have $\alpha = 0.1$, $\beta = 1$, and the blue, red and yellow lines are for $\bar{N} = 1$ and $\nu = \kappa = 10^{-4}$, $\bar{N} = 1$ and $\nu = \kappa = 10^{-6}$, and $\bar{N} = 5$ and $\nu = \kappa = 10^{-4}$, respectively. We can see when comparing at low frequencies there is particularly good quantitative agreement between the travelling wave calculation (crosses) and numerical results (solid lines), where both follow a clear ω^2 trend with the same slope. The dashed lines indicate the critical frequencies below which this approximation would be valid, and we can see that this estimation approximately holds.

At sufficiently low frequencies we observe no dependence on viscosity or thermal diffusivity as both the blue and red lines agree. As we assume the wave is fully damped, the timescale over which dissipation occurs is not then significant. By comparing the blue and yellow lines, we can see that there is a linear dependence on $\bar{N}$, showing the strength of the stable stratification does play an important role in the magnitude of dissipation.

In Appendix D we also find the frequency-averaged travelling wave dissipation defined by equation 4.47. When we take limits of $\omega_{min} = 0$ and

$\omega_{max} = \bar{N}$, it is found that

$$\bar{D}_{TW} = \frac{|\psi_0|^2 r_0^5 \bar{N}^3}{4\sqrt{l(l+1)}}, \tag{5.3}$$

and when we take $\omega_{max} = \omega_{crit}$ and $\omega_{min} = 0$, we find

$$\bar{D}_{TW} = \frac{|\psi_0|^2 r_0^5 \bar{N}^{\frac{5}{2}} (\beta - \alpha)^{\frac{1}{2}} (\nu + \kappa)^{\frac{1}{2}} (l(l+1))^{\frac{1}{4}}}{4}. \tag{5.4}$$

We compare the travelling wave frequency-average dissipation to the numerically equivalent calculation, using ω_{crit} as our upper integration bound in both cases. Figure 5.4c shows that the numerical calculation agrees well with the travelling wave approximation, where we have $\alpha = 0.1$, $\beta = 1$, $\nu = \kappa = 10^{-4}$ and we vary $\bar{N}$. We can see that for small values the agreement is almost exact, and only begins to deviate for $\bar{N} > 1$. This agrees with the departure between analytical and numerical results seen in Figure 5.4b, and is a result of the relevant damping per wavelength decreasing as we increase $\bar{N}$, to be discussed further in Section 5.2.1.

5.2 Parameter dependences for uniform stable stratification

Moving on, we now consider how the key parameters in our model alter the expected viscous, thermal and total dissipation, by varying each parameter in turn. For reference, Table 5.2 has been created to give some astrophysical context to the parameters explored.

5.2.1 Varying the strength of the stable stratification

Perhaps the most important parameter when considering stable stratification is the buoyancy frequency, $\bar{N}$, which is a measure of the strength of the stratification as it dictates the density/entropy gradient. Planetary evolution models and observations

Planet	Buoyancy Frequency			Dilute Core Size			Viscosity			Prandtl Number	
Units	s^{-1}	ω_d^{-1}	Reference	km	r_0	Reference	$m^2 s^{-1}$	$\frac{\nu}{r_0^2 \omega_d}$	Reference		Reference
Jupiter				34956	~ 0.5	Wahl et al. (2017)	3×10^{-7} to 10^{-5}	1×10^{-13} to 3×10^{-12}	Guillot et al. (2004)	10^{-4} to 10^{-1}	Guillot et al. (2004)
				48938	~ 0.7	Debras & Chabrier (2019)					
Saturn	0 to 8.8×10^{-4}	0 to 2	Mankovich & Fuller (2021)	34939	~ 0.6	Mankovich & Fuller (2021)					
	0 to 8.8×10^{-4}	0 to 2	Fuller (2014)	23293	~ 0.4	Fuller (2014)					
Neptune				17336	~ 0.4	Bailey & Stevenson (2021)					

Table 5.2: Estimates for parameters in Jupiter and Saturn, in SI units and the non-dimensional units used in this study. Data taken from various sources spanning different techniques.

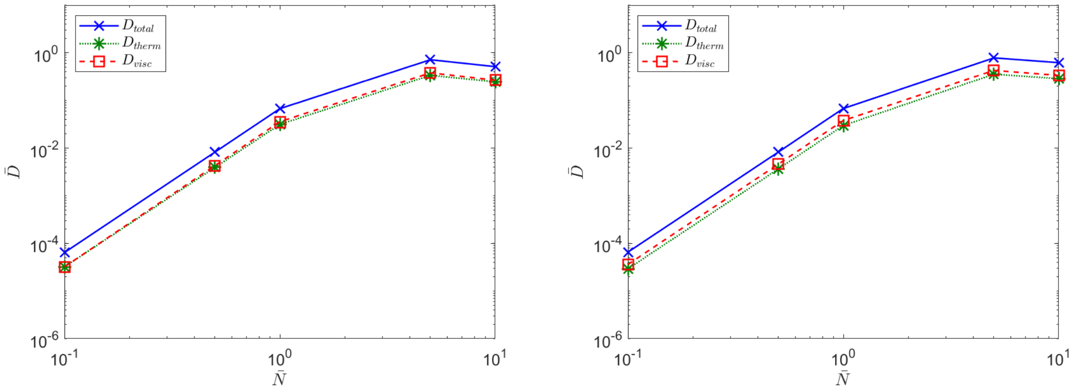

(a) $\nu = \kappa = 10^{-4}$ (b) $\nu = \kappa = 10^{-6}$

Figure 5.5: Frequency-averaged dissipation as a function of stratification strength $\bar{N}$ for two different viscosities and thermal diffusivities. In both cases $\omega_{max} = \bar{N}$ and $\alpha = 0.1$, $\beta = 1.0$.

give a range of results for the properties of the stable stratification, therefore here we explore what implications different values could have, using the values in Table 5.2 to motivate our parameter surveys.

Figure 5.5 shows the frequency-averaged dissipation as a function of $\bar{N}$ showing the viscous $\bar{D}_{visc}$, thermal $\bar{D}_{ther}$, and total $\bar{D}_{total}$ frequency-averages, where integration limits have been taken as $\omega_{min} = 0$ and $\omega_{max} = \bar{N}$. In both cases we are considering a uniform stable stratification extending to the planetary radius, therefore $\alpha = 0.1$ and $\beta = 1$, however we consider two different values for the viscosity and thermal diffusivity, such that Figure 5.5a is for the case $\nu = \kappa = 10^{-4}$ and Figure 5.5b for $\nu = \kappa = 10^{-6}$. At this stage we simply note the similarity between the two plots and discuss them concurrently, expanding on the similarities further in Section 5.2.3. There is a clear $\bar{N}^3$ dependence when $\bar{N} < 1$, which agrees with the analytical travelling wave calculation given by equation 5.3 discussed previously. This holds despite the change in the limit used for ω_{max}, as in this case we have integrated beyond the critical frequency so would not necessarily expect complete agreement. We note that the same trend is exhibited in both the thermal and viscous dissipation as the resonant waves dissipate through both mechanisms.

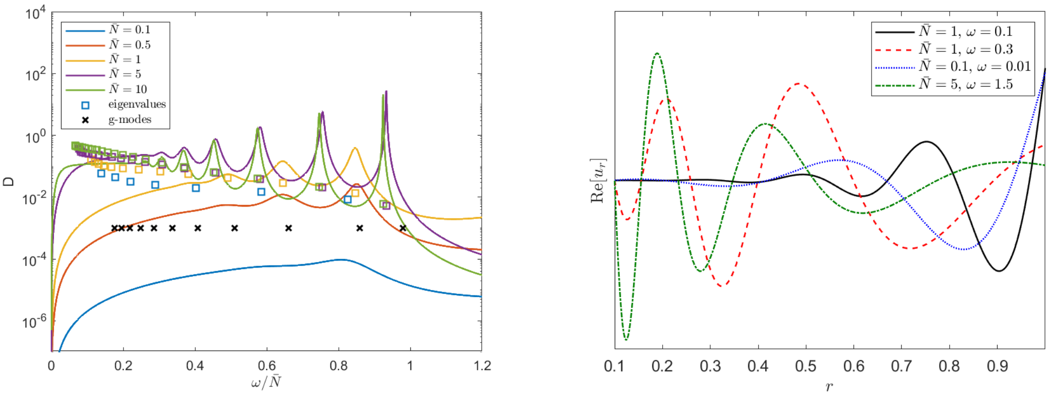

(a) $\nu = \kappa = 10^{-4}$ (b) $\nu = \kappa = 10^{-4}$

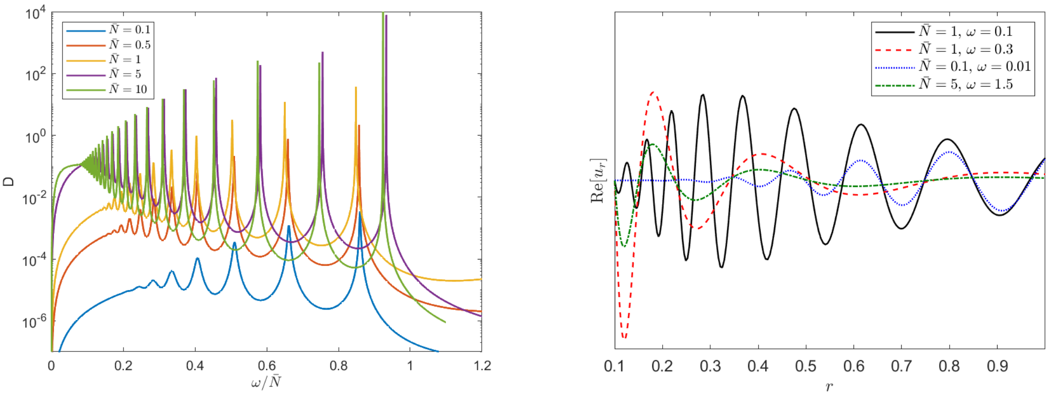

(c) $\nu = \kappa = 10^{-6}$ (d) $\nu = \kappa = 10^{-6}$

Figure 5.6: Panels a and c show dissipation rate as a function of frequency for different magnitudes of uniform stable stratification. Panels b and d show the radial dependence of u_r for the given parameters. Note the y−axis has been scaled for illustrative purposes, $(\bar{N} = 1, \omega = 0.1) \times 50$, $(\bar{N} = 1, \omega = 0.3) \times 5$, $(\bar{N} = 0.1, \omega = 0.01) \times 500$.

Figures 5.6a and 5.6c show the frequency dependence of dissipation for the cases, which when integrated, give the data for the frequency-averaged values shown in Figures 5.5a and 5.5b respectively. The x-axis has been scaled by $\bar{N}$ in these figures to allow for easy comparison. We can clearly see the characteristic g-mode peaks that appear at a similar location in $\frac{\omega}{\bar{N}}$ in each case. The first mode, located just below $\bar{N}$, contains one node in radius, therefore the wavelength is equal to the layer depth. Following on from this, additional lower frequency modes correspond to waves with additional nodes, which have lower frequencies and shorter wavelengths. These exist as an infinite set of nodes, see equation B.17, however the first 10 have been plotted in this case. The frequency of the internal gravity modes obtained analytically is linear in $\bar{N}$, therefore when plotting on the $\frac{\omega}{\bar{N}}$

axis the predictions lie on top of one another. The modes of the full system clearly have a dependence on $\bar{N}$, and roughly speaking the $\bar{N} < 1$ trends deviate more than $\bar{N} > 1$ cases. There are several factors in balance here; the effect of neglecting viscosity and thermal diffusivity is more prevalent at low frequencies and low $\bar{N}$, and the effect of the free surface is more prevalent at frequencies comparable with ω_d and large $\bar{N}$. It is the balance between these opposing effects that gives the non-obvious dependence in accuracy.

As $\bar{N}$ increases, more resonances are visible as clear peaks and the modes appear to be narrower and sharper. Though this is initially counter-intuitive, as the eigenvalue solutions, shown by the squares with the corresponding colour, show that the damping rate increases with $\bar{N}$, it can be explained by considering the relevant time scales. If we consider the ratio of the group travel time to the damping time, we find the following,

$$\frac{t_g}{t_d} = \frac{2(\beta-\alpha)r_0k_r^2}{k_\perp \bar{N}} \div \frac{2}{(\nu+\kappa)k_r^2} = \frac{(\nu+\kappa)(\beta-\alpha)r_0}{\bar{N}}\frac{k_r^4}{k_\perp}. \tag{5.5}$$

We can see that this ratio is linearly dependent on $\bar{N}$ and therefore despite the overall damping rate ($\propto \ t_d^{-1}$) increasing the “damping per wave crossing time" decreases which leads to sharper and narrower peaks.

Figures 5.6b and 5.6d show the forced solution for u_r as a function of r for different frequencies and stratification strengths, but note the y-axis has been scaled so all examples can be viewed on one plot. All the cases shown are examples of internal gravity (g-mode) waves as shown in Figure 5.2a. Both the wavelength and amplitude of the solutions are strongly dependent on the forcing frequency and stratification. The amplitude (not shown on these plots), depends on how close the forcing frequency is to a resonance, where we note that dissipation is proportional to amplitude squared.

By comparing the solid black ($\bar{N} = 1, \omega = 0.1$) and red-dashed ($\bar{N} = 1$, $\omega = 0.3$) lines we can see that decreasing the forcing frequency (i.e. ratio of $\frac{\omega}{\bar{N}}$), decreases the wavelength. Each peak in dissipation corresponds to a resonance

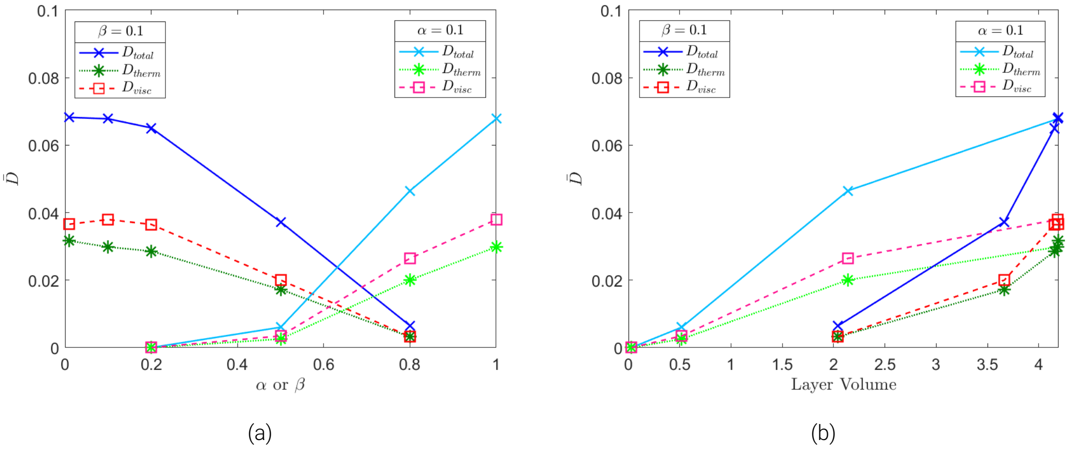

Figure 5.7: Frequency-averaged dissipation as a function of stratified layer size α and β. In both cases $\omega_{max} = \bar{N}$ and other parameters are fixed, $\bar{N} = 1, \nu = \kappa = 10^{-6}$.

where a multiple of half-integer wavelengths fit within the stratified layer. This relationship can be more clearly seen in the $\nu = \kappa = 10^{-6}$ case as the frequencies shown are both well above the critical frequency ($\omega_{crit} = 0.072$). By comparing the black solid line ($\bar{N} = 1, \omega = 0.1$) with the blue-dotted line ($\bar{N} = 0.1, \omega = 0.01$) and the red-dashed line ($\bar{N} = 1, \omega = 0.3$) with the green dot-dashed line ($\bar{N} = 5, \omega = 1.5$) we can see that the wavelengths are roughly comparable for the same $\frac{\omega}{\bar{N}}$. Again, proximity to the critical frequency affects the robustness of this result.

5.2.2 Varying the size of the stably stratified layer

As we have outlined in Chapter 1, in realistic planetary models we expect the stable stratification would not extend all the way to the planetary radius but sit below a convective region. It is therefore informative to consider the consequences of varying the radius of the stratified layer. We now consider a buoyancy frequency as described in equation 4.41 with $\beta \neq 1$. As our numerical model requires a finite size solid core for regularity of the solutions, we must consider a non-zero inner core size αr_0, therefore, along with β, we explore how this parameter alters the results.

Figure 5.7a shows how the frequency-averaged dissipation varies with α and β, for $\bar{N} = 1, \nu = \kappa = 10^{-6}$. Figure 5.7b shows the same parameter values but in

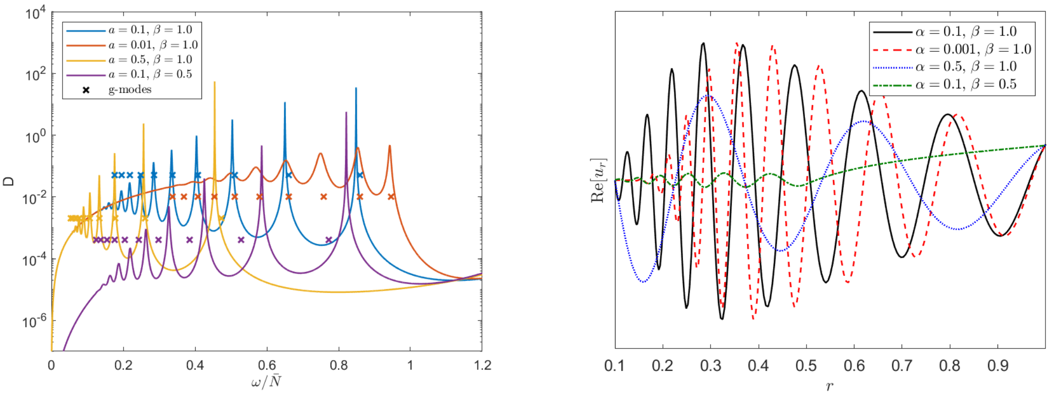

(a)

(b)

Figure 5.8: Panel a shows total dissipation rate as a function of frequency for various α and β values. Panel b shows the radial dependence of the u_r for given parameters.

this case we have calculated the corresponding volume of the stratified layer for each pair of α and β values. The darker coloured lines show the dependence on α for a fixed $\beta = 1.0$, and the lighter lines show the dependence on β for fixed $\alpha = 0.1$. When fitted, the β dependence is roughly $\bar{D} \propto \beta^5$, which we note is the same as the dependence on r_0 found in the travelling approximation when considering $\beta = 1$, see equation 5.2. It is clear from Figure 5.7b that there is a strong volume effect, for which total dissipation decreases as the volume of the stratified layer decreases. However as these results found in Figure 5.7b do not show a strictly linear relationship, there are additional dependencies on α and β that are independent of the volume of the layer.

This result is due to a combination of factors altering the amplitude of the forced response, which can be related to the rate of dissipation. Firstly, the waves are launched from the outer edge of the stratified layer at βr_0 and propagate inwards. The initial amplitude of the forced wave depends on this radius and decreases as β decreases. However in the case of a standing wave the amplitude increases as the wave propagates inwards, leading to larger rates of dissipation close to the inner core.

The frequencies of the internal gravity modes depend strongly on α and β. This is expected as the resonant frequencies depend on the half-integer wavelengths that fit inside the stratified layer, as shown by equation B.17. The solutions for a forcing frequency of $\omega = 0.1$ are shown in Figure 5.8b, where the differences in wavelength are clear. The green-dashed line shows the case where the stratified layer only extends to half the planetary radius, where the wavelike behaviour can be seen to be confined to the stratified region and not persist in the convective region, in which the solution is evanescent.

5.2.3 Varying viscosity, thermal diffusivity and Prandtl number

The interiors of giant planets are, like most astrophysical fluids, expected to consist of regions of low viscosity, thermal diffusivity and Prandtl number, as we indicate in Table 5.2. It is often numerically unrealistic to carry out studies in this parameter regime as the time and length scales required to be resolved are extremely small. For the purposes of our calculations, this means we would require very high radial resolution to resolve tidally forced waves with realistic planetary properties. Therefore, studies like ours must focus on parameter values that are more numerically achievable. In this section we also consider numerically convenient values, which allows us to explore the likely trends in dissipation rates.

Initially we consider cases with a constant Prandtl number, while varying viscosity ν, and thermal diffusivity κ, simultaneously. In Figure 5.9a for which $\alpha = 0.1$, $\beta = 1.0$, $\bar{N} = 1$ we can see that the frequency averaged dissipation has little dependence on viscosity and thermal diffusivity. This is a useful result when considering average trends for planetary applications, since realistic parameters are likely to be far from those considered here. This means that the overall frequency-averaged dissipative properties are insensitive to diffusivities, even if the dissipation at a given frequency is strongly dependent on these values.

This can be explained by considering the low-frequency and mid-frequency regimes separately. For frequencies sufficiently low that the travelling wave approximation is valid (see Section 5.1.1), the result is found to be independent

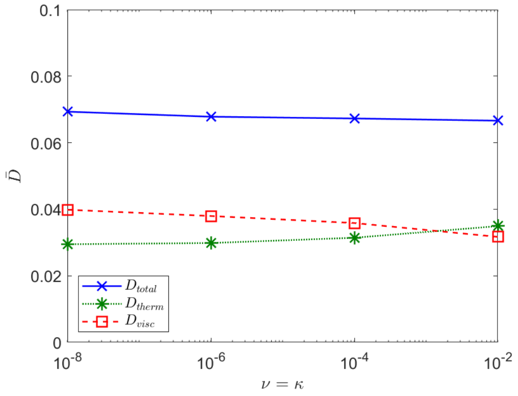

(a) $Pr = 1$

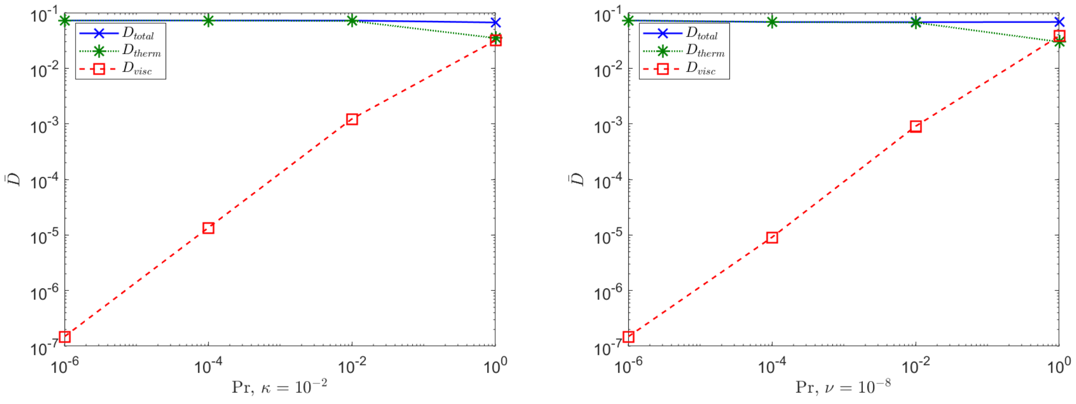

(b) $\kappa = 10^{-2}$ (c) $\nu = 10^{-8}$

Figure 5.9: Frequency-averaged dissipation as a function of viscosity, thermal diffusivity and Prandtl number, for $\alpha = 0.1$, $\beta = 1.0$, $\bar{N} = 1$. In all cases $\omega_{max} = \bar{N}$.

of damping mechanism and therefore each of ν, κ and Pr. To consider the mid-frequency range where resonant peaks are clear, we refer back to the analogy of a forced damped harmonic oscillator discussed in section 4.6. There we established that the width of the peak was proportional to the damping rate, and the height of the peak inversely proportional to the damping rate. Therefore, upon integration, they have counteracting effects in the frequency-averaged dissipation, this is confirmed in Figure 5.10a, where these effect are visible. Although the point at which we transition into the travelling wave regime varies considerably, see Table 5.1, this has no effect on the overall results.

In Figure 5.10a we also observe that the effect of viscosity on the frequency of the internal gravity modes is very small, in fact the dependence is not observable on the scale of these plots. Instead, the mode frequency is strongly dependent on

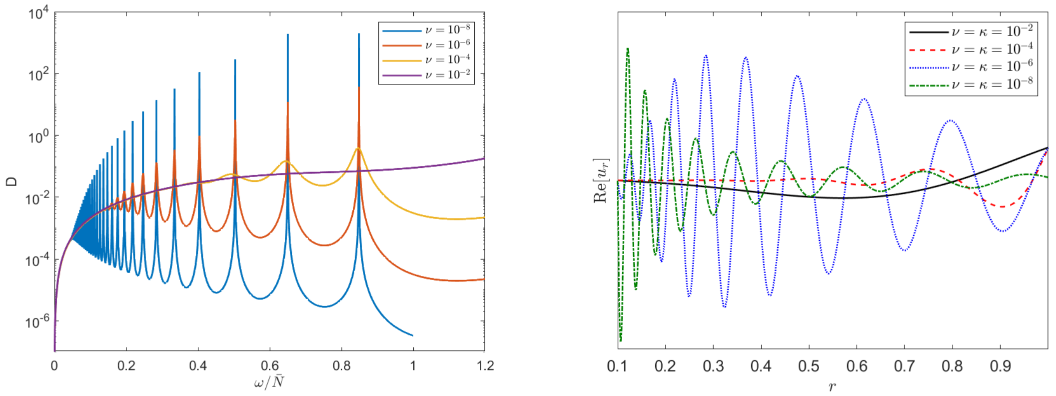

(a) D_{total}

(b) $\omega = 0.1$

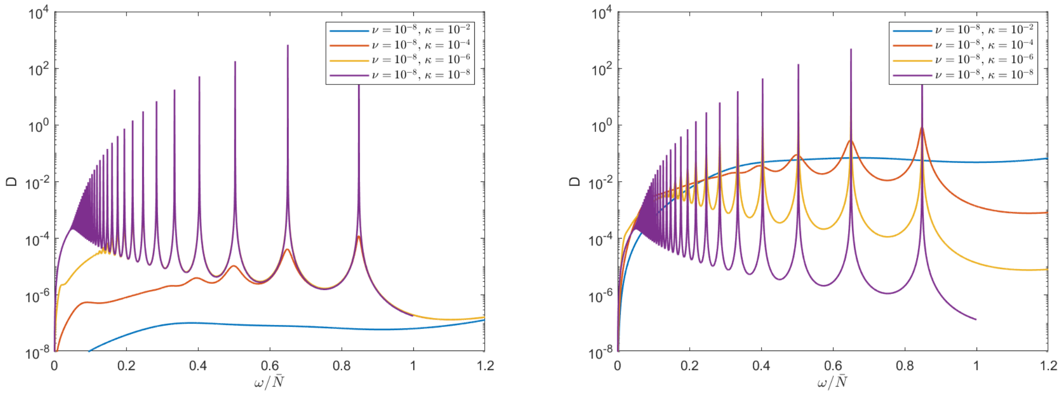

(c) Viscous dissipation

(d) Thermal dissipation

Figure 5.10: Panel a shows total dissipation as a function of frequency for different viscosities and thermal diffusivities with $Pr = 1$. Panel b shows the radial dependence of u_r at forcing frequency of $\omega = 0.1$ for the given parameters. Panels c and d show the viscous and thermal dissipation, respectively, for $\nu = 10^{-8}$.

the location and strength of the stable stratification, which is kept constant across these cases.

Figure 5.10b shows the radial dependence of u_r at a tidal forcing frequency of $\omega = 0.1$ for different viscosities and thermal diffusivities with a fixed Prandtl number $Pr = 1$. At this tidal forcing frequency we are below the regime in which a discrete set of resonances are visible at all but the lowest viscosity, and it is clear in the case of the largest viscosity that we are in the travelling wave regime. We observe that, although the integrated dissipation is independent of viscosity, the spatial structure of the response, like the frequency dependent dissipation, is sensitive to viscosity and thermal diffusivity.

Turning our attention now to varying the Prandtl number, Figure 5.9b and 5.9c show the frequency-averaged dissipation as a function of Prandtl number. We consider two cases, one of fixed viscosity $\nu = 10^{-8}$, and the other fixed thermal diffusivity $\kappa = 10^{-2}$, both cases again fix $\alpha = 0.1$, $\beta = 1.0$ and $\bar{N} = 1$ as before. We find the integrated dissipation D_{total} has very little dependence on Prandtl number and the main consequence of decreasing Prandtl number is the subsequent decrease in the ratio of D_{visc} to D_{ther}; we also note the similarity between the figures despite the significant variation in total diffusivity $\nu+\kappa$. Looking at the frequency dependence in Figures 5.10c and 5.10d, we see the width and height of the resonant peaks also exhibit the expected behaviour similar to the forced damped harmonic oscillator.

5.3 Parameter dependences for semi-convective layers

As it is possible that stratified layers in giant planets could be unstable to double-diffusive convection, leading to the presence of staircase-like density structures, we now consider how semi-convective layers can alter the measured dissipation. Instead of a uniformly stratified medium, we now consider a series of convective steps with stably stratified interfaces, as described by equations 4.43, which have an equivalent mean stratification to a uniformly stratified layer of equal depth.

5.3.1 Convergence with step number

Shown in Figures 5.11a and 5.11b is the frequency-averaged dissipation as a function of step number for cases in which the staircase extends across the entire depth of the planet. In both cases we fix $\alpha = 0.1$, $\beta = 1$, $\bar{N} = 1$ and $\nu = \kappa = 10^{-6}$, but in Figure 5.11a the width of each interface is fixed, and in Figure 5.11b the total width of all interfaces is fixed with the height of the peaks adjusted accordingly.

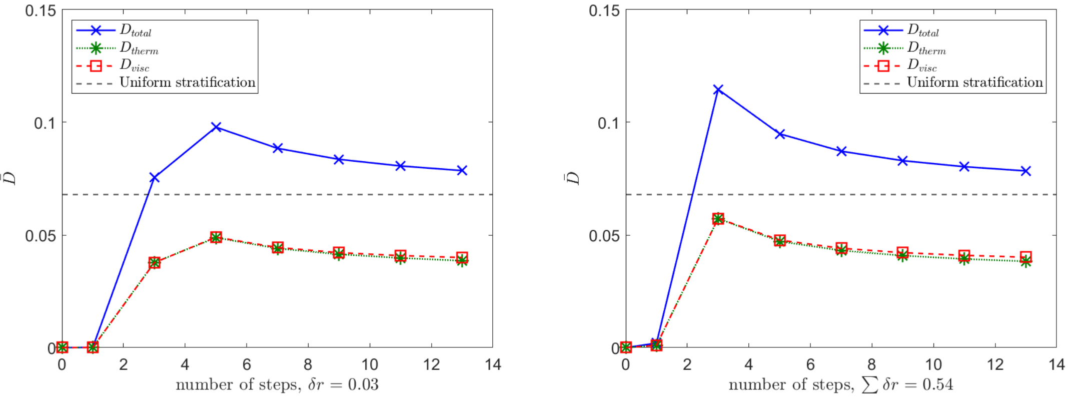

(a) Fixed step width, $\delta r = 0.03$ (b) Fixed total step width, $\sum \delta r = 0.54$

Figure 5.11: Frequency-averaged dissipation as a function of the number of steps in a staircase, for $\alpha = 0.1$, $\beta = 1.0$, $\bar{N} = 1$, $\nu = \kappa = 10^{-6}$.

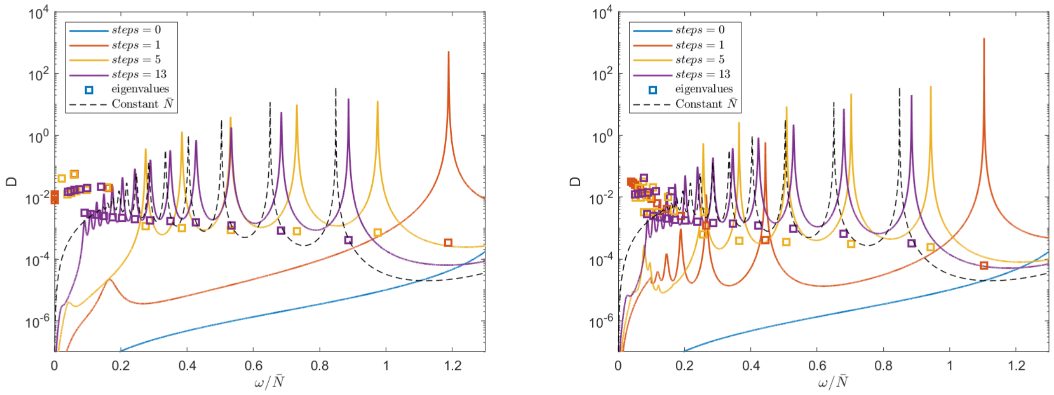

(a) $\delta r = 0.03$ (b) $\sum \delta r = 0.54$

Figure 5.12: Dissipation as a function of frequency for different numbers of steps with fixed $\alpha = 0.1$, $\beta = 1.0$, $\bar{N} = 1$, $\nu = \kappa = 10^{-6}$. Panel a shows the case for fixed step width $\delta r = 0.03$. Panel b shows the case for fixed total step width $\sum \delta r = 0.54$.

Although it is likely that a staircase structure does not extend all the way to the planetary surface, we have considered $\beta = 1$ in these cases to reduce the required radial resolution, allowing us to consider cases with a higher step number whilst keeping numerical demand low. In both cases the total dissipation $\bar{D}_{total}$ for the equivalent uniformly stratified case has been plotted (black-dashed line).

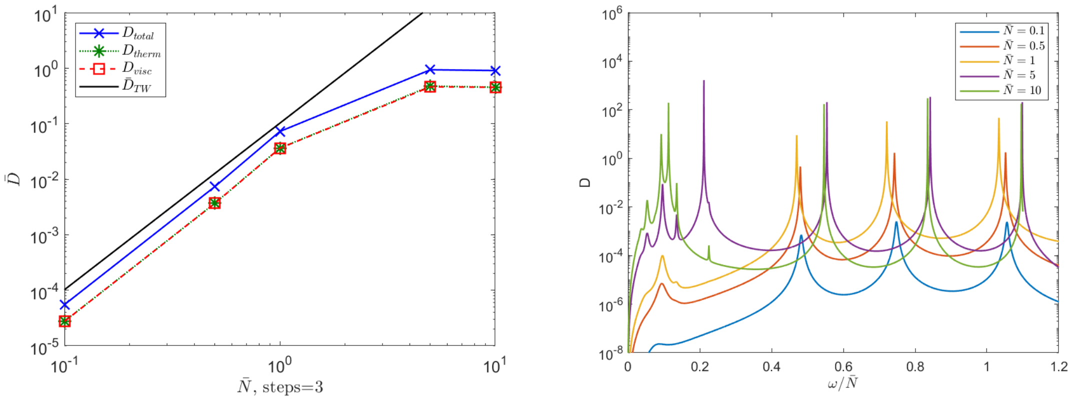

(a) Varying $\bar{N}$ with fixed $\nu = \kappa = 10^{-6}$, steps$= 3$

(b) Varying $\bar{N}$ with fixed $\nu = \kappa = 10^{-6}$, steps$= 3$

Figure 5.13: Panel a shows the frequency-averaged dissipation as a function of stratification strength, $\bar{N}$ for the case of a staircase-like density structure with other parameters fixed at $\alpha = 0.1$, $\beta = 1.0$, steps $= 3$, $\delta r = 0.06$, $\nu = \kappa = 10^{-6}$. Panel b shows the corresponding frequency dependence.

Although for very low step numbers these cases exhibit slightly different trends, where the total dissipation is larger than that of a uniformly stratified layer, the total frequency-averaged dissipation very quickly converges to that of the uniform stratified layer. There is large uncertainty in the number of steps that could form, and it is likely to evolve with time as they merge (Belyaev et al., 2015; Wood et al., 2013); however this suggests unless there are very few layers in the system the staircase will act similarly to a uniformly stratified medium, although it will depend of the frequency on the tidal forcing.

The frequency dependence of the dissipation profiles for different step numbers is shown in Figures 5.12a and 5.12b for fixed step width and fixed total step width respectively. We see additional peaks arising with increasing step number and observe low frequency internal gravity mode resonances at low frequencies. These short wavelength modes have formed within the finite width of the interfaces, in the case of a fixed step size they occur for $\omega < 0.2$, and have little contribution to the frequency-averaged dissipation. However, in the case of fixed total step width they occur at much higher frequencies ($\omega < 0.5$ in steps $= 1$ case). This is due to the large interface width in the case of a single layer, allowing for internal gravity waves with comparably large wavelengths to form.

5.3.2 Varying the strength of the staircase stratification

As we did for the uniformly stratified case, we consider how the frequency-averaged dissipation rate depends on the strength of the stratification in Figure 5.13a. We see that the trend found in Section 5.2.1, and the agreement with the travelling wave calculation, holds here also as the staircase-like structure behaves like a uniform medium. This suggest that the results from this calculation could be useful in this case also and looking at the dissipation profile in Figure 5.13b, we can see the same narrowing of peaks as stratification strength increases. The notable difference between these cases is the behaviour of the g-modes forming within the interfaces. The resonances with these modes can be seen to increase significantly with stratification, and in fact even with only moderate stratification ($\bar{N} = 5$) they have a magnitude comparable to that of the interfacial modes, and therefore contribute significantly to the frequency-averaged dissipation.

5.4 Isolated stable layer - Helium rain layer

Having explored a stable layer just outside the core, we now consider an isolated stable layer near the transition region between the metallic and molecular regions, potentially caused by Helium rain, see Chapter 1. We use equation 4.43 to describe a single wide step ($\delta r = 0.1$) to represent an isolated transition layer. In Figure 5.15a we show total dissipation (D_{total}) for cases where $\bar{N} = 1$, $\nu = \kappa = 10^{-6}$, and $\alpha = 0.1$. The location of the wide interface is varied using β, which here represents the centre of the layer. We see the large surface gravity resonance about $\omega = 1.6$, the single interfacial mode (where the layer oscillates as an interface) between $\omega = 0.6$ and $\omega = 1.5$, and a series of shorter wavelength internal gravity mode resonances at low frequencies.

There are two things to note in this figure. First, the frequency of the interfacial mode depends strongly on the location of the layer β, which could have consequences when considering observations of mode-mixing or the possibility of resonance-locking (Fuller, 2014; Fuller et al., 2016; Dewberry et al., 2021). Second,

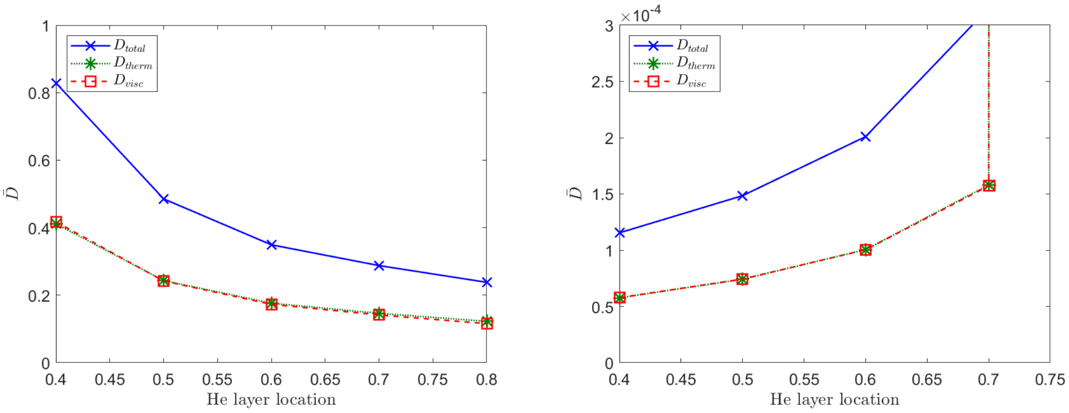

(a) $\omega_{min} = 0, \omega_{max} = 2$

(b) $\omega_{min} = 0, \omega_{max} = 0.6$

Figure 5.14: Frequency-averaged dissipation as a function of Helium layer location for cases with $\alpha = 0.1, \bar{N} = 1, \delta r = 0.1, \nu = \kappa = 10^{-6}$.

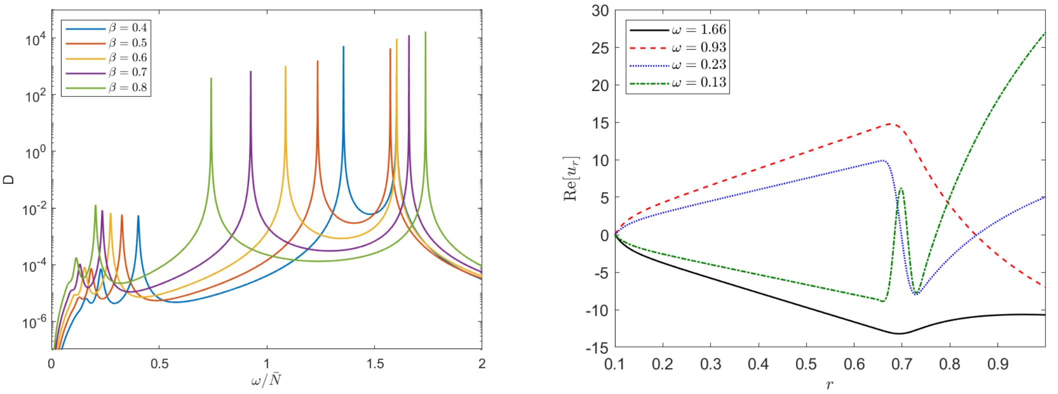

(a) $\alpha = 0.1, \bar{N} = 1, \delta r = 0.1, \nu = \kappa = 10^{-6}$

(b) $\alpha = 0.1, \bar{N} = 1, \delta r = 0.1, \nu = \kappa = 10^{-6}, \beta = 0.7$

Figure 5.15: Panel a shows dissipation as a function of frequency for an isolated stable layer at different radii. Panel b shows the radial dependence of the forced solution at different frequencies.

the amplitude of the interfacial and surface gravity mode peaks decrease in height as the layer moves outwards whilst the internal gravity waves peaks increase in magnitude. Figure 5.14 shows the frequency-averaged dissipation, and we can see in panel a where the upper frequency limit has been taken to be $\omega_{max} = 2$, that dissipation decreases as the layer is moved outwards. However, in panel b we take $\omega_{max} = 0.6$ so that the integrated quantity only includes the internal gravity wave resonances within the step, there is a increase in dissipation. Therefore, the importance and consequences of an isolated stably stratified layer depends on whether the forcing frequency is close to the interfacial mode resonance or the internal gravity mode resonances.

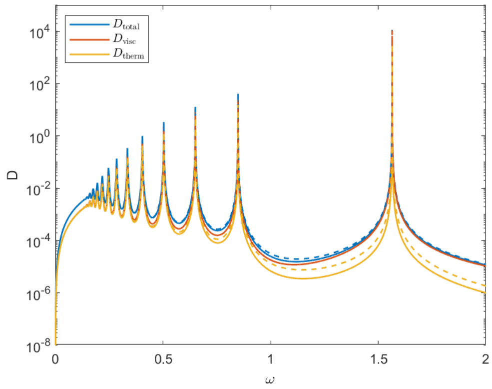

(a)

Figure 5.16: Dissipation rates for a case considering the gravity profile of a dense core. Parameter values are $\alpha = 0.1$, $\beta = 1.0$, $\bar{N} = 1$, $\nu = \kappa = 10^{-6}$. The solid lines show results for $g \propto \frac{1}{r^2}$ and the dashed lines $g \propto r$ for comparison.

5.5 Gravity profile for a dense core with $g \propto 1/r^2$

So far in this thesis we have considered a gravity profile suitable for a homogeneous body where $g \propto r$. We do not expect a planet to be a homogeneous body and therefore consider how changing this profile to consider the gravity field of a centrally condensed body affects our results. To do this, we consider $g \propto \frac{1}{r^2}$, which results in the following governing equations, but note that the surface gravity g_0 is still 1,

$$\frac{\partial \boldsymbol{u}}{\partial t} = -\frac{1}{\rho_0}\nabla p + \frac{b}{r^2}\hat{r} + \nu \nabla^2 \boldsymbol{u} - \nabla \psi, \tag{5.6}$$

$$\frac{\partial b}{\partial t} + r^2 u_r N^2 = \kappa \nabla^2 b, \tag{5.7}$$

with similar changes in the boundary conditions and dissipation calculations. We note that the buoyancy force and gravity term appear on their own, in the same term in equation 5.6, and in the absence of thermal diffusivity, equation 5.7 could be rearranged similarly. This results in an identical calculation for the analytical prediction of free modes, and the differences in the forced response arise solely in the buoyancy variable directly affecting thermal dissipation only. Hence, we expect the dissipative responses to be very similar for both gravity profiles.

Our numerical results have confirmed this and we found that changing the gravity profile did not significantly alter our conclusions. As expected the resultant velocity, and in turn, the viscous dissipation remained unchanged and only the thermal dissipation varies. Figure 5.16a shows the total, viscous and thermal dissipation rates with the gravity profile of a dense core (solid line) compared with that of a homogeneous body (dashed line), where we note only minor quantitative differences.

5.6 Comparison to realistic values and observed tidal quality factors

Here we have discussed a simplified model and the values for tidal dissipation rates found here should not be taken too far out of this context. However, it is still informative to consider the extrapolation of our results to compute tidal quality factors to appreciate the astrophysical significance of our results. Following Ogilvie (2014), the total tidal dissipation rate can be related to the dimensionless complex Love number by

$$D = |\omega| \frac{(2l+1)r_0|\mathcal{A}|^2}{8\pi G} \mathrm{Im}[k_l^m(\omega)]. \tag{5.8}$$

Therefore considering for a homogeneous fluid body that $\mathrm{Im}[k_2^m(\omega)] = \frac{3}{2Q'}$ and $\mathcal{A} = \psi_0 r_0^2$, we can write,

$$Q' = |\omega| \frac{(2l+1)r_0^3|\psi_0|^2}{8\pi G} \frac{3}{2D}. \tag{5.9}$$

Therefore, using the non-dimensionalisation used previously, noting that $G = 1$ in our units, the tidal quality factor can be written in terms of our variables as,

$$Q' = |\omega| \frac{(2l+1)|\psi_0|^2}{8\pi} \frac{3}{2D}. \tag{5.10}$$

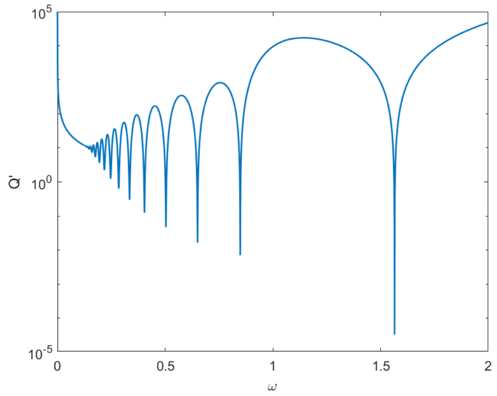

Figure 5.17: Tidal quality factor for the case shown in Figure 5.1a, with parameters, $\alpha = 0.1$, $\beta = 1.0$, $\bar{N} = 1$, $\nu = \kappa = 10^{-6}$.

We note that as we have considered the linear problem, $D \propto \psi_0^2$ and therefore Q' is independent of tidal amplitude. Setting $l = 2$ and $|\psi_0| = 1$ as we have considered in our numerical results, we find

$$Q' = \frac{15|\omega|}{16\pi D}. \tag{5.11}$$

Therefore, taking our first example of a dissipation profile shown in Figure 5.1a, we can find the frequency-dependent tidal quality factor shown in Figure 5.17.

Using the formula for dissipation found using the travelling wave approximation, equation 5.2, we find,

$$Q' = \frac{30\sqrt{6}}{16\pi}\frac{1}{\bar{N}|\omega|}. \tag{5.12}$$

From this it is possible to calculate quantities such as the circularisation timescale. Taking from Barker (2020) the timescale for circularisation as

$$\tau_e = \frac{2}{63}Q'\left(\frac{M}{M_2}\right)\left(\frac{M+M_2}{M}\right)^{\frac{5}{3}}\frac{P_{orb}^{\frac{13}{3}}}{P_{dyn}^{\frac{10}{3}}}, \tag{5.13}$$

and using some approximate numbers for which we use the values for the hot Jupiter WASP-12b, data taken from Exoplanet.eu (2022), $M = 1.5M_J = 2.8\times10^{27}$kg, $M_2 = 1.4M_\odot = 2.9 \times 10^{30}$kg, $P_{orb} = 1.1$ days, $r_0 = 1.9R_J$, $P_{dyn} = 0.26$ days, and a rough estimation of the tidal quality factor from Figure 5.17 of $Q' = 10^3$. Thus,

$$\tau_e \approx 1.2 \times 10^3 \text{ years}, \tag{5.14}$$

which shows there could be efficient tidal circularisation is possible with the excitation of internal waves.

Similarly we can take from Barker (2020) the calculation for the timescale of orbital migration from initial orbit with semi-major axis a to an orbit with semi-major axis $2a$ due to dissipation inside the planet as,

$$\tau_a = \frac{4}{117}\left(2^{\frac{13}{2}} - 1\right)\frac{Q'}{\Omega_o}\left(\frac{M_2}{M}\right)\left(\frac{a}{R}\right)^5, \tag{5.15}$$

where we have assumed $\Omega_0 \propto a^{-\frac{3}{2}}$ and $Q' \propto \Omega_s$. Using values for Io and Jupiter taken from the Jet Propulsion Laboratory (2022) $M = M_J = 1.90 \times 10^{27}$kg, $M_2 = 8.93 \times 10^{22}$kg, $R = R_J = 6.99 \times 10^4$km, $a = 4.22 \times 10^5$km, $\omega \approx 4.2 \times 10^{-5}$seconds^{-1} and again taking a rough value for tidal quality factor to be $Q' = 10^3$ we find,

$$\tau_a \approx 5.0 \times 10^5 \text{ years}. \tag{5.16}$$

Although such efficient dissipation rates would require large portions of the planet to be stably stratified, this calculation indicates the potential importance of such layers on tidal dissipation rates.

5.7 Conclusion

In this chapter we have used the model outlined in Chapter 4, combining numerical and analytical techniques, to gain understanding of how the tidally forced dissipation depends on some of the parameters in our system, particularly those that dictate the properties of a stably stratified layer. Our numerical calculations allow us to consider the dissipation of internal waves through viscous forces and thermal damping using realistic tidal forcing. We used a numerically smooth profile to represent uniform stably stratified layers that extend to a specified radius or a staircase-like density structure.

As expected from previous studies (e.g. Ogilvie & Lin, 2004; Ogilvie, 2009; André et al., 2019), we observed a strong frequency dependence in the dissipation rate in which there are clear resonances with the modes of the system. In this non-rotating system, when considering uniform stratification we observe internal gravity modes, resonant within the width of the layer. In the case of a staircase-like density profile, we observe interfacial modes as well as short wavelength internal gravity modes that form within the width of the interfaces. In both cases we observe a large resonance with the surface gravity mode. We found good agreement with both the oscillation frequency and damping rate with the eigenvalue problem and analytical calculations of the free modes.

We quantify the dissipation using a frequency-averaged quantity, which allows us to determine overarching trends on the parameters of the system. Using this quantity, we establish that the dissipation rate is proportional to stratification strength $\bar{N}$ and depends on radius of stratification as $\propto \beta^5$. These results agree with the corresponding analytical calculation in the travelling wave regime. We found the integrated dissipation rates to be largely independent of viscosity and thermal diffusivity, despite the differences in the frequency dependent profiles. This is a useful result as our parameter values lie outside the range of realistic values due to computational constraints. This is also in agreement with the analogy with a damped harmonic oscillator, where we established that the peak width is proportional to the damping rate, and peak heights are inversely proportional to damping, resulting in counteracting effects in the integrated quantity.

When comparing a staircase-like profile with an equivalent uniformly stratified layer, we found that provided there are a sufficient number of steps (a few) the staircase acts like that of a uniformly stratified layer in most cases. Despite this, however, it does alter the frequency dependent dissipation, particularly in frequency ranges containing resonances, so it could impact the dissipation rate significantly depending on the tidal forcing frequency. When considering the case of an isolated stratified layer near the molecular/metallic transition region, we observe a large resonance corresponding to a single interfacial mode. This can have a significant contribution to the overall dissipation rate and due to the magnitude of this single resonance could have an impact for resonance locking scenarios. The stable layer also supports short wavelength internal gravity waves leading to low frequency resonances that contribute to the dissipation rate.

Overall, we found that stable stratification, whether a uniform layer, a staircase-like structure, or a Helium rain layer, can contribute to the dissipation rate by the introduction of additional resonances into the system. Even in cases where the contribution to the integrated dissipation quantity is low, the properties of the stable stratification can have a strong effect at particular frequencies, which if sufficiently close to those of the tidal forcing, could have implications for orbit and spin migration rates.

Chapter 6

Tidal dissipation in rotating and stratified planets

In this final results chapter, we are considering a rotating body to study the preliminary effects rotation has on the dynamics. We continue to use the governing equations and numerical methods that were outlined in Chapter 4, however, unlike in the preceding chapter we now consider cases in which $\Omega \neq 0$. Most notably, this allows for inertial and gravito-inertial waves to be excited and subsequently dissipated (see Section 1.5). This is a more realistic model as it is likely that the Coriolis force is important for planetary applications, in particular at the frequencies of tidal forcing in these systems.

6.1 The additional properties of a rotating system

The additional excitation of inertial wave and gravito-inertial waves (over the internal gravity waves, interfacial waves and surface gravity waves observed in Chapter 5) means we now see more resonances at low frequencies that align with these modes. Figure 6.1a shows the viscous (D_{visc}), thermal (D_{therm}), and total (D_{total}) dissipation rates for a rotating body with $\Omega = 0.4$ for which $\alpha = 0.5$, $\bar{N} = 0$

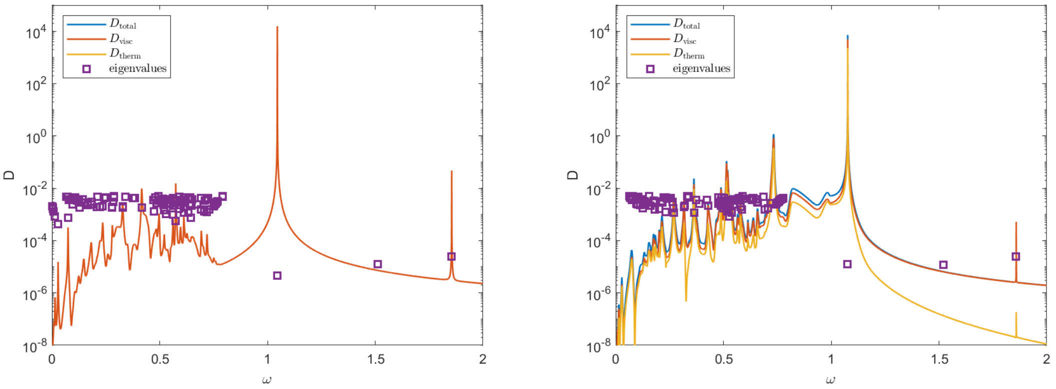

(a) $\alpha = 0.5$, $\bar{N}^2 = 0$

(b) $\alpha = 0.1$, $\beta = 0.5$, $\bar{N}^2 = 1$

Figure 6.1: Illustrative examples of the dissipation as a function of frequency in two models with the addition of rotation, and the eigenvalues solutions over-plotted for both cases. One example of an entirely convective interior outside a solid inner core (panel a) and one with a stratified layer extending to half the planetary radius (panel b). In both cases we keep $\Omega = 0.4$, $\nu = \kappa = 10^{-6}$.

and $\nu = \kappa = 10^{-6}$. We adopt $\Omega = 0.4$ throughout most of this chapter as this is approximately Saturn-like. This portrays a planet in which a large solid core is surrounded by a well-mixed convective envelope allowing for pure inertial waves to be excited in this envelope at low frequencies $|\omega| < 2\Omega = 0.8$, as well as the surface gravity modes at higher frequencies. We can observe the peaks of enhanced dissipation close to resonances with inertial modes leading to the irregular frequency dependence characteristic of these modes. We used a large core size here to enhance the appearance of inertial waves in the tidal response, in order to illustrate their properties (Ogilvie, 2009; Rieutord, 2009; Rieutord & Valdettaro, 2010). The eigenvalues (purple squares) agree well with the locations and heights of the peaks, where the least damped modes correspond to the largest resonances, with the strongest dissipation. In this case only the least damped modes have been plotted, with the cut-off chosen purely for aesthetic reasons.

As in the non-rotating case, we excite the large surface gravity mode resonance around $\omega = 1$, however in this case it has been shifted to a significantly lower frequency. It can be shown (e.g. Lebovitz, 1961; Barker et al., 2016), that rotation causes the splitting of this mode for a given l and different m values. For example, in Lebovitz (1961) where they consider a rotationally deformed, self-gravitating body, in the limit is small rotation (deformation) the $l = 2$ surface gravity

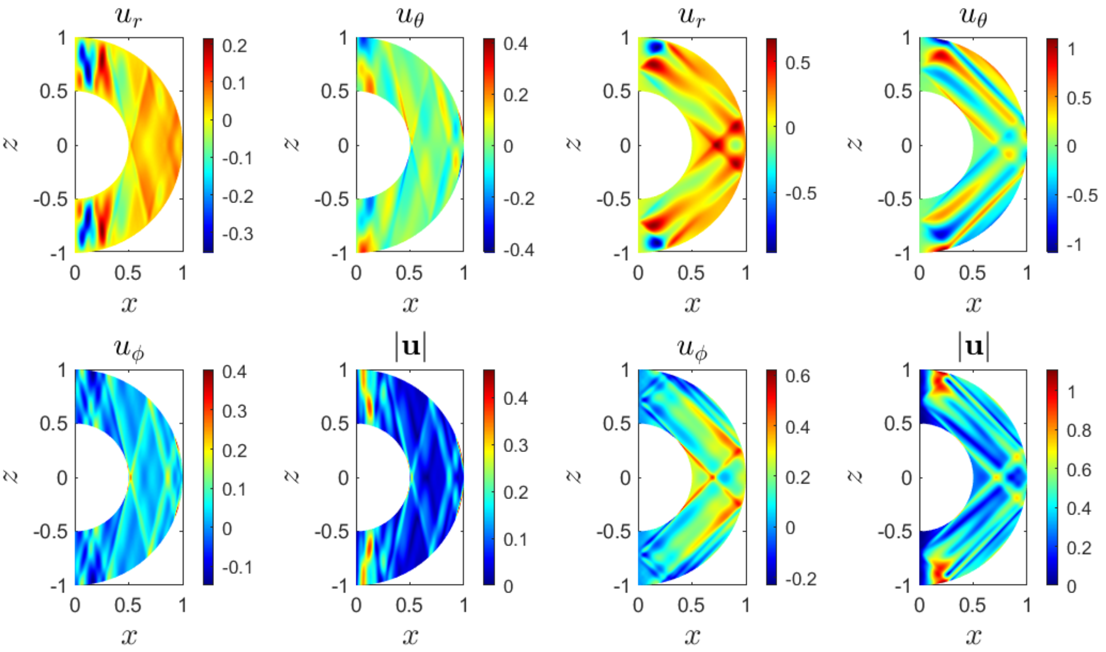

(a) $\omega = 0.181$

(b) $\omega = 0.561$

Figure 6.2: Illustrative examples of the forced response in a convective envelope, for which $\alpha = 0.5$, $\beta = 1.0$, $\bar{N}^2 = 0$, $\Omega = 0.4$, $\nu = \kappa = 10^{-6}$. Both panels are examples of tidally-forced inertial waves with Panel a an example with a lower forcing frequency.

mode is split into five modes, $\omega = \omega_0 - \frac{m}{2}\Omega$, where $m = -2, -1, 0, 1, 2$ and ω_0 is non-rotating frequency $\omega_0 = \pm\omega_d\sqrt{l}$. Similar results could be obtained in this model and as we are restricted to $m = 2$ due to the symmetry, in our system only the $m = 2$ splitting of the mode is relevant and appears as a shift in the location of the surface gravity mode. There is an additional resonance close to $\omega = 1.8$, which is caused by the coupling of different spherical harmonics due to the Coriolis force and therefore corresponds to resonance with the $l = 4$, $m = 2$, surface gravity mode (again shifted due to the splitting). Around $\omega = 1.5$ there is an eigenvalue solution that does not align to any peak, this corresponds to the $l = 3$ surface gravity mode which, although a solution to the unforced eigenvalue problem, is not excited in reality, as although all l's are coupled by the Coriolis force, the symmetry in the $l = 2$ tidal forcing means that only modes with the same symmetry (i.e. equatorially symmetric in u_r and therefore even l for $m = 2$) are excited.

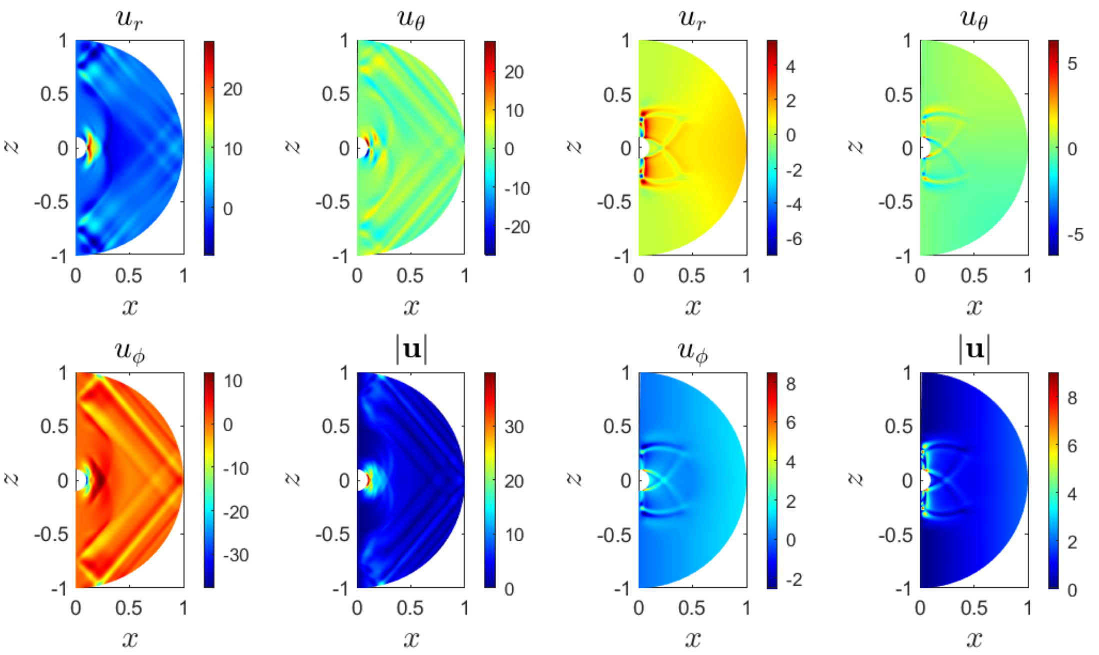

(a) $\omega = 0.514$

(b) $\omega = 0.95$

Figure 6.3: Illustrative examples of the forced response within a planet with a stably stratified core and convective envelope. In both cases we keep $\alpha = 0.1$, $\beta = 0.5$, $\bar{N}^2 = 1$, $\Omega = 0.4$, $\nu = \kappa = 10^{-6}$. Panel a shows gravito-inertial waves in the stratified layer and inertial waves in the convective envelope. Panel b shows gravito-inertial waves in the stratified layer only.

In Figures 6.2 to 6.4 we show the spatial structure of our forced response, which is consistent with previous studies incorporating rotation and stratification (e.g. Rieutord & Valdettaro, 1997; Dintrans et al., 1999; Ogilvie & Lin, 2004; Rieutord, 2009). In Figure 6.2, we show the spatial structure of the forced response at two different forcing frequencies, and we observe the inertial wave beams that form in the convective shell. Figure 6.2a and Figure 6.2b show the spatial structure for forcing frequencies $\omega = 0.181$ and $\omega = 0.561$, respectively. It can be shown using the dispersion relation, equation 1.32, that

$$\cos\theta_i = \frac{\omega}{2\Omega}, \tag{6.1}$$

where θ_i is the angle between the rotation axis $\hat{\boldsymbol{\Omega}}$ and wavenumber $\hat{\boldsymbol{k}}$. By comparing the two cases we see the expected correspondence between the angle of the wave beam with the axis of rotation and forcing frequency.

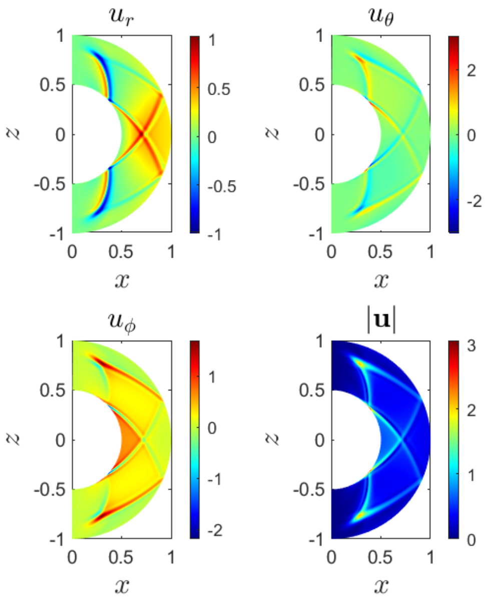

(a) $\omega = 0.732$

Figure 6.4: Illustrative examples of the forced response within a rotating planet with a stratified layer, showing a gravito-inertial wave response. Parameters are $\alpha = 0.5$, $\beta = 1.0$, $\bar{N}^2 = 1$, $\Omega = 0.4$, $\nu = \kappa = 10^{-6}$.

Figure 6.1b shows a similar but potentially more realistic case where instead of a large solid core we consider a stably stratified layer that extends to half the planetary radius. Therefore we consider a buoyancy profile described using equations 4.41 with $\alpha = 0.1$, $\beta = 0.5$, and $\bar{N} = 1$. We have kept rotation, viscosity, and thermal diffusivity constant with $\Omega = 0.4$, $\nu = \kappa = 10^{-6}$. This is also equivalent to the case considered in Figure 5.1b but with the addition of rotation. Therefore as well as exciting the inertial waves in the outer convective envelope, as observed in the solid core case, we also excite gravito-inertial waves in the extended stably stratified layer over a larger range of frequencies $|\omega| < \sqrt{\bar{N}^2 + 4\Omega^2} = 1.28$.

In Figure 6.3a we consider the spatial structure of the forced solution at a frequency of $\omega = 0.514$, a frequency which is within the range of both gravito-inertial waves and inertial waves if $\bar{N} = 0$. We observe both these waves to be excited, the gravito-inertial waves within the stratified core, and the inertial waves within the convective envelope. At this point we note the similarity between the spatial structure in the outer envelope with the example shown in Figure 6.2b where

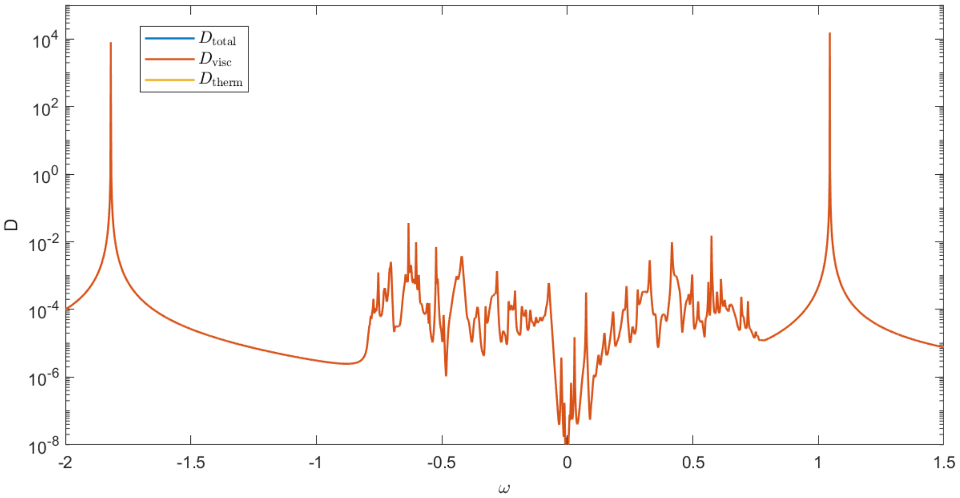

Figure 6.5: Illustrative example of the dissipation rate as a function of tidal forcing frequency for both positive and negative frequencies. The model considered is the same as that shown in Figure 6.1a with $\alpha = 0.5$, $\bar{N} = 0$, $\Omega = 0.4$, $\nu = \kappa = 10^{-6}$.

the forcing frequency is similar. When we consider a higher frequency $\omega = 0.95$, outside the inertial wave range but within the gravito-inertial wave range, shown in Figure 6.3b, we can see that only gravito-inertial waves within the stably stratified layer are excited.

Finally, Figure 6.4 is an example of a gravito-inertial wave excited in a stably stratified envelope around a solid core, where in this case $\alpha = 0.5$, $\beta = 1.0$, $\bar{N} = 1$, $\nu = \kappa = 10^{-6}$. This demonstrates how in a region with stable stratification, instead of the straight lines characteristic of an inertial wave we observe the curved lines characteristic of the gravito-inertial waves (Dintrans et al., 1999).

Negative frequencies

One significant differences between the tidal response in a rotating and a non-rotating case is the breaking of the symmetry between negative and positive forcing frequencies, such that $D(\omega) \neq D(-\omega)$. Figure 6.5 shows the dissipation rate for both positive and negative tidal forcing frequencies for the same model as is shown in Figure 6.1a, with $\alpha = 0.5$, $\bar{N} = 0$, $\Omega = 0.4$, $\nu = \kappa = 10^{-6}$. At low magnitude frequencies we have additional Rossby modes (also known as planetary waves). Rossby modes can be found by considering conservation of vorticity, and in the absence of a background flow and stratification, have a dispersion relation (Papaloizou & Pringle, 1978; Zaqarashvili et al., 2021),

$$\omega = -\frac{2m\Omega}{l(l+1)}, \tag{6.2}$$

which has strictly the opposite sign to rotation (retrograde). Additionally (and again in the absence of stratification), purely toroidal modes can be excited with a dispersion relation (Ogilvie, 2009),

$$\omega = -\frac{2\Omega}{m+1}, \tag{6.3}$$

where again we note the strictly negative frequency. At higher magnitude of frequencies, the direction of the shift in frequency of the surface gravity mode again depends on the sign of Ω, which we also observe.

Although this does affect the dissipation rate at some forcing frequencies (e.g. Ogilvie, 2009), and may well have implications when comparing to real observational quantities, due to time constraints and to allow easier comparison with the non-rotating system, we continue to discuss only the positive frequencies here. This is reasonable as we are primarily concerned with the overarching behaviour of the modes in general rather than specific resonances, therefore expect our conclusions to hold generally for negative frequencies.

6.2 Dependences on the parameters of the system

As we did for the analysis carried out in Chapter 5, we again would like to further understand how the dissipation depends on the parameters of the system. In this chapter however we consider two different frequency weightings. We continue to consider the frequency-averaged dissipation introduced in Section 4.5 that was used in Chapter 5, however in some circumstances we consider a different weighting,

$$\bar{D}_2 = \int_{\omega_{min}}^{\omega_{max}} \frac{D(\omega)}{\omega^2}\,\mathrm{d}\omega. \tag{6.4}$$

We consider this quantity as it allows for comparison with the impulsive calculation in Ogilvie (2013), where in the low frequency limit, for the unstratified case with a solid core, they used impulsive forcing to calculate the associated energy transfer $\hat{E}$ analytically. They find that $\hat{E} \propto \int \mathrm{Im}[k_l^m]/\omega\,\mathrm{d}\omega$, which can be shown to correspond tidal dissipation by

$$\hat{E} = \frac{1}{2\pi} \int_{\infty}^{\infty} \frac{D}{\omega^2}\,\mathrm{d}\omega, \tag{6.5}$$

which has an ω^{-2} dependency, motivating this weighting.

We note that in many of the parameter ranges considered in the rotating cases, the highest frequency gravito-inertial waves can have frequencies comparable to those of the surface gravity modes, therefore it is not always possible to separate the behaviour of these two types of modes. Unlike in the non-rotating case where $\omega_{max} = \bar{N}$ was an obvious limit to take to include internal gravity modes and exclude the surface gravity mode behaviour, we can't make the same assumption here about the gravito-inertial wave limit $\omega_{max} = \sqrt{\bar{N}^2 + 4\Omega^2}$. We include some examples of an integrated quantity in this chapter, as it still has illustrative uses, but we emphasise that these results should be interpreted with caution as the frequency-averaged dissipation measure is less robust to the frequency interval considered than in the non-rotating case.

6.2.1 Dependence on rotation rate Ω

Having introduced rotation as a new and key element in the problem, we first turn our attention to altering this parameter and studying the consequences. We focus on two key profiles, a stably stratified layer extending across the entire planet $\beta = 1.0$ and a stably stratified layer that extends to half the planetary radius $\beta = 0.5$, with a well-mixed convective region above.

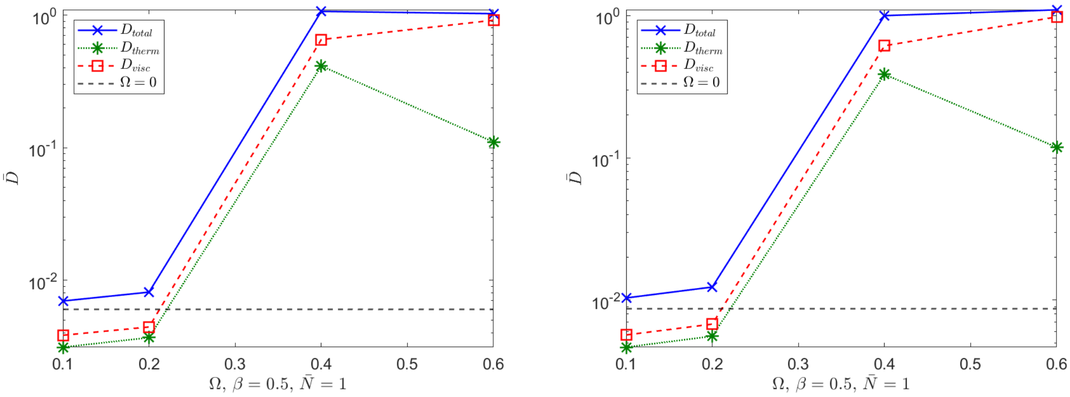

(a) $\bar{D} = \int D/\omega \ \mathrm{d}\omega$ (b) $\bar{D} = \int D/\omega^2 \ \mathrm{d}\omega$

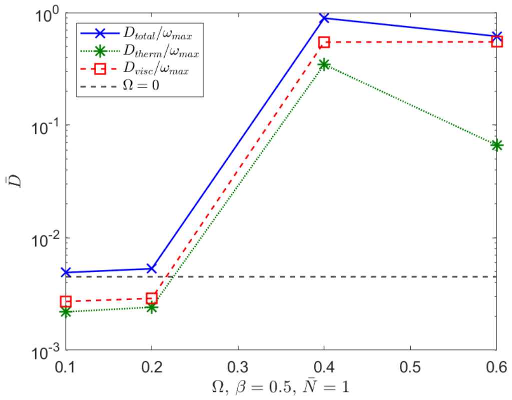

(c) $\bar{D} = (1/\Delta\omega) \int D \ \mathrm{d}\omega$

Figure 6.6: Comparison of different frequency weightings for the frequency-averaged dissipation as a function of rotation rate. Other parameters are fixed at $\alpha = 0.1$, $\beta = 0.5$, $\bar{N} = 1$, $\nu = \kappa = 10^{-6}$. In all cases the integration limits have been taken to be $\omega_{min} = 0$ and $\omega_{max} = \sqrt{\bar{N} + 4\Omega^2}$.

In Figure 6.6 we consider just the case for which only half the planet is stably stratified, $\beta = 0.5$, and first compare the outcomes of three different weightings for the integrated (frequency-averaged) dissipation rate. We consider: the $\frac{1}{\omega}$ weighting used in Chapter 5, the $\frac{1}{\omega^2}$ weighting for comparison with Ogilvie (2013) and a "mean average", which we define to be $\bar{D} = \frac{1}{\omega_{max} - \omega_{min}} \int D \ \mathrm{d}\omega$. In all three cases we have kept the integration limits the same as the range for gravito-inertial waves, $\omega_{min} = 0$ and $\omega_{max} = \sqrt{N^2 + 4\Omega^2}$; the same quantity for the corresponding non-rotating case has been plotted for reference in each case. We can see that there is a slight quantitative difference between these three weightings but there are no qualitative differences. In all three cases we see that the dissipation is larger than found in the non-rotating case and a large jump between $\Omega = 0.2$ and $\Omega = 0.4$. However, we remember than in the case of rotation, $\omega_{max} = \sqrt{N^2 + 4\Omega^2}$ is no longer a robust limit and it is more instructive to consider the frequency dependent solution. Considering the vertical lines in Figure 6.9, which mark the gravito-inertial wave limit, we can see that for the rotation rates $\Omega = 0, 0.1, 0.2$, the surface gravity mode is well above ω_{max}, whereas for $\Omega = 0.4, 0.6$, it is below this limit. In fact, we see that in the case of $\Omega = 0.6$, the surface gravity mode no longer appears as an isolated peak. It is therefore likely that the surface gravity mode is to a large part dictating the trends observed in Figure 6.6.

In Figure 6.7 we consider different integration limits, again showing all three frequency weightings. On the left-hand side, we consider a lower upper limit $\omega_{max} = 1$ which removes the surface gravity mode from most cases (for $\Omega = 0.6$ the surface gravity mode is still included). We can see that in all three plots the frequency-averaged quantities increase away from the non-rotating baseline as rotation rate increases and the inertial wave response is enhanced. On the right-hand side, we consider a higher integration limit $\omega_{max} = 1.8$, which incorporates the surface gravity mode behaviour in all cases. Using this limit, we observe that there is a difference between the different weightings and in fact the weightings that give the most emphasis to dissipation due to inertial wave excitation shows an increase in the averaged quantity as rotation rate increases.

We also consider the case in which the stratified layer extends to the planetary radius $\beta = 1.0$, Figure 6.8 with all other parameters fixed at $\alpha = 0.1$, $\bar{N} = 1$, $\nu = \kappa = 10^{-6}$. Due to the similarities between the weightings, we have shown here just the frequency-averaged measure used in the non-rotating case, but we have included all three limits of integration discussed so far in this section. We see that the trends observed in the case of $\beta = 0.5$, hold here. The only key difference is that, for data points in which the surface gravity mode is not included in the integration, the overall dissipation is lower in the case of $\beta = 0.5$, as the low frequency dissipation rate is lower in this case.

Due to the uncertainty in the integrated quantity, it is important to discuss the profiles of the frequency-dependent dissipation alongside the spatial structure

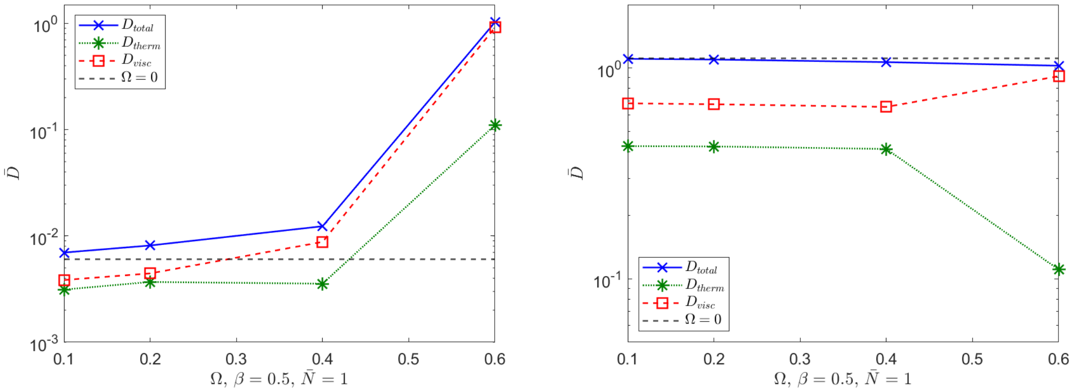

(a) $\bar{D} = \int D/\omega \, \mathrm{d}\omega, \omega_{min} = 0, \omega_{max} = 1$

(b) $\bar{D} = \int D/\omega \, \mathrm{d}\omega, \omega_{min} = 0, \omega_{max} = 1.8$

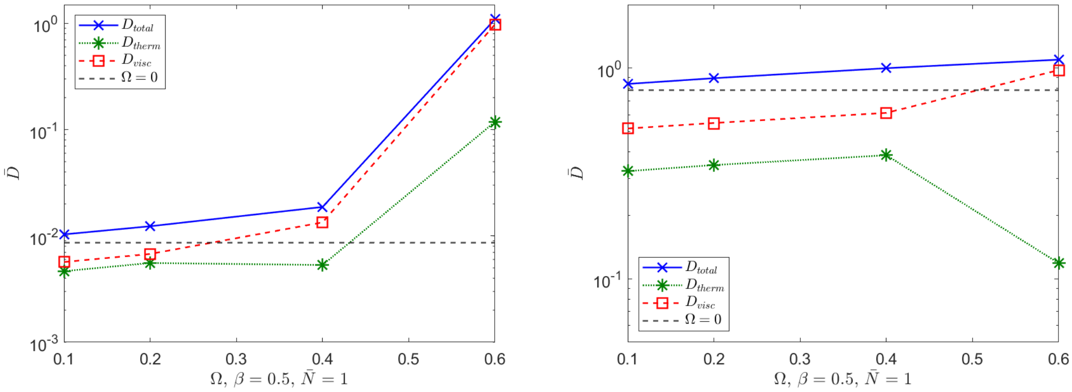

(c) $\bar{D} = \int D/\omega^2 \, \mathrm{d}\omega, \omega_{min} = 0, \omega_{max} = 1$

(d) $\bar{D} = \int D/\omega^2 \, \mathrm{d}\omega, \omega_{min} = 0, \omega_{max} = 1.8$

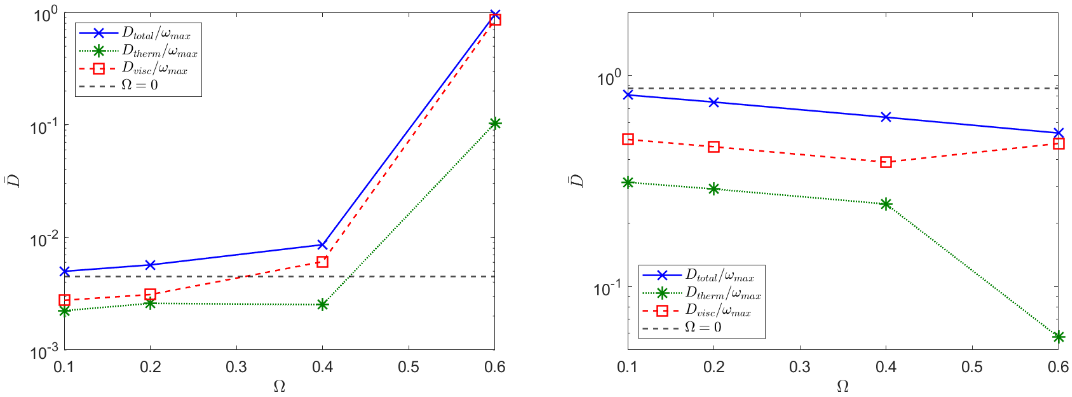

(e) $\bar{D} = (1/\Delta\omega) \int D \, \mathrm{d}\omega, \omega_{min} = 0, \omega_{max} = 1$

(f) $\bar{D} = (1/\Delta\omega) \int D \, \mathrm{d}\omega, \omega_{min} = 0, \omega_{max} = 1.8$

Figure 6.7: Comparison of different frequency weightings and integration limits for frequency-averaged dissipation as a function of rotation rate. Other parameters are fixed at $\alpha = 0.1$, $\beta = 0.5$, $\bar{N} = 1$, $\nu = \kappa = 10^{-6}$.

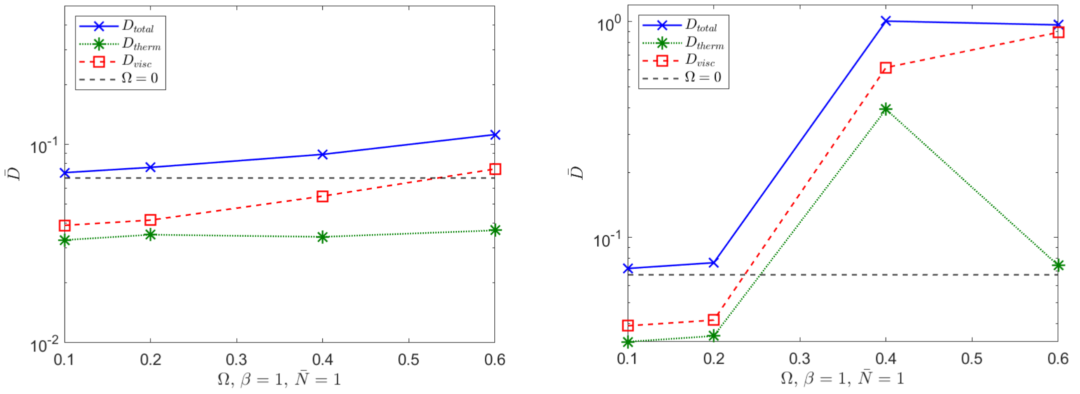

(a) $\bar{D} = \int D/\omega \, \mathrm{d}\omega, \omega_{min} = 0, \omega_{max} = 1$

(b) $\bar{D} = \int D/\omega \, \mathrm{d}\omega, \omega_{min} = 0, \omega_{max} = \sqrt{N^2 + 4\Omega^2}$

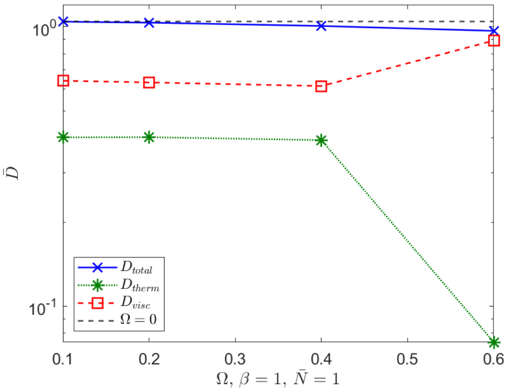

(c) $\bar{D} = \int D/\omega \, \mathrm{d}\omega, \omega_{min} = 0, \omega_{max} = 1.8$

Figure 6.8: Comparison of integration limits for the frequency-averaged dissipation as a function of rotation rate for a fully stratified planet. Other parameters at fixed at $\alpha = 0.1$, $\beta = 0.5$, $\bar{N} = 1$, $\nu = \kappa = 10^{-6}$.

of the forced solution. Figures 6.9a and 6.9b show the total dissipation (D_{total}) for four different rotation rates, as well as the corresponding non-rotating cases from Chapter 5 (black-dashed line); the cases shown are for $\beta = 1$ and $\beta = 0.5$, respectively. We can see that there is a non-trivial balance between the roles of the buoyancy and Coriolis forces. In all rotating cases we see gravito-inertial waves in the expected range $\omega < \sqrt{\bar{N}^2 + 4\Omega^2}$. As well as observing the increasing range of modes we also see that the irregular pattern characteristic of inertial modes is more pronounced as rotation rate increases. Indeed, at a low rotation rate, $\Omega = 0.1$, the profile is similar to that of $\Omega = 0$, as the buoyancy forces appear to dominate. We also note when comparing the two figures that in the case of a partially stratified planet, varying rotation has a more pronounced effect. This

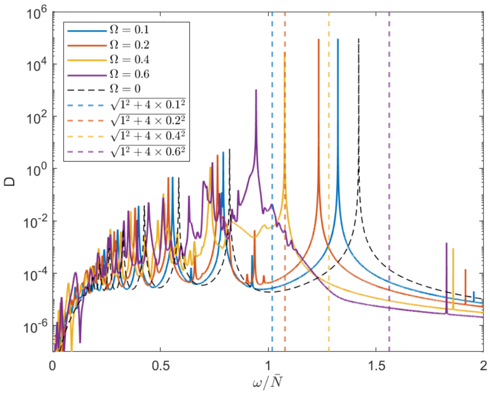

(a) $\beta = 0.5$

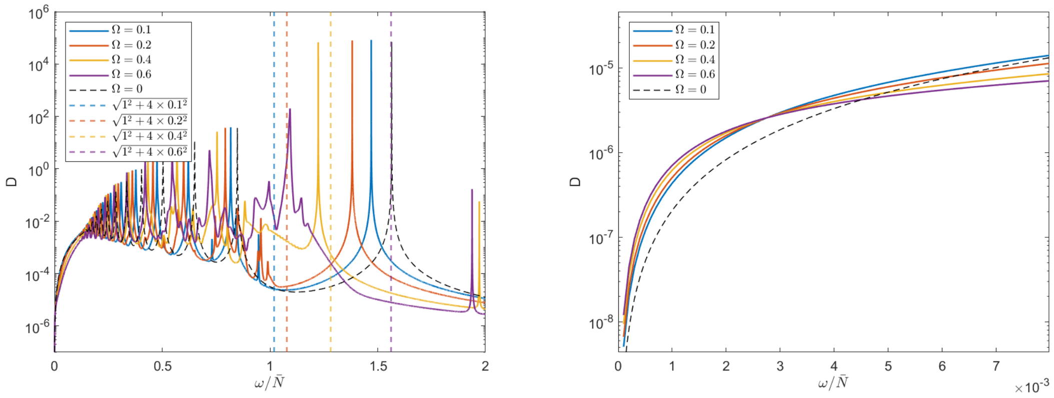

(b) $\beta = 1$ (c) $\beta = 1$

Figure 6.9: Frequency dependence of the dissipation rate for varying rotation rates, in all cases $\alpha = 0.1$, $\bar{N} = 1$, $\nu = \kappa = 10^{-6}$. Panel a shows a stratified layer extending to half the planetary radius, panels b and c show a uniform layer extending to the planet radius, with c showing just the low frequency regime (travelling wave).

is because the stratified layer acts similarly to a large solid core, enhancing the excitation of inertial waves, which are not excited in a homogeneous full sphere. Figure 6.9c, shows the low frequency range in the case of a stratified layer extending to the planetary surface. We can see that at low frequencies there is a clear dependence on Ω, which transitions between the two regions. It is possible that similar analysis to that carried out in the travelling wave regime in Section 5.1.1 (and has been considered for other models such as Papaloizou & Savonije (1997); Ogilvie & Lin (2004); Chernov et al. (2013)) could explain this dependence but this we leave as an open question.

Turning our attention to the spatial structure we consider Figure 6.10 which shows the forced solution for the four different increasing rotation rates (rows)

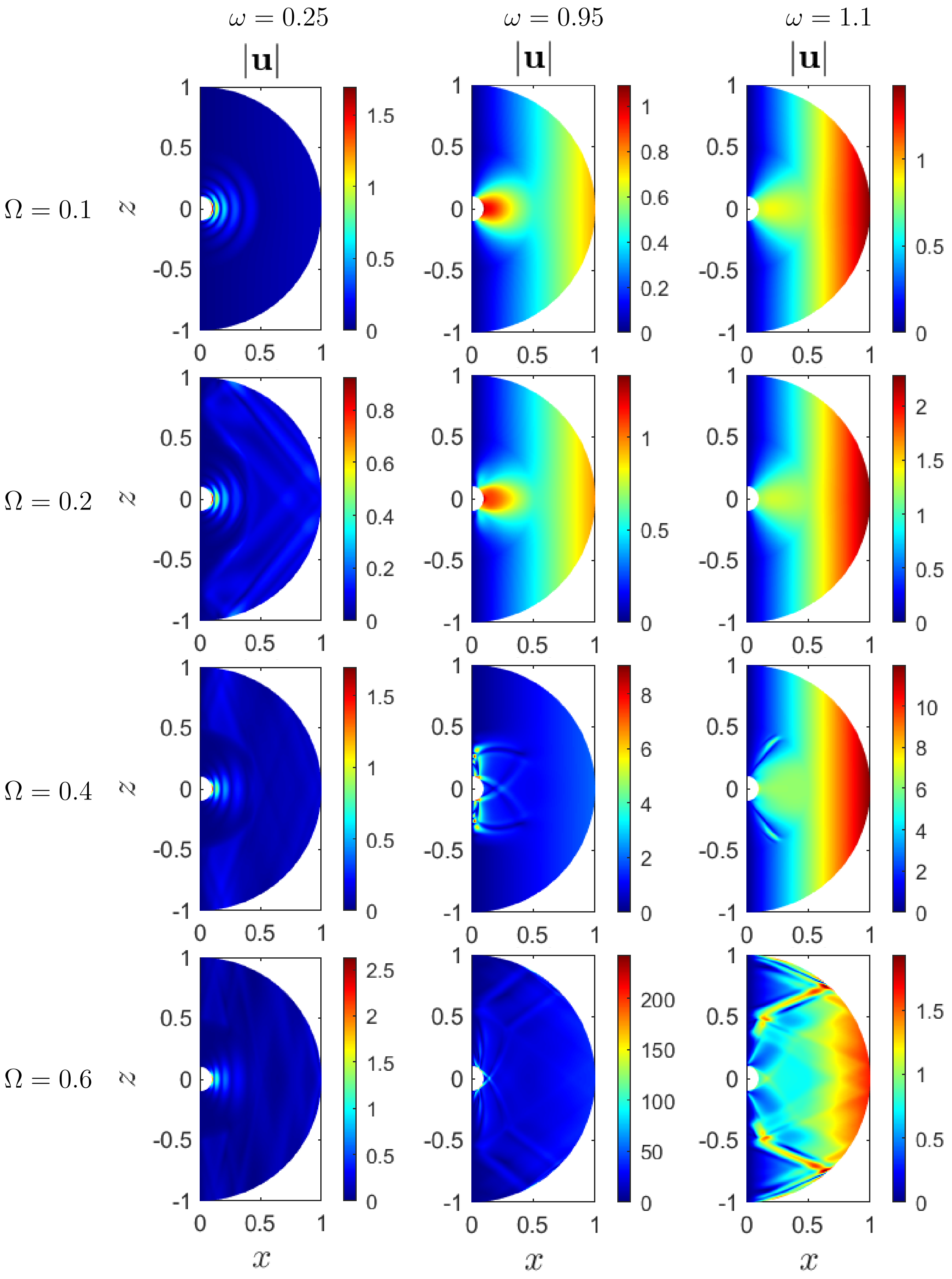

Figure 6.10: Examples of the spatial structure for different rotation rates and forcing frequencies, in all cases we consider a stably stratified layer extending to half the planetary radius $\alpha = 0.1$, $\beta = 0.5$, $\bar{N} = 1$, $\nu = \kappa = 10^{-6}$.

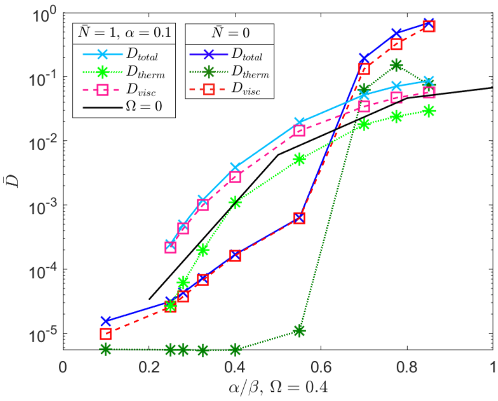

(a) $\bar{D} = \int D/\omega \, \mathrm{d}\omega, \omega_{min} = 0, \omega_{max} = 1$

Figure 6.11: Frequency-averaged dissipation as a function of core size. Comparison cases where a convective layer sits above a solid core ($\bar{N} = 0$ and varying α) with a case where a stably stratified layer extends to the same radius ($\bar{N} = 1$, $\alpha = 0.1$, varying β). Other parameters kept constant at $\Omega = 0.4$ and $\nu = \kappa = 10^{-6}$.

with increasing forcing frequency (columns). We see clear agreement with the predicted range for inertial and gravito-inertial waves in the convective envelope and outer core, respectively, as we move between the different regimes. Additionally we observe larger magnitude inertial waves as rotation rate Ω increases, corresponding to the larger rates of dissipation. Note the changing colour bars between the different cases.

6.2.2 Dependence on core size

A large area of uncertainty is how far a stable layer that forms would extend throughout a planetary interior, with current estimations varying significantly, see Table 5.2. We know from previous studies that the size of a solid core can significantly enhance the excitation of inertial waves. Here we compare two scenarios, cases with a solid core with a convective envelope above ($\bar{N} = 0$, varying α) and cases where a small solid core is surrounded by a stably stratified layer again beneath a convective envelope ($\bar{N} = 1$, $\alpha = 0.1$, varying β).

Figure 6.11 shows the frequency-averaged profiles for these two cases. The darker lines show the case without stratification where the dependence on the radius of the solid core α, whilst the lighter coloured lines show the cases with a

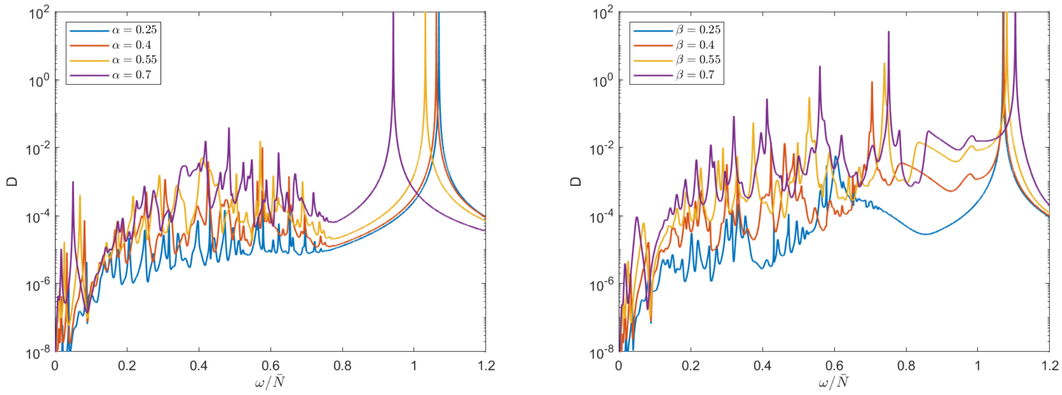

(a) $\bar{N} = 0$ and varying α

(b) $\bar{N} = 1$, $\alpha = 0.1$, varying β

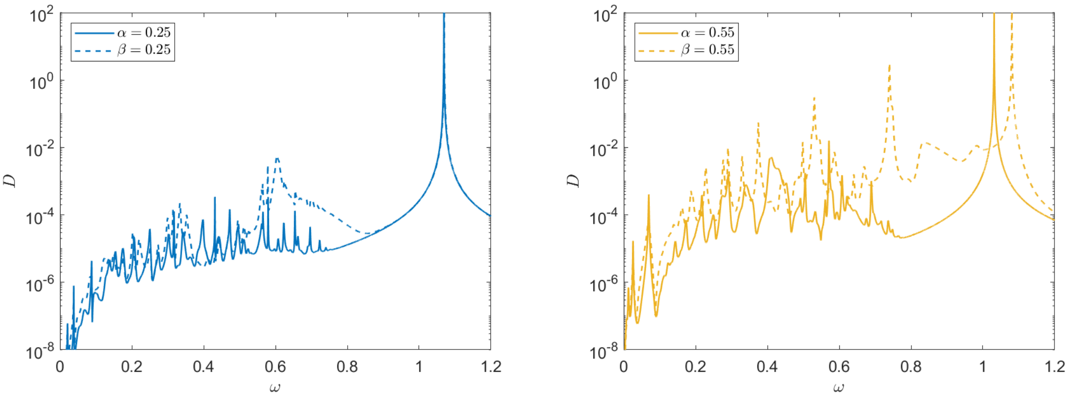

(c) Core extending to $0.25r_0$

(d) Core extending to $0.55r_0$

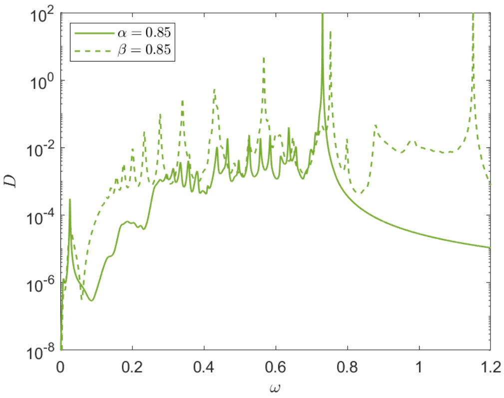

(e) Core extending to $0.85r_0$

Figure 6.12: Frequency dependence of the dissipation rate for different core sizes, comparing both a solid core and stably stratified core, in all cases $\Omega = 0.4$, $\nu = \kappa = 10^{-6}$. Panels a and b show a solid core and stratified layer, respectively, for different core sizes. Panels c to e compare a solid core to a stratified layer for three different radii.

stably stratified core β. The black line shows the equivalent trend found in the non-rotating cases, where we consider a small core with a stably stratified region above. We can see that, in both cases, the frequency-averaged dissipation shows a strong dependence on core size, but this trend varies between the two core types. For core sizes less than $0.5r_0$ there are larger dissipation rates where there is a stably stratified core; for larger core sizes (perhaps larger than would be expected in the case of Jupiter and Saturn), we see the opposite trend. This suggests that for the smaller core sizes, the stratified layer acts as a solid core for the excitation of inertial waves, with additional contribution to the overall dissipation rate arising from the excitation of gravito-inertial waves in the stratified layer. We consider the trend found for a larger core with caution, as when considering the frequency-dependent dissipation in Figure 6.12, we can see that for these cases the surface gravity mode has shifted to frequencies less that the integration limit $\omega = 1$ when considering a solid core which contributes to the dissipation rate.

Considering further the frequency-dependent dissipation rate in Figure 6.12, we can understand more about the contribution of a stratified core. In Figures 6.12a and 6.12b we compare cases with differently sized cores for a solid core and a stratified core, respectively. In both cases, we see that the magnitude of the resonances increases as the core size increases, but we note however some differences. For cases with a stratified core, we observe the increased frequency range of the resonances matching that of gravito-inertial waves rather than inertial waves. Additionally, in the case when a stably stratified layer extends to $0.7r_0$, there are regular discrete peaks that are characteristic of internal gravity waves dominate around a forcing frequency of 0.2. In Figures 6.12c to 6.12e, we have compared the total dissipation rates for cases with a solid core and stably stratified core for three different radii, 0.25, 0.55 and 0.85. We can see clearly that for the smallest core size, the inertial wave response is very similar in both cases, departing from each other at frequencies around $0.6 - 0.9$ only. However, as we increase the core size we increase the contribution of the gravito-inertial waves so this agreement is worse. Indeed, when the core extends as far as $0.85r_0$, we can see at frequencies less than 0.6, the dissipation rate in the case of a stably stratified core resembles that of the results found in the equivalent non-rotating system, more than the equivalent solid core case. We note also that the shift in the frequency of the surface gravity mode varies between these cases as the stratified layer does have an effect on the frequency of this mode. Finally, we note, that it is when considering these thin shell convective regions (large cores) that we expect the negative frequency Rossby modes to be more significant, which require further investigation than carried out here.

6.2.3 Dependence on step number

We now explore the consequences of semi-convective layers forming potentially as a result of double-diffusive convection. As in the non-rotating case, we consider a staircase-like density profile as defined by equation 4.43, and will consider cases in which $\alpha = 0.1$, $\beta = 1.0$, $\bar{N} = 1$, $\delta r = 0.03$, $\Omega = 0.4$ and $\nu = \kappa = 10^{-6}$, with varying step number. As we discussed in the non-rotating case we consider $\beta = 1.0$, to allow for larger step numbers with reduced numerical demand. In Figure 6.13a we show the frequency-averaged dissipation as step number increases; we have in this case shown just the $\frac{1}{\omega}$ weighting and used an upper integration limit of $\omega_{max} = 1$ to exclude the surface gravity wave dependence. Note, the lower limit of $\omega_{min} = 0.1$ has been chosen for purely numerical reasons; lowest frequency waves require the highest resolution and contribute little to the overall dissipation in this measure. For comparison, we also show the equivalent non-rotating case as a function of step number (black-dashed line), as well as the uniformly stratified layer with equivalent mean stratification (black solid line).

We can see that the dissipation for all step numbers considered is higher than both a uniformly stratified medium and the non-rotating cases. We can see that although there is a trend towards the uniformly stratified case, it does not converge to this result as quickly as we found in the non-rotating case as we increase the number of steps (see Figure 5.11a). Considering Figure 6.14, which shows the frequency-dependent dissipation rates for different step numbers, we

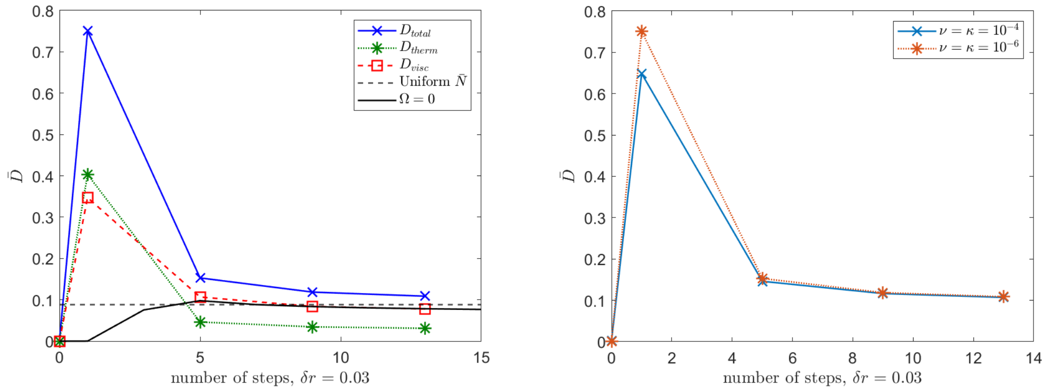

(a) $\bar{D} = \int D/\omega \, d\omega$, $\omega_{min} = 0.1, \omega_{max} = 1$ (b) $\bar{D} = \int D/\omega \, d\omega$, $\omega_{min} = 0.1, \omega_{max} = 1$

Figure 6.13: Frequency-averaged dissipation as a function of number of steps. Other parameters kept constant at $\alpha = 0.1$, $\beta = 1.0$, $\bar{N} = 1$, $\Omega = 0.4$, $\nu = \kappa = 10^{-6}$. Panel a compare total, viscous and thermal dissipation with the total dissipation of the uniformly stratified case as well as the non-rotating case. Panel b compares two different viscosities with fixed Prandtl number.

can see that at low frequencies the behaviour varies for different numbers of steps. Note the the limit for gravito-inertial waves is $\omega < \sqrt{N_{max}^2 + 4\Omega^2}$ and when considering a staircase-like structure $N_{max} \geq \bar{N}$, increasing the range for inertial waves slightly (but with no significant implications for our parameter values, so we do not focus on this aspect).

We first compare the cases of zero steps, one step and five steps, noting that zero steps consists of a small solid core with a convective envelope to the outer edge. At low frequencies, although inertial waves are excited in the convective shells in all three cases, these are barely visible for the case of zero steps, where there is only the small solid core to launch inertial waves from. As we increase the number of steps to one and then five, the excitation of inertial waves occurs from boundaries at additional and increasingly larger radii, leading to additional dissipation. Following this, we now compare the cases with five, nine and 13 steps and find there are significantly smaller differences between these cases. At this point the outer radius does not vary significantly as the number of steps is increased. Figure 6.15 shows the forced solutions at $\omega = 0.25$ for all five step numbers in which we can see the inertial wave beams forming in the convective layers, with a very small amplitude response in the case of zero steps, and increasing amplitude of the response as we increase the number of steps.

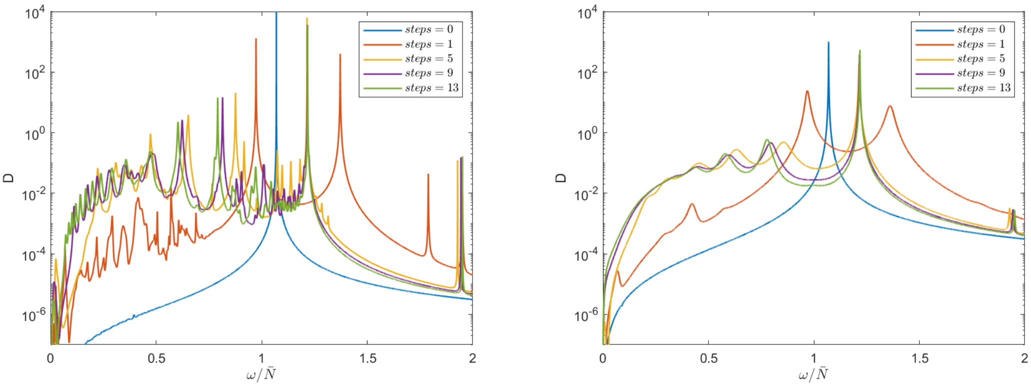

(a) $\nu = \kappa = 10^{-6}$

(b) $\nu = \kappa = 10^{-4}$

Figure 6.14: Frequency dependence of dissipation for different numbers of steps in the staircase density profile. In all cases $\alpha = 0.1$, $\beta = 1$, $\bar{N} = 1$. In panel a, we fix $\nu = \kappa = 10^{-6}$ and in panel b we fix $\nu = \kappa = 10^{-4}$.

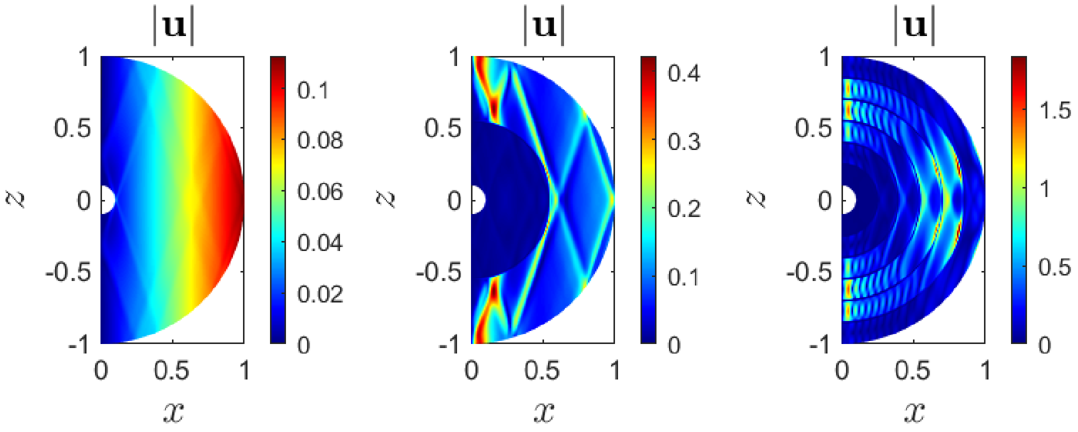

(a) steps= 0

(b) steps= 1

(c) steps= 5

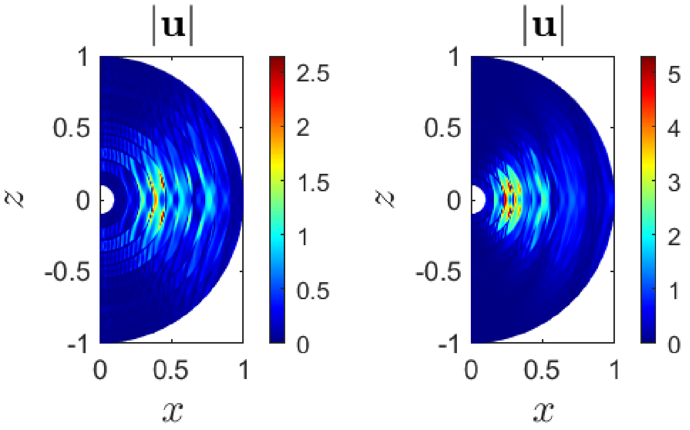

(d) steps= 9

(e) steps= 13

Figure 6.15: Examples of the spatial structure for 0,1,5,9 and 13 steps, in all cases $\alpha = 0.1$, $\beta = 1.0$, $\bar{N} = 1$, $\nu = \kappa = 10^{-6}$, and a forcing frequency $\omega = 0.25$.

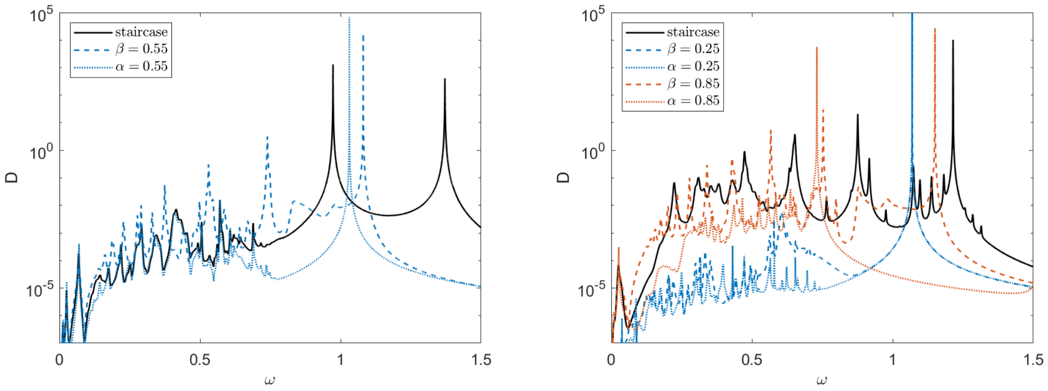

(a) Single interface

(b) Five interfaces

Figure 6.16: Comparison between total dissipation for profiles with interfaces, uniformly stratified layers and a solid core, in all cases $\Omega = 0.4$ and $\nu = \kappa = 10^{-6}$. The black solid lines are the single and five step cases in panels a and b respectively. The dashed coloured lines describe a stratified layer with $\alpha = 0.1$ and $\bar{N} = 1$, and solid coloured lines a solid core with $\bar{N} = 0$. The blue aligns the core/stratification with the first (or only) interface and the red the last interface.

We are beginning to see that the size of the convective envelope is key to the behaviour of the inertial waves and the corresponding dissipation, which is consistent with the expectation from studies of the unstratified case (e.g. Ogilvie, 2009; Goodman & Lackner, 2009; Rieutord & Valdettaro, 2010; Ogilvie, 2013). Therefore, we compare cases with a solid or stratified core that extends to the same radii as the staircase interfaces. The solid black lines on Figures 6.16a and 6.16b are the total dissipation for a single step and five steps, respectively. In Figure 6.16a, we have compared this case to both a solid core, and a stratified layer extending to that radius, $\alpha = 0.55$ and $\bar{N} = 0$ and $\alpha = 0.1$, $\beta = 0.55$ and $\bar{N} = 1$. We can see that at low frequencies there is very good agreement between these three profiles, suggesting that the forced wave response in the outer envelope only weakly depends on what is below the envelope, provided the buoyancy frequency is sufficiently strong. In Figure 6.16b we have similarly shown a solid core and a stably stratified layer, this time extending to the first interface (blue, $\alpha/\beta = 0.25$) and last interface (red, $\alpha/\beta = 0.85$). We notice although the agreement is not as good as in the single step case, there is still closer agreement between the cases where the core corresponds to the last interface of the staircase. This suggests that this is the key interface in dictating the dissipation due to inertial waves. We note that the dissipation is larger in the staircase model due to the additional layers where inertial waves are excited. In both figures there is significantly different behaviour in the mid to high frequencies where it is expected that the buoyancy effects dominate. This suggests that the importance of buoyancy forces compared with Coriolis forces will strongly depend on the forcing frequency.

In Figure 6.13b we take a preliminary check on the effect of varying viscosity and thermal diffusivity, showing total dissipation for $\nu = \kappa = 10^{-6}$ compared with $\nu = \kappa = 10^{-4}$. Although it is hard to draw robust conclusions from two data points, these initial results suggest that varying viscosity does not significantly alter the overall conclusions drawn here, and suggests that the findings in this section may be robust to varying viscosity and thermal diffusivity. We also expect that varying the Prandtl number to not be important and, as in Chapter 5, it will primarily alter the balance between viscous and thermal dissipation rates.

6.3 Comparison of dilute core models

As it is likely that the interiors of giant planets consist of an extended core, but that there is uncertainty in the exact properties of such a layer, in this section we explore further the consequences of different buoyancy frequency profiles describing stable stratification. We consider four cases that have different buoyancy profiles but all represent a stratified outer core extending to half of the planetary radius surrounded by a convective envelope. We compare,

- **Case 1** - a large solid core with a convective envelope, $\alpha = 0.5$, $\bar{N} = 0$,
- **Case 2** - a uniformly stably stratified layer extending from an inner core boundary to an outer core boundary, $\alpha = 0.1$, $\beta = 0.5$, $\bar{N} = 1$,
- **Case 3** - a single stable interface at the outer core boundary βr_0, $\alpha = 0.1$, $\beta = 0.5$, $\bar{N} = 1$,
- **Case 4** - a staircase extending from an inner core boundary to an outer core boundary, $\alpha = 0.1$, $\beta = 0.5$, $\bar{N} = 1$, steps$= 3$.

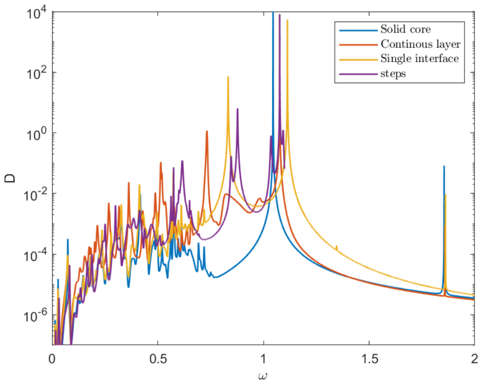

Figure 6.17: Total dissipation for different dilute core modes, where in all case $\Omega = 0.4$, $\nu = \kappa = 10^{-6}$.

All other parameters are kept constant with $\Omega = 0.4$, $\nu = \kappa = 10^{-6}$. We plot the total dissipation in each case in Figure 6.17.

We find that when considering the low frequency inertial range, the frequency-dependent dissipation is very similar in all four cases. The inertial wave behaviour in the convective envelope appears to dominate the behaviour and is little affected by the form of the stratification beneath it. We see that the stable layer and staircases act like a solid boundary for the propagation of inertial waves in the convective envelope and enhance the dissipation similarly. The cases with a stratified layer and staircase structure have higher dissipation rates due to the contribution of gravito-inertial waves in the stratified region.

Within the mid-frequency range between $0.8 \lessapprox \omega \lessapprox 1$, the behaviour varies significantly, as it is in this frequency range that the gravito-inertial modes within the stratified region are dominant. These modes are sensitive to the form of the stratification, and we observe peaks corresponding to g-modes in the case of a uniformly stratified layer, as well as the interfacial modes that are characteristic of a staircase structure.

In Figure 6.18, we compare the spatial structure in all four cases at three different forcing frequencies. Considering the first column for which the forcing frequency is low, $\omega = 0.21$, within the inertial wave range, we observe that the solution in the convective envelope is very similar in each case. In all examples

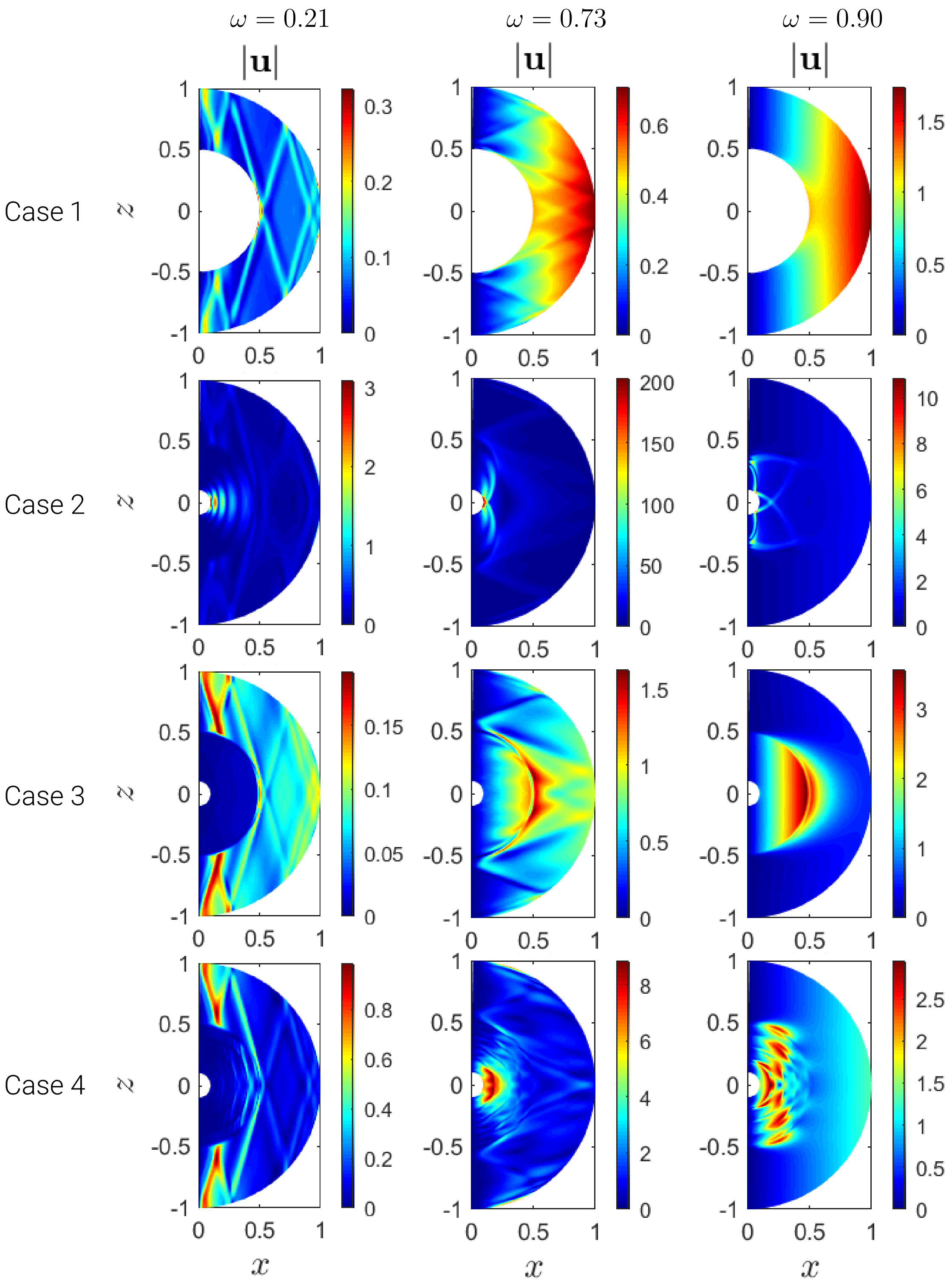

Figure 6.18: Examples of the spatial structure for different dilute cores and forcing frequencies, in all cases $\nu = \kappa = 10^{-6}$ and $\Omega = 0.4$.

the stable stratification is acting effectively as a solid boundary for the propagation of inertial waves, showing that an extended stratified core acts like a large solid core, enhancing the dissipation over cases with a small core.

In the second column, at a higher forcing frequency of $\omega = 0.73$, the spatial structure observed in the convective region again remains consistent. However, we now see the different modes that form within the stratified region, which vary significantly, contributing to the differences between the resultant dissipation. At both forcing frequencies, for the staircase and interface cases we faintly observe additional inertial modes in the deep convective layers, as well as internal gravity modes in the uniformly stratified layer. This can explain the slight increase in dissipation observed in the other cases over the case of a solid core (Case 1).

Finally, in the last column we consider the highest forcing frequency, at which we are outside of the inertial wave range but within the gravito-inertial wave ranges. We clearly observe different responses in each case that depend on the stratified region with wavelike behaviour only observable in the case with a stratified layer and a staircase structure.

6.4 Example with Saturn-like parameter values

Finally, we consider a case with parameter values similar to those consistent with the latest models for Saturn. For this we consider the values similar to those used in Mankovich & Fuller (2021), and therefore consider an example where $\alpha = 0.1$, $\beta = 0.6$, $\bar{N} = 2$, $\Omega = 0.4$. We consider both a uniformly stratified case as well as a staircase structure with one, five and nine steps. Figure 6.19a shows the dissipation rate using these four profiles and Figure 6.19b shows the tidal quality factor calculated using equation 5.12 for the case of a uniformly stratified layer. The black vertical lines show the tidal frequency of six of Saturn's major moons: Mimas, Enceladus, Tethys, Dione, Rhea and Titan, as a point of reference for the relevant frequency regimes. The tidal forcing frequencies are also shown in Table 6.1.

Satellite	Period	Ω_o	Tidal frequency	Tidal frequency
Units	(days)	(ω_d)	(ω_d)	$(\omega_d/\bar{N})$
Mimas	0.942	0.176	-0.395	-0.198
Enceladus	1.37	0.121	-0.505	-0.253
Tethys	1.89	0.0879	-0.572	-0.286
Dione	2.74	0.0606	-0.626	-0.313
Rhea	4.52	0.0367	-0.674	-0.337
Titan	15.9	0.0104	-0.727	-0.363

Table 6.1: Tidal forcing frequency $\omega = 2(\Omega_o - \Omega_s)$, for six of Saturn's major moons, data taken from Jet Propulsion Laboratory (2022). In this case $\bar{N} = 2\omega_d$.

We can see that all four cases show qualitatively and quantitatively similar dissipation profiles, and the frequency-averaged dissipation is almost unchanged as the step number is varied. In these examples all three wave frequency ranges overlap, gravito-inertial, inertial, and surface gravity modes, making it difficult to separate the behaviour of each. However, given the sensitivity to the frequency of the tidal forcing due to the moons shown, the stably stratified layer could have important implications for the tidal dissipation rates.

The tidal quality factor found, in Figure 6.19b, is evaluated to be around 10^2 to 10^4 at the frequencies relevant for Saturn's moons. This is comparable to the observational constraints from the migration rates of Saturn's moons (e.g. Lainey et al., 2017). This idealised calculation therefore highlights the importance of considering stably-stratified layers on the excitation and dissipation of inertial and internal waves in planets. This may be a key mechanism of tidal dissipation that could help to explain observations.

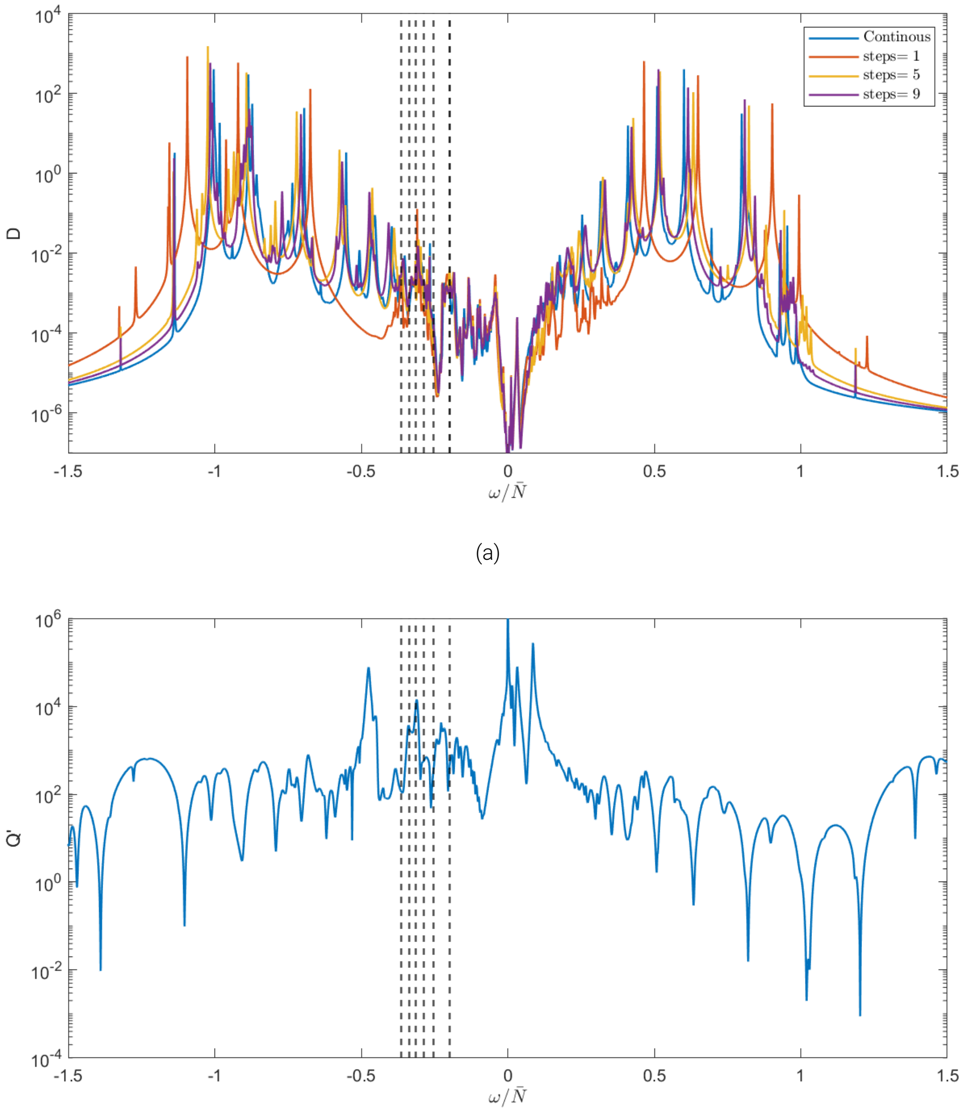

(a)

(b)

Figure 6.19: Example of total dissipation and tidal quality factor for Saturn-like parameters, with the tidal forcing of six of Saturn's moons over-plotted, Mimas, Enceladus, Tethys, Dione, Rhea and Titan.

6.5 Conclusion

In this chapter we built on the results obtained in Chapter 5 by including rotation into our system. The primary difference between the results in this chapter is that as well as the internal gravity and surface gravity modes we have observed in the purely stratified cases, we additionally observe inertial waves and gravito-inertial waves, and these can exhibit different dependencies on the parameters of our model. These additional resonances occur in similar frequency ranges to the internal gravity waves considered previously, and are likely to be significant at the relevant frequencies of tidal forcing. These additional resonances can contribute to large rates of dissipation which enhance the overall rate of dissipation.

As in the non-rotating analysis, we used a frequency-averaged quantity to establish some overarching trends in the system. We established that increasing the rate of the rotation enhances the inertial wave response, in turn increasing the total dissipation rate. In general we found that the results found in the non-rotating study were consistent with those found in this chapter. Increasing the size of the core, whether it is a solid core or a stably stratified layer, significantly increases the dissipation rate, and we found that the gravito-inertial waves excited in a stably stratified layer can enhance the dissipation compared to that of a solid core with the same radius. As in the non-rotating case, we established that provided a sufficient number of steps in a staircase-like density structure, the layer will behave as a uniformly stably stratified layer, when considering any frequency integrated quantities with differences occurring the frequency dependent dissipation.

We found that a key parameter in the excitation of inertial waves was the size of the outer convective envelope (i.e. the radius to which the dilute core extends), and that the dissipative properties can be independent of the buoyancy profile beneath it, whether it is a stably stratified layer, single interface or solid core for Saturn-like parameter values. The buoyancy frequency profile beneath this layer can alter the dissipation trends but the significance of this depends on the parameters being considered.

Chapter 7

Conclusion

The inclusion of stratified layers and semi-convective regions has significant potential impact on the tidal dynamics of giant planet systems. In this thesis we have considered the implications of including regions of stable stratification within the interiors of giant planets on the tidal response, in line with recent observations that indicate the presence of such layers within these planets. It is possible that the excitation and dissipation of tidally forced waves could contribute to the efficient dissipation and consequential fast migration rates of the satellites of giant planets. We analyse how the presence of stably stratified layers impact the transmission, excitation and dissipation of internal waves in a global spherical Boussinesq system.

Free modes of a density staircase

We present results in Chapter 2 for the free modes of semi-convective layers that form a staircase-like density/entropy structure by considering the unforced inviscid system. We found the internal modes can exhibit dispersion relations of the structure of both interfacial and internal gravity waves, depending on the properties of the surrounding fluid. As the number of steps in the staircase increases, thereby decreasing the step size, the solutions found tend towards that of a uniformly stratified medium. The shift in frequency (and period) between a staircase structure and continuous medium can be shown to have an approximate scaling of $(m+1)^{-2}$ where m denotes the number of interfaces that make up the staircase. We found this to be in agreement with the results found in the Cartesian case.

Transmission through a staircase

In Chapter 3 we turned our attention to the transmission of waves through a medium containing semi-convective layers, continuing to use the unforced inviscid system, but now considering a wave like solution in the end region. We found that the transmission through the staircase depends strongly on the properties of the staircase, and is largest when the incoming wave is resonant with the modes previously found. We showed that for large wavelength waves the transmission is largely unaffected by the presence of a staircase. In these cases, the wavelengths are sufficiently large compared to the step size that the staircase acts as if it was a continuously stratified layer. However, wavelengths comparable to the step size or smaller are only transmitted when resonant with a free mode of the system.

Tidally forced problem

In Chapters 5 and 6, we considered tidal forcing and dissipative effects, as ultimately the dissipation rates are the quantities for which comparison can be made with observed tidal migration rates. We continued in a global spherical Boussinesq system with the addition of viscosity and thermal diffusivity, as well as incorporating realistic tidal forcing. We used numerical calculations to evaluate directly the dissipation of internal waves, as well as numerical eigenvalue solutions and analytical results to supplement the direct dissipation results. We explore how uniformly stratified layers as well as semi-convective staircases alter the excitation of internal and inertial modes, and the consequences of varying the parameters of our system, on both the frequency and dissipation of these modes.

By considering first a non-rotating system we were able to establish scaling relations for various parameters of the system both numerically and analytically using a low frequency approximation. In these cases, we found that the strength and size of the stratification altered the resulting dissipation significantly. The dissipation is found to be directly proportional to the mean stratification $\bar{N}$, and scale as $(\beta r_0)^5$ where βr_0 is the size of the stratified layer. We find very little dependence on viscosity and Prandtl number in the integrated rate of dissipation, suggesting that our results could be robust to the more realistic viscosities and Prandtl numbers expected for giant planet interiors.

As we found in Chapters 2 and 3, when comparing a staircase-like density structure with a stably stratified layer, the results converged very quickly with step number, and therefore it is likely to have similar implications for the tidal problem. We considered the effect of having an isolated stable layer in the Helium metallic/molecular transition region; this allows for both a large interfacial mode resonance, and internal gravity modes to form within the layer, both of which could contribute to dissipation rates aligned with the forcing frequency.

Finally, we considered the consequences of the inertial effects by introducing rotation to the system. We found that an extended core can enhance the inertial wave response in a surrounding convective layer, thereby significantly contributing to the overall dissipation. When comparing different structures for the internal core we found that for the Ω and N values considered, the inertial wave response is largely unaffected by the properties of the stable layer, with stable stratification and a staircase structure both acting as a solid core. The stable stratification does lead to additional gravito-inertial and interfacial wave resonances, however, these do not have as significant a contribution to the overall dissipation as the inertial waves and therefore the overall dissipation is little affected. This is likely to change for lower Ω or higher N as these gravito-inertial and interfacial waves do still contribute and would have a more significant contribution when considering these different parameters regimes.

Consequence for planetary applications

We have found that regions of stable stratification can have implications for the tidal dissipation in planetary systems. They can introduce new modes, which although the contribution to the frequency-averaged dissipation may not be as significant, due to the strong frequency dependence of dissipation, if additional modes are excited they could have a significant contribution to tidal dissipation. These modes also have implications for resonance locking and mode-mixing due to the sensitivity to mode frequencies of this process. We found that a stably stratified layer can act as a large core in enhancing the inertial wave response, hence a dilute core can potentially have a significant contribution to the inertial wave response.

Future work

We have carried out an initial study on the effects of stable stratification and established that such layers can have important consequences on dissipation, but there are undoubtedly implications beyond this work.

Within the bounds of the model constructed in Chapter 4, it would be possible to consider many more permutations of the parameters than we have done in Chapters 5 and 6. Most significantly, for rotating systems the dependence on stratification strength $\bar{N}$, viscosity ν, and Prandtl number Pr, could be more rigorously considered. It is likely that at higher stratification values than considered in this thesis, the contribution of gravito-inertial and interfacial modes relative to inertial modes increases, and therefore the parallels between a stably stratified layer, solid core and staircase structure become weaker as the importance of internal gravity waves and gravito-inertial waves become more important. It is possible that some of the analytical calculations carried out to complement the non-rotating results could be extended to the rotating case, allowing for analytical dependencies to be established, such as the travelling wave limit.

It would be simple to modify the form of the buoyancy frequency used in this model to consider different stratification profiles that more closely align with the shape and values of observations. Although we expect overarching trends to be insensitive to the exact shape of the buoyancy profile, it would allow for more direct comparison with recent data.

It is also true that the Boussineq approximation is not strictly valid in the case of giant planets, some of the implications of which have already been discussed. Extending the model to incorporate the anelastic (or fully compressible) approximation would be more accurate for giant planets (Jones et al., 2011). This would allow for the study of realistic large-scale density variations. Finally, throughout this thesis we have neglecting the effects of magnetic fields and the additional physics that their inclusion would introduce. Giant planets have significant magnetic fields (e.g. Moore et al., 2018) with consequences on the physics governing their interiors (e.g. Jones, 2011) and it would likely be an interesting (albeit complex) addition to this study.

Appendices

A Viscous dissipation

It can be informative to separate the viscous dissipation into two components: the viscous dissipation occurring in the bulk of the fluid and the normal viscous flux through the boundary. Considering the momentum equation 4.3 (without rotation for simplicity, and as Coriolis forces do no work), and using index notation, we write,

$$\partial_t u_i = b g_i + \partial_j \sigma_{ij}, \tag{A.1}$$

where $\sigma_{ij} = -(p+\psi)\delta_{ij} + 2\nu e_{ij}$, is the total stress tensor for an incompressible Newtonian fluid and e_{ij} strain-rate tensor defined later. When taking the scalar product with u_i and making use of the product rule, we find,

$$\frac{1}{2}\partial_t u_i u_i = b u_i g_i + \partial_j(\sigma_{ij} u_i) - \sigma_{ij}\partial_j u_i. \tag{A.2}$$

The strain-rate tensor for an incompressible Newtonian fluid is (Acheson, 1991),

$$e_{ij} = \frac{1}{2}(\partial_i u_j + \partial_j u_i), \tag{A.3}$$

therefore by noting that by definition $e_{ij} = e_{ji}$, and by extension $\sigma_{ij} = \sigma_{ji}$, using equation A.3 we find,

$$\sigma_{ij} e_{ij} = \sigma_{ij}\partial_i u_j. \tag{A.4}$$

Using this result in equation A.2 gives,

$$\frac{1}{2}\partial_t u_i u_i = b u_i g_i + \partial_j(\sigma_{ij} u_i) - \sigma_{ij} e_{ij}. \tag{A.5}$$

Therefore, by expanding using the definition of σ_{ij} in the last term,

$$\frac{1}{2}\partial_t u_i u_i = b u_i g_i + \partial_j(\sigma_{ij} u_i) + (p+\psi) e_{ii} - 2\nu e_{ij} e_{ij}. \tag{A.6}$$

By noting that $e_{ii} = 0$ as we are considering an incompressible system where $\boldsymbol{\nabla} \cdot u = 0$, and by expanding all terms we find,

$$\frac{1}{2}\partial_t u_i u_i = b u_i g_i - \partial_j(p+\psi)\delta_{ij} u_i - 2\nu \partial_j e_{ij} u_i - 2\nu e_{ij} e_{ij}, \tag{A.7}$$

and taking the volume integral (as in Section 4.3), the following energy balance can be found,

$$\frac{\mathrm{d}KE}{\mathrm{d}t} = -\frac{\mathrm{d}PE}{\mathrm{d}t} - D_{therm} - \oint_S (p+\psi)(\delta_{ij} u_i)\hat{n}_j \,\mathrm{dS} + 2\nu\left(\oint_S e_{ij} u_i \cdot \hat{n}_j \,\mathrm{dS} - \int_V e_{ij} e_{ij} \,\mathrm{dV}\right). \tag{A.8}$$

The viscous dissipation term is separated into two components, one corresponds to the dissipation within the fluid (the volume integrated component) and is as calculated in equation 31 of Ogilvie (2009). The other is the normal viscous flux through the surface (the surface integral term). We can now establish an additional balance in the system as it can be shown numerically that the normal viscous fluxes balance the pressure integral, and the bulk viscosity component balances the injection term (involving ψ) in the absence of buoyancy forces.

B Analytical calculation of g-modes

The frequencies of the internal gravity (g-mode) resonances in a uniformly stratified medium with constant N^2 and $g \propto r$, can be analytically calculated given suitable approximations. To allow for analytical calculations we neglect viscosity and thermal diffusivity and consider alternative solid wall boundary conditions. Neglecting viscosity and thermal diffusivity is valid here as the group travel time of the modes is significantly larger than the viscous (damping) time scale.

We may reduce our system to that used in Pontin et al. (2020) and Chapter 3, where the governing equations become

$$\frac{\mathrm{d}^2\xi_r}{\mathrm{d}r^2} + \frac{4}{r}\frac{\mathrm{d}\xi_r}{\mathrm{d}r} - \left[\left(1 - \frac{\bar{N}^2}{\omega^2}\right)\frac{l(l+1)}{r^2} - 2\right]\xi_r = 0, \tag{B.9}$$

which can be solved to give

$$\xi_r = Ar^{\lambda_+} + Br^{\lambda_-}, \tag{B.10}$$

where

$$\lambda_\pm = -\frac{3}{2} \pm \frac{1}{2}\sqrt{1 + 4\left(1 - \frac{\bar{N}^2}{\omega^2}\right)l(l+1)}. \tag{B.11}$$

Here we are using displacement, $\boldsymbol{\xi} = \frac{\partial \boldsymbol{u}}{\partial t}$, where ξ_r denotes the radial component.

We are considering $\bar{N}^2 > 0$ and therefore consider oscillatory solutions with complex $\lambda_\pm$. The critical value for ω that bounds the internal gravity wave regime is found to be,

$$\omega^2 < \frac{4\bar{N}^2 l(l+1)}{4l(l+1)+1}. \tag{B.12}$$

Defining $\lambda_i = \mathrm{Im}[\lambda]$ and $\lambda_r = \mathrm{Re}[\lambda]$, the solution for displacement ξ_r can instead be written in the form,

$$\xi_r = Ar^{\lambda_r}e^{i\lambda_i \ln(r)} + Br^{\lambda_r}e^{-i\lambda_i \ln(r)}. \tag{B.13}$$

We then apply solid wall boundary conditions at either end of the domain,

$$\xi_r = 0 \quad r = \alpha r_0 \text{ and } r = \beta r_0. \tag{B.14}$$

This departs from the boundary conditions used in the numerical calculations but maintains simplicity in the analytical calculations with little effect on the final result when $\omega^2 \ll \omega_d^2$. These combine to give

$$-e^{i\lambda_i(\ln(\beta r_0)-2\ln(\alpha r_0))} + e^{-i\lambda_i \ln(\beta r_0)} = 0, \tag{B.15}$$

from which follows

$$2\lambda_i(\ln(\beta r_0) - \ln(\alpha r_0)) = 2\pi n, \tag{B.16}$$

where n is an integer, from 1 to ∞. The final dispersion relation for the frequencies given is therefore

$$\omega^2 = \frac{4l(l+1)\bar{N}^2(\ln(\beta r_0) - \ln(\alpha r_0))^2}{(2l+1)^2(\ln(\beta r_0) - \ln(\alpha r_0))^2 + 4\pi^2 n^2}. \tag{B.17}$$

C Analytical calculation of f-modes

To quantify the variation in frequency of the surface gravity (f-mode) resonance on the parameters of the system, it is helpful to analytically compute these mode frequencies. As in Appendix B we neglect the viscosity and thermal diffusivity to recover the system used in Pontin et al. (2020). However in this case instead we consider the equation for the pressure perturbation,

$$\frac{\mathrm{d}^2 p}{\mathrm{d}r^2} + \frac{2}{r}\frac{\mathrm{d}p}{\mathrm{d}r} - \left(1 - \frac{N^2}{\omega^2}\right)\frac{l(l+1)}{r^2}p = 0, \tag{C.18}$$

and include the free surface boundary condition. This can then easily be solved to find

$$p = Ar^{\mu_+} + Br^{\mu_-}, \tag{C.19}$$

where

$$\mu_\pm = \lambda_\pm + 1 = -\frac{1}{2} \pm \frac{1}{2}\sqrt{1 + 4\left(1 - \frac{\bar{N}^2}{\omega^2}\right)l(l+1)}. \tag{C.20}$$

Using the relation, $\frac{\mathrm{d}p}{\mathrm{d}r} = \omega^2\left(1 - \frac{N^2}{\omega^2}\right)\xi_r$, we can find the radial displacement to be

$$\xi_r = \frac{1}{\omega^2(1 - \frac{N^2}{\omega^2})}\left(\mu_+ A r^{\mu_+ - 1} + \mu_- B r^{\mu_- - 1}\right). \tag{C.21}$$

We use the same boundary conditions as in the Section 4.2, no radial displacement at the core, and a free surface at the planetary radius. Therefore with $r_0 = 1$ these two conditions can be combined to give,

$$1 - \frac{\mu_+}{\mu_-}\alpha^{\mu_+ - \mu_1} = \frac{\omega_d^2}{\omega^2 - N^2}\left(\mu_+ - \mu_+\alpha^{\mu_+ - \mu_-}\right), \tag{C.22}$$

where $\omega_d = \sqrt{\frac{GM}{r_0^3}}$. We consider this in different cases to predict the location in frequency of the f-mode peak, in each case taking the positive complex solution.

First we consider the case with no core and no stratification, $N = 0$ and $\alpha = 0$, and recover the expected limit (Barker et al., 2016)

$$\omega^2 = \omega_d^2 l. \tag{C.23}$$

If we consider the case in which there is a stratified layer and no inner core, $N \neq 0$ and $\alpha = 0$, we obtain

$$\omega^2 = \frac{1}{2}\left(N^2 - \omega_d^2 + \sqrt{N^4 - 2N^2\omega_d^2 + (1+2l)^2\omega_d^4}\right). \tag{C.24}$$

Taking the limit in which there is a fully convective layer with a finite core size, $N = 0$ and $\alpha \neq 0$, we find

$$\omega^2 = \omega_d^2 (l+1)\frac{\alpha^{-2(l+1)} - 1}{\frac{l+1}{l}\alpha^{-2(l+1)} + 1}. \tag{C.25}$$

The final case in which $N \neq 0$ and $\alpha \neq 0$ can be calculated using symbolic algebra packages (e.g. Mathematica). The frequency predictions in this case are plotted on some figures, but we do not show the expression here because it does not reduce to a simple form.

D Analytical dissipation in the travelling wave regime

For a sufficiently low frequency tidal forcing $\omega^2 \ll \omega_d^2$, such as those that would be expected in some tidal applications, the forced waves will be damped before they reach the inner core and form a standing mode. In these cases therefore the energy of the waves is fully dissipated into the medium. Note, although in this case we are considering the wave to be damped by viscosity and thermal diffusivity, this calculation is independent of the particular damping mechanism, and would apply in any circumstance in which waves are efficiently excited and then subsequently fully damped. For example, this regime would also occur if wave breaking occurs due to nonlinear effects (e.g. Barker & Ogilvie, 2010). We again neglect viscosity and thermal diffusivity and consider the modified pressure perturbation $W = p + \psi$ and radial displacement ξ_r to obtain

$$W = Ar^{\mu_+} + Br^{\mu_-}, \tag{D.26}$$

$$\xi_r = \frac{1}{\rho_0\omega^2(1 - \frac{N^2}{\omega^2})}\big(\mu_+ Ar^{\mu_+ - 1} + \mu_- Br^{\mu_- - 1}\big), \tag{D.27}$$

where $\mu_\pm$ is as defined in equation C.20.

If we consider frequencies sufficiently low such that the wave is damped due to viscous forces before reflecting off the inner core and returning to the outer surface, then we can assume that at (or just inside) the outer surface only the ingoing component of the wave solution is non-zero. Therefore the additional constraint we include is that

$$B = 0. \tag{D.28}$$

We continue to use the free surface condition used in our numerical results,

$$\Delta p = 0 \quad r = r_0, \tag{D.29}$$

which gives us

$$A = \frac{\psi r_0^{2-\mu_+}}{1 - \frac{\omega_d^2}{\rho_0(\omega^2 - N^2)}\mu_+}. \tag{D.30}$$

The energy flux is defined using the standard definition for a linear wave,

$$F = \pi r^2 \int_0^\pi \mathrm{Re}[-i\omega\xi_r W^*] \sin\theta d\theta, \tag{D.31}$$

where ξ_r and W have r and θ dependence, which here evaluates to

$$F = \frac{r^2}{2} \mathrm{Im}[\omega\xi_r W^*]. \tag{D.32}$$

where ξ_r and W have only r dependence. Using equations D.26 and D.27, we calculate the flux close to the outer surface by continuing to assume $B = 0$. In reality the flux is radially dependent, but we are just concerned about the flux just below the outer boundary, where $B = 0$ holds if there is no reflected wave there. Therefore the flux can be written as

$$F = \frac{\omega^3}{2l(l+1)\rho_0^2} \frac{|\mu_+ A|^2}{(\omega^2 - N^2)^2} \mathrm{Im}\left[\mu_+\right] r^0. \tag{D.33}$$

By substituting in A and μ_+ and taking the limit $\omega^2 \ll \omega_d^2 \sim N^2$,

$$F = \frac{|\psi_0|^2 r_0^5 N \omega^2}{2\sqrt{l(l+1)}}. \tag{D.34}$$

As the assumption being made is such that the wave is fully damped before reaching the inner core, we can assume that the energy dissipated is equal to the total flux of the wave, i.e. the total dissipation rate in this travelling wave calculation is given by $D_{TW} = F$.

The frequency-averaged dissipation in the travelling wave dominated regime is

$$\bar{D}_{TW} = \int^{\omega_{max}} \frac{D_{TW}}{\omega}\, \mathrm{d}\omega = \frac{|\psi_0|^2 r_0^5 \bar{N}}{2\sqrt{l(l+1)}} \int^{\omega_{max}} \omega\, \mathrm{d}\omega. \tag{D.35}$$

Therefore, it is given by

$$\bar{D}_{TW} = \frac{|\psi_0|^2 r_0^5 \bar{N}}{4\sqrt{l(l+1)}} \Big[\omega^2\Big]_{\omega_{min}}^{\omega_{max}}. \tag{D.36}$$

In most instances we take $\omega_{max} = \bar{N}$, $\omega_{min} = 0$, therefore

$$\bar{D}_{TW} = \frac{|\psi_0|^2 r_0^5 \bar{N}^3}{4\sqrt{l(l+1)}}, \tag{D.37}$$

but if we take $\omega_{max} = \omega_{crit}$ where ω_{crit}, is defined below,

$$\bar{D}_{TW} = \frac{|\psi_0|^2 r_0^5 \bar{N}^{\frac{5}{2}} (\beta - \alpha)^{\frac{1}{2}} (\nu + \kappa)^{\frac{1}{2}} (l(l+1))^{\frac{1}{4}}}{4}. \tag{D.38}$$

D.1 Transition frequency

We are considering a wave for which its damping time scale is sufficiently short that the wave does not propagate back to the outer edge of the stratified layer after it has been launched. As we are considering viscous and thermal damping in our linear calculation, we can predict the frequency describing the transition point by comparing the radial group travel time for a gravity wave packet with the viscous and thermal damping timescale.

The radial group velocity is defined as,

$$c_{g,r} = \hat{\boldsymbol{r}} \cdot \boldsymbol{c_g} = \frac{\partial \omega}{\partial k_r}, \tag{D.39}$$

where for a plane internal gravity wave with a sufficiently short wavelength

$$\omega^2 = \frac{k_\perp^2 N^2}{k_r^2 + k_\perp^2}. \tag{D.40}$$

Therefore,

$$c_{g,r} = \frac{-k_\perp k_r N}{(k_r^2 + k_\perp^2)^{3/2}}, \tag{D.41}$$

with $k_\perp = \frac{\sqrt{l(l+1)}}{r_0}$. As we are considering low frequencies, we can assume that $k_\perp \ll k_r$, and

$$c_{g,r} \approx -\frac{k_\perp N}{k_r^2}. \tag{D.42}$$

Therefore, by considering the distance required to travel $2(\beta - \alpha)$, the group travel time is

$$t_g = \frac{2(\beta - \alpha) r_0}{c_{g,r}} = \frac{2(\beta - \alpha) r_0 k_r^2}{k_\perp N}. \tag{D.43}$$

The viscous/thermal damping time is defined as

$$t_d \approx \frac{2}{(\nu + \kappa) k_r^2}, \tag{D.44}$$

which means that taking $t_g \lesssim t_d$ gives

$$k_r^4 \lesssim \frac{N k_\perp}{(\beta - \alpha) r_0 (\nu + \kappa)}, \tag{D.45}$$

or equivalently in terms of our tidal forcing frequency

$$\omega \lesssim \left((\beta - \alpha) r_0 (\nu + \kappa)(N k_\perp)^3\right)^{\frac{1}{4}}. \tag{D.46}$$

Therefore we expect the tidal response for frequencies smaller than this approximate value to be in the travelling wave regime in our linear calculations. In reality other effects including wave breaking or other non-linear effects can cause efficient damping of propagating waves; this would perhaps alter the critical frequency but we would expect to obtain the same prediction for the dissipation rate also in this case.

Glossary

adiabatic A process for which internal energy is conserved and no heat is transferred to the surroundings. 2, 24

Boussinesq approximation An approximation where variations in density are assumed sufficiently small that they can be neglected except when multiplied by gravitational acceleration. 23, 24, 30

Brunt-Väisälä frequency (buoyancy frequency), the frequency at which a fluid parcel would oscillate in a stratified fluid if it is displaced vertically, consequentially a measure of stratification. 5, 8, 24, 32

buoyancy frequency See, Brunt-Väisälä frequency. 24

Cartesian geometry A system of numerical co-ordinates in which the component axes are perpendicular to each other. 26, 35, 40, 54

dispersion relation An equation that relates the frequency of a wave to its wavenumbers. 26, 41

Eulerian A frame of reference where you consider the properties of a fluid vary over time at a given location rather than considering the properties of a fluid parcel (Lagrangian). 23, 31, 76

gravito-inertial wave a classification of internal wave, where both buoyancy and Coriolis force acts as a restoring force causing oscillations within a rotating stably stratified medium. 22, 25, 125

group velocity The speed and direction the energy of the wave is transported. 26, 60

inertial wave a classification of wave, where the Coriolis acceleration acts as a restoring force causing oscillations within a rotating medium. 22, 25, 125

interfacial gravity wave classification of gravity wave, where gravity acts as a restoring force, causing oscillations in the boundary between two fluids of different densities.. 42, 99

internal gravity wave (g-mode) a classification of internal wave, where gravity acts as a restoring force causing oscillations within a stably stratified medium. 8, 22, 25, 42, 59, 96, 125

Kronoseismology the observations and studies of waves in Saturn. 4

Love number dimensionless complex number that can quantify the tidal response, defined to be the ratio between the perturbed gravitational potential response in a body to the applied tidal potential. 16, 17, 120

phase velocity The speed and direction the wave crests are moving. 26

spherical geometry A system of numerical co-ordinates in which the position is defined by distance from the origin r, polar angle from the vertical axis θ and azimuthal angle in the horizontal plane, ϕ. 26, 29, 57, 76

tidal quality factor dimensionless quantity used to quantify the tidal response. 16, 120

transmission coefficient ratio of the radial energy flux of the incident wave with that of the outgoing wave. 59, 62

Bibliography

Acheson D. J., 1991, *"Elementary fluid dynamics"*. Clarendon Press

André Q., Barker A., Mathis S., 2017, *"Layered semi-convection and tides in giant planet interiors - I. Propagation of internal waves"*, A&A, 605, A117

André Q., Mathis S., Barker A. J., 2019, *"Layered semi-convection and tides in giant planet interiors - II. Tidal dissipation"*, A&A, 626, A82

Bailey E., Stevenson D. J., 2021, *"Thermodynamically governed interior models of Uranus and Neptune"*, The Planetary Science Journal, 2, 64

Baines P. G., Gill A. E., 1969, *"On thermohaline convection with linear gradients"*, Journal of Fluid Mechanics, 37, 289–306

Barker A. J., 2020, *"Tidal dissipation in evolving low-mass and solar-type stars with predictions for planetary orbital decay"*, Monthly Notices of the Royal Astronomical Society, 498, 2270

Barker A. J., Ogilvie G. I., 2010, *"On internal wave breaking and tidal dissipation near the centre of a solar-type star"*, Monthly Notices of the Royal Astronomical Society, 404, 1849

Barker A. J., Braviner H. J., Ogilvie G. I., 2016, *"Non-linear tides in a homogeneous rotating planet or star: Global modes and elliptical instability"*, Monthly Notices of the Royal Astronomical Society, 459, 924

Belyaev M. A., Quataert E., Fuller J., 2015, *"The properties of g-modes in layered semiconvection"*, Monthly Notices of the Royal Astronomical Society, 452, 2700

Berardo D., Cumming A., 2017, *“Hot-start giant planets form with radiative interiors”*, The Astrophysical Journal, 846, L17

Bolton S. J., et al., 2017, *“Jupiter’s interior and deep atmosphere: The initial pole-to-pole passes with the Juno spacecraft”*, Science, 356, 821

Boyd J. P., 2001, *“Chebyshev and Fourier spectral methods”*, second edn. Dover Books on Mathematics, Dover Publications, Mineola, NY

Cartwright D. E., 2000, *“Tides: a scientific history”*. Cambridge University Press

Chabrier G., Baraffe I., 2007, *“Heat transport in giant (Exo)planets: A new perspective”*, The Astrophysical Journal, 661, L81

Chernov S. V., Papaloizou J. C. B., Ivanov P. B., 2013, *“Dynamical tides excited in rotating stars of different masses and ages and the formation of close in orbits”*, Monthly Notices of the Royal Astronomical Society, 434, 1079

Christensen-Dalsgaard J., 2014, *“Lecture notes on stellar oscillations”*, `http://astro.phys.au.dk/~jcd/oscilnotes/print-chap-full.pdf`

Cowling T. G., 1941, *“The non-radial oscillations of polytropic stars”*, Monthly Notices of the Royal Astronomical Society, 101, 367

Ćuk M., Hamilton D. P., Lock S. J., Stewart S. T., 2016, *“Tidal evolution of the Moon from a high-obliquity, high-angular-momentum Earth”*, Nature, 539, 402

Ćuk M., Lock S. J., Stewart S. T., Hamilton D. P., 2021, *“Tidal evolution of the Earth–Moon system with a high initial obliquity”*, The Planetary Science Journal, 2, 147

Debras F., Chabrier G., 2019, *“New models of Jupiter in the context of Juno and Galileo”*, The Astrophysical Journal, 872, 100

Dewberry J. W., Lai D., 2022, *“Dynamical tidal Love numbers of rapidly rotating planets and stars”*, The Astrophysical Journal, 925, 124

Dewberry J. W., Mankovich C. R., Fuller J., Lai D., Xu W., 2021, *“Constraining Saturn’s interior with ring seismology: Effects of differential rotation and stable stratification”*, The Planetary Science Journal, 2, 198

Dintrans B., Rieutord M., Valdettaro L., 1999, *"Gravito-inertial waves in a rotating stratified sphere or spherical shell"*, Journal of Fluid Mechanics, 398, 271–297

Duguid C. D., Barker A. J., Jones C. A., 2019, *"Tidal flows with convection: Frequency dependence of the effective viscosity and evidence for antidissipation"*, Monthly Notices of the Royal Astronomical Society, 491, 923

Duguid C. D., Barker A. J., Jones C. A., 2020, *"Convective turbulent viscosity acting on equilibrium tidal flows: New frequency scaling of the effective viscosity"*, Monthly Notices of the Royal Astronomical Society, 497, 3400

Exoplanet.eu March 2022, *"Catalog"*, `http://exoplanet.eu/catalog/`

Favier B., Barker A. J., Baruteau C., Ogilvie G. I., 2014, *"Non-linear evolution of tidally forced inertial waves in rotating fluid bodies"*, Monthly Notices of the Royal Astronomical Society, 439, 845

Fortney J. J., Nettelmann N., 2010, *"The interior structure, composition, and evolution of giant planets"*, Space Science Reviews, 152, 423

Fuller J., 2014, *"Saturn ring seismology: Evidence for stable stratification in the deep interior of Saturn"*, Icarus, 242, 283

Fuller J., Luan J., Quataert E., 2016, *"Resonance locking as the source of rapid tidal migration in the Jupiter and Saturn moon systems"*, Monthly Notices of the Royal Astronomical Society, 458, 3867

Garaud P., 2018, *"Double-diffusive convection at low Prandtl number"*, Annual Review of Fluid Mechanics, 50, 275

Ghaemsaidi S. J., Dosser H. V., Rainville L., Peacock T., 2016, *"The impact of multiple layering on internal wave transmission"*, Journal of Fluid Mechanics, 789, 617–629

Goldreich P., 1963, *"On the eccentricity of satellite orbits in the solar system"*, Monthly Notices of the Royal Astronomical Society, 126, 257

Goldreich P., Nicholson P. D., 1977, *"Turbulent viscosity and Jupiter's tidal Q"*, Icarus, 30, 301

Goldreich P., Soter S., 1966, *“Q in the solar system”*, Icarus, 5, 375

Goodman J., Lackner C., 2009, *“Dynamical tides in rotating planets and stars”*, The Astronomical Journal, 696, 2054

Gough D. O., 1993, in Astrophysical Fluid Dynamics - Les Houches 1987. Elsevier Science Ltd, pp 399–560

Guillot T., 1999, *“Interiors of giant planets inside and outside the solar system”*, Science, 286, 72

Guillot T., 2005, *“The interiors of giant plants: Models and outstanding questions”*, Annual Review of Earth and Planetary Sciences, 33, 493

Guillot T., 2019, *“Signs that Jupiter was mixed by a giant impact”*, Nature, 572, 315

Guillot T., Stevenson D. J., Hubbard W. B., Saumon D., 2004, in Bagenal F., Dowling T. E., McKinnon W. B., eds, , Vol. 1, Jupiter. The Planet, Satellites and Magnetosphere. Cambridge Planetary Science, pp 35–57

Hedman M. M., Nicholson P. D., 2013, *“Kronoseismology: using density waves in Saturn's C ring to probe the planet's interior”*, The Astronomical Journal, 146, 12

Hedman M. M., Nicholson P. D., French R. G., 2018, *“Kronoseismology. IV. six previously unidentified waves in Saturn’s middle C ring”*, The Astronomical Journal, 157, 18

Helled R., Schubert G., 2009, *“Heavy-element enrichment of a Jupiter-mass protoplanet as a function of orbital location”*, The Astrophysical Journal, 697, 1256

Helled R., Stevenson D., 2017, *“The fuzziness of giant planets’ cores”*, The Astrophysical Journal, 840, L4

Helled R., et al., 2014, in Beuther H., Klessen R. S., Dullemond C. P., Henning T., eds, Protostars and Planets VI. p. 643, doi:10.2458/azu_uapress_9780816531240-ch028

Hubbard W. B., Smoluchowski R., 1973, *“Structure of Jupiter and Saturn”*, Space Science Reviews, 14, 599

Ioannou P. J., Lindzen R. S., 1993a, *“Gravitational tides in the outer planets. I. implications of classical tidal theory”*, The Astronomical Journal, 406, 252

Ioannou P. J., Lindzen R. S., 1993b, *“Gravitational tides in the outer planets. II. interior calculations and estimation of the tidal dissipation factor”*, The Astronomical Journal, 406, 266

Jet Propulsion Laboratory 2022, `https://ssd.jpl.nasa.gov/sats/elem/`

Jones C. A., 2011, *“Planetary magnetic fields and fluid dynamos”*, Annual Review of Fluid Mechanics, 43, 583

Jones C., Boronski P., Brun A., Glatzmaier G., Gastine T., Miesch M., Wicht J., 2011, *“Anelastic convection-driven dynamo benchmarks”*, Icarus, 216, 120

Kato S., 1966, *“Overstable convection in a medium stratified in mean molecular weight”*, Publications of the Astronomical Society of Japan, 18, 374

Kaula W. M., 1961, *“Analysis of gravitational and geometric aspects of geodetic utilization of satellites”*, Geophysical Journal International, 5, 104

Kippenhahn R., Weigert A., Weiss A., 2012, *“Stellar structure and evolution”*. Springer, doi:10.1007/978-3-642-30304-3

Lainey V., Arlot J.-E., Karatekin Ö., van Hoolst T., 2009, *“Strong tidal dissipation in Io and Jupiter from astrometric observations”*, Nature, 459, 957

Lainey V., et al., 2012, *“Strong tidal dissipation in Saturn and constraints on Enceladus’ thermal state from astrometry”*, The Astrophysical Journal, 752, 14

Lainey V., et al., 2017, *“New constraints on Saturn’s interior from Cassini astrometric data”*, Icarus, 281, 286

Lainey V., et al., 2020, *“Resonance locking in giant planets indicated by the rapid orbital expansion of Titan”*, Nature Astronomy, 4, 1053

Landau L. D., Lifshitz E. M., 1987, *“Fluid Mechanics: Landau and Lifshitz: Course of theoretical physics”*. Vol. 6, Pergamon Press

Lebovitz N. R., 1961, *"The virial tensor and its application to self-gravitating fluids"*, The Astronomical Journal, 134, 500

Leconte J., Chabrier G., 2012, *"A new vision of giant planet interiors: Impact of double diffusive convection"*, A&A, 540, A20

Leconte J., Chabrier G., 2013, *"Layered convection as the origin of Saturn's luminosity anomaly"*, Nature Geoscience, 6, 347

Liu S.-F., Hori Y., Müller S., Zheng X., Helled R., Lin D., Isella A., 2019, *"The formation of Jupiter's diluted core by a giant impact"*, Nature, 572, 355

Love A., 1892, *"A treatise on the mathematical theory of elasticity"*. Cambridge University Press

Love A. E. H., 1909, *"The yielding of the Earth to disturbing forces"*, Proceedings of the Royal Society of London, Series A, 82, 73

Lozovsky M., Helled R., Rosenberg E. D., Bodenheimer P., 2017, *"Jupiter's formation and its primordial internal structure"*, The Astrophysical Journal, 836, 227

Maeder A., 2009, *"Physics, formation and evolution of rotating stars"*. Astronomy and Astrophysics Library, doi:10.1007/978-3-540-76949-1

Mankovich C. R., Fuller J., 2021, *"A diffuse core in Saturn revealed by ring seismology"*, Nature Astronomy, 5, 1103

Marley M. S., Porco C. C., 1993, *"Planetary acoustic mode seismology: Saturn's rings"*, Icarus, 106, 508

Mathis S., Neiner C., Tran Minh N., 2014, *"Impact of rotation on stochastic excitation of gravity and gravito-inertial waves in stars"*, A&A, 565, A47

Mirouh G. M., Garaud P., Stellmach S., Traxler A. L., Wood T. S., 2012, *"A new model for mixing by double-diffusive convection (semi-convection). I. The conditions for layer formation"*, The Astrophysical Journal, 750, 61

Moll R., Garaud P., Mankovich C., Fortney J. J., 2017, *"Double-diffusive erosion of the core of Jupiter"*, The Astrophysical Journal, 849, 24

Moore K. M., et al., 2018, *"A complex dynamo inferred from the hemispheric dichotomy of Jupiter's magnetic field"*, Nature, 561, 76

Munk W. H., MacDonald G. J. F., 1960, *"The rotation of the earth; a geophysical discussion"*. American Journal of Physics, doi:10.1119/1.10629

Murray C. D., Dermott S. F., 2000, *"Solar system dynamics"*. Cambridge University Press, doi:10.1017/CBO9781139174817

NASA Exoplanet Archive 2022, *"Exoplanet plots"*, `https://exoplanetarchive.ipac.caltech.edu/exoplanetplots/`

Nettelmann N., Fortney J. J., Moore K., Mankovich C., 2015, *"An exploration of double diffusive convection in Jupiter as a result of hydrogen-helium phase separation"*, Monthly Notices of the Royal Astronomical Society, 447, 3422

Ogilvie G. I., 2009, *"Tidal dissipation in rotating fluid bodies: A simplified model"*, Monthly Notices of the Royal Astronomical Society, 396, 794

Ogilvie G. I., 2013, *"Tides in rotating barotropic fluid bodies: The contribution of inertial waves and the role of internal structure"*, Monthly Notices of the Royal Astronomical Society, 429, 613

Ogilvie G. I., 2014, *"Tidal dissipation in stars and giant planets"*, Annual Review of Astronomy and Astrophysics, 52, 171

Ogilvie G. I., 2016, *"Astrophysical fluid dynamics"*, Journal of Plasma Physics, 82, 205820301

Ogilvie G. I., Lin D. N. C., 2004, *"Tidal dissipation in rotating giant planets"*, The Astrophysical Journal, 610, 477

Papaloizou J., Pringle J. E., 1978, *"Non-radial oscillations of rotating stars and their relevance to the short-period oscillations of cataclysmic variables"*, Monthly Notices of the Royal Astronomical Society, 182, 423

Papaloizou J. C. B., Savonije G. J., 1997, *"Non-adiabatic tidal forcing of a massive, uniformly rotating star — III. Asymptotic treatment for low frequencies in the inertial regime"*, Monthly Notices of the Royal Astronomical Society, 291, 651

Polfliet R., Smeyers P., 1990, *“Dynamic tides in stars as forced isentropic oscillations and their effects on free oscillations”*, A&A, 237, 110

Pollack J. B., Hubickyj O., Bodenheimer P., Lissauer J. J., Podolak M., Greenzweig Y., 1996, *“Formation of the giant planets by concurrent accretion of solids and gas”*, Icarus, 124, 62

Pontin C. M., Barker A. J., Hollerbach R., André Q., Mathis S., 2020, *“Wave propagation in semiconvective regions of giant planets”*, Monthly Notices of the Royal Astronomical Society, 493, 5788

Remus F., Mathis S., Zahn J.-P., Lainey V., 2012, *“Anelastic tidal dissipation in multi-layer planets”*, A&A, 541, A165

Rieutord M., 2009, *“Approaching the low-frequency spectrum of rotating stars”*. Springer Berlin Heidelberg, Berlin, Heidelberg, pp 101 – 121, doi:10.1007/978-3-540-87831-5_4

Rieutord M., Valdettaro L., 1997, *“Inertial waves in a rotating spherical shell”*, Journal of Fluid Mechanics, 341, 77–99

Rieutord M., Valdettaro L., 2010, *“Viscous dissipation by tidally forced inertial modes in a rotating spherical shell”*, Journal of Fluid Mechanics, 643, 363–394

Sakashita S., Hayashi C., 1959, *“Internal structure and evolution of very massive stars”*, Progress of Theoretical Physics, 22, 830

Schwarzschild M., Härm R., 1958, *“Evolution of very massive stars.”*, The Astronomical Journal, 128, 348

Shibley N. C., Timmermans M.-L., 2019, *“The formation of double-diffusive layers in a weakly turbulent environment”*, Journal of Geophysical Research: Oceans, 124, 1445

Shibley N. C., Timmermans M.-L., Carpenter J. R., Toole J. M., 2017, *“Spatial variability of the Arctic ocean’s double-diffusive staircase”*, Journal of Geophysical Research: Oceans, 122, 980

Spiegel E. A., Veronis G., 1960, *"On the Boussinesq approximation for a compressible fluid."*, The Astronomical Journal, 131, 442

Stevenson D. J., 1982, *"Interiors of the giant planets"*, Annual Review of Earth and Planetary Sciences, 10, 257

Stevenson D. J., Salpeter E. E., 1977, *"The dynamics and helium distribution in hydrogen-helium fluid planets"*, The Astrophysical Journal Supplement Series, 35, 239

Su Y., Lecoanet D., Lai D., 2020, *"Physics of tidal dissipation in early-type stars and white dwarfs: Hydrodynamical simulations of internal gravity wave breaking in stellar envelopes"*, Monthly Notices of the Royal Astronomical Society, 495, 1239

Sutherland B. R., 2010, *"Internal gravity waves"*. Cambridge University Press, doi:10.1017/CBO9780511780318

Sutherland B. R., 2016, *"Internal wave transmission through a thermohaline staircase"*, Phys. Rev. Fluids, 1, 013701

Thompson M., 2006, *"An introduction to astrophysical fluid dynamics"*. World Scientific, doi:10.1142/P418

Trefethen L. N., 2000, *"Spectral methods in MatLab"*. Society for Industrial and Applied Mathematics, USA, doi:https://doi.org/10.1137/1.9780898719598

Tritton D. J., 2012, *"Physical fluid dynamics"*. Springer Science & Business Media, doi:10.1007/978-94-009-9992-3

Turner J. D., Ridden-Harper A., Jayawardhana R., 2021, *"Decaying orbit of the Hot Jupiter WASP-12b: Confirmation with TESS observations"*, The Astronomical Journal, 161, 72

Vallis G. K., 2017, *"Atmospheric and oceanic fluid dynamics: Fundamentals and large-scale circulation"*, 2 edn. Cambridge University Press, doi:10.1017/9781107588417

Vazan A., Helled R., Podolak M., Kovetz A., 2016, *"The evolution and internal structure of Jupiter and Saturn with compositional gradients"*, The Astrophysical Journal, 829, 118

Vazan A., Helled R., Guillot T., 2018, *“Jupiter’s evolution with primordial composition gradients”*, A&A, 610, L14

Wahl S. M., et al., 2017, *“Comparing Jupiter interior structure models to Juno gravity measurements and the role of a dilute core”*, Geophysical Research Letters, 44, 4649

Walin G., 1964, *“Note on the stability of water stratified by both salt and heat”*, Tellus, 16, 389

Wilkins A. N., Delrez L., Barker A. J., Deming D., Hamilton D., Gillon M., Jehin E., 2017, *“Searching for rapid orbital decay of WASP-18b”*, The Astrophysical Journal, 836, L24

Wilson H. F., Militzer B., 2012, *“Rocky core solubility in Jupiter and giant exoplanets”*, Physical Review Letters, 108, 111101

Wood T. S., Garaud P., Stellmach S., 2013, *“A new model for mixing by double-diffusive convection (semi-convection). II. The transport of heat and composition through layers”*, The Astronomical Journal, 768, 157

Wu Y., 2005a, *“Origin of tidal dissipation in Jupiter. I. Properties of inertial modes”*, The Astrophysical Journal, 635, 674

Wu Y., 2005b, *“Origin of tidal dissipation in Jupiter. II. The value of Q”*, The Astrophysical Journal, 635, 688

Yee S. W., et al., 2019, *“The orbit of WASP-12b is decaying”*, The Astrophysical Journal, 888, L5

Zaqarashvili T., et al., 2021, *“Rossby waves in astrophysics”*, Space Science Reviews, 217, 1